Investigation of urban networks by using Computational Fluid Dynamics Techniques and Urban Physics applications.

Tina Nepheli Vartziotis

Supervisors:

K.C. Giannakoglou, Professor at NTUA
F.J. Ulm, Professor at MIT
R. Pellenq, Senior Research Scientist MIT

Held at the Department of Concrete Sustainability Hub, Massachusetts Insitute of Technology

Submitted to the Department of Mechanical Engineering, Parallel CFD & Optimization Unit, National Technical University of Athens
Diploma Thesis

at the
NATIONAL TECHNICAL UNIVERSITY OF ATHENS
October 2018

Investigation of urban networks by using Computational Fluid Dynamics Techniques and Urban Physics applications.

by

Tina Nepheli Vartziotis

Submitted to the Department of Mechanical Engineering, Parallel CFD &
Optimization Unit, National Technical University of Athens
on October, 2018, in partial fulfillment of the
requirements for the degree of
Diploma Thesis

Abstract

To quantify geometrical characteristics of cities, we require input data of building footprints. While these can be obtained from GIS city departments, generally data sets of this kind are limited to large cities in the US and few cities in Europe. To overcome this issue, we established a method that allows us to obtain building footprints for any city in the world using open source maps (OpenStreetMap). Using buffer and clustering algorithms we were able to improve city texture calculations to account for diverse shapes of cities and their non-impervious parts. To understand the impact that city texture has on surface temperature, we utilized daytime satellite images, which only in recent years have managed to capture high resolution measurements for an entire city. Lastly, using the Monte Carlo technique we generated statistical accurate synthetic city models and used these to calculate wind loads and the drag coefficient on the buildings.

Thesis Supervisor: K.C. Giannakoglou
Title: Professor at NTUA

Thesis Supervisor: F.J. Ulm
Title: Professor at MIT

Thesis Supervisor: R. Pellenq
Title: Senior Research Scientist at MIT

Acknowledgments

I want to thank my professor Kyriakos Giannakoglou, who gave me the opportunity to work on my diploma thesis in collaboration with the Massachusetts Institute of Technology and to link the CFD code with the thesis. I also want to thank my supervisors Professor Franz Ulm and Dr Roland Pellenq for their support and guidance during the progress of this work. Especially I want to thank Jacob Sobstyl and Kostantinos Tsiakas for the support and excellent cooperation climate.

Contents

List of Figures

List of Tables

Chapter 1

Introduction

This chapter introduces the topic of urban growth and its role on environmental issues. It discusses different approaches for modeling urban networks and ways of quantifying them in order to understand their future impact on sustainability and resilience of cities. The chapter concludes with the objectives of this research, followed by an outline of this thesis.

1.1 Urban Population Growth

The rapid growth of urban population creates an intensified need for the development of urban infrastructure,[43]. Patterns of urban growth have become more complicated in the past couple of decades. Many cities have experienced fast outward expansions from the central core, such as downtown New York and Athens but there are also areas that have been expanding without any obvious pattern, for instance Los Angeles and London[37].City growth is intrinsically related to population growth,[37]. Studies conducted by the United Nations predict similar patterns of expansion in urban life in the next decades,[35]. To make cities safe, resilient and sustainable, they have to become smart, sustainable and inclusive from an economy perspective. If cities are to deliver such sustainable growth, there is a need to establish a platform that will foster cities to continue to thrive and grow, while improving resource usage and reducing pollution and poverty, thereby creating cities of opportunities with universal access for services, energy, housing and transportation,[35][34].

The mark has been surpassed where globally more people live in urban than in rural areas. Over 55% of the world's population now resides in urban areas. In 1950, 30% of the world's population was urban, and by 2050, 68% of the world's population is projected to be urban. Today, the most urbanized regions include Northern America (82% urban), Latin America and the Caribbean (81%), Europe (74%) and Oceania (68%). The level of urbanization in Asia is now approximating 50%. In contrast, Africa remains mainly rural, with only 43 % of its population living in urban areas. [35][35]

The urban population of the world has grown rapidly since 1950, having increased from 751 million to 4.2 billion in 2018. Asia, despite being less urbanized than other continents, is home to 54% of the world's urban population, followed by Europe and Africa (13% each). Growth in the urban population is driven by the overall population increase and by the socio-economic lift of people moving at a higher rate to urban areas. Combined, these two factors are projected to add 2.5 billion to the world's urban population by 2050, with almost 90% of this growth predicted to occur in Asia and Africa [35][34]depicts a dramatic increase of the proportion of total population for all major areas. None of the illustrated areas will have urban population less than 50%. Some cities have experienced population decline in recent years. Most of these are located in low-fertility countries of Asia and Europe where overall population sizes are stagnant or declining. Economic contraction and natural disasters have contributed to population losses in some cities as well,[35][34].

Urban growth is closely related to the three pillars of sustainable development: economic growth, social progress while minimizing the environmental footprint. Well-managed urbanization, informed by an understanding of population trends over the long run, can help to maximize the benefits of agglomeration while minimizing environmental degradation and other potential adverse impacts of a growing number of city dwellers, [35][34].

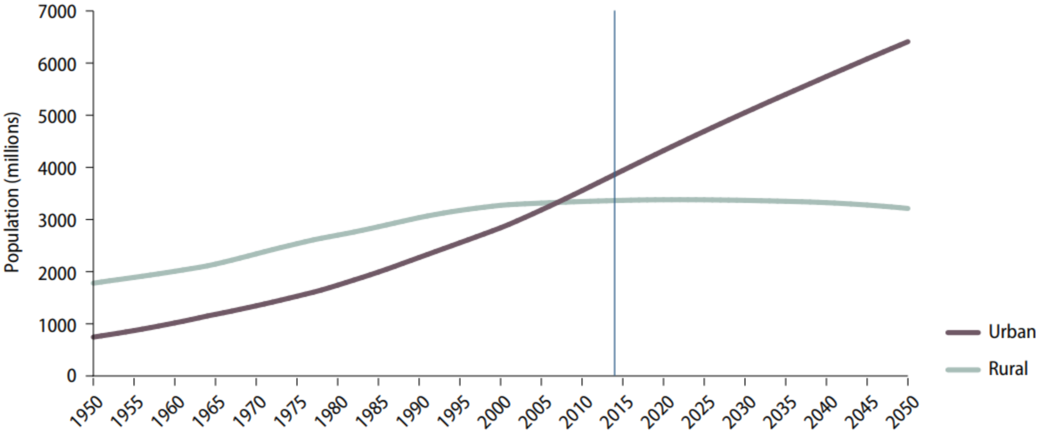

Figure 1-1: Urban and rural population of the world 1950-2050, United Nations

1.2 Environmental Issues

The microclimate in urban areas differs significantly from the climate in rural areas. Wind speeds are lower due to wind sheltering leading to less removal of heat and pollutants from urban areas and air temperatures are higher due to urban heat island effect,[11]. Natural surfaces such as vegetation have been replaced with non-vegetated surfaces like asphalt and concrete, which have the ability to store heat, which is later released back into the atmosphere. This change in land use is known to increase the land surface temperature[43]. In order to meet the need for secure and environmentally friendly cities, there is a need to focus on the response of cities to external actions during operation and in extreme situations. These include, but are not limited to Urban heat islands, hurricanes, flooding and air pollution.

1.2.1 UHI (urban heat island) -Surface UHI effect

Urban heat island (UHI) is a climate phenomenon that results in increased air temperature in cities when compared to their rural surroundings. UHI is generally considered to be an adverse effect with its externalities ranging from increased air pollution to higher energy demand, and deteriorated human health and comfort. With future urban growth patterns, the impacts of UHI will magnify, a part of urbanization natural surfaces such as vegetation are replaced with non-vegetated surfaces such as asphalt and concrete. Warmer air caused by UHI increases heat stress on urban residents, potentially raising the threat of mortality. In addition, higher temperature increases energy consumption and associated greenhouse gas emissions due to intensified use of air conditioning. Accurate quantification of UHI can help to efficiently evaluate the potential heat risks and guide city management and development for government and city planners. Traditionally, the detection of UHI has been conducted considering measurements at urban and rural regions. Similarly, the study of surface UHI (SUHI) uses remote sensing satellite images captured in urban and rural regions. The estimation of UHI relies on the definition of urban and rural stations, and for SUHI on image pixel resolution. In the last few years, global climate change already had observable effects on the environment. From the normally mild summer climates of Ireland, Scotland and Canada to the scorching Middle East to Southern California, numerous locations in the Northern Hemisphere have witnessed their hottest weather ever recorded over the first July week in 2018, as depicted by the figure below [45].

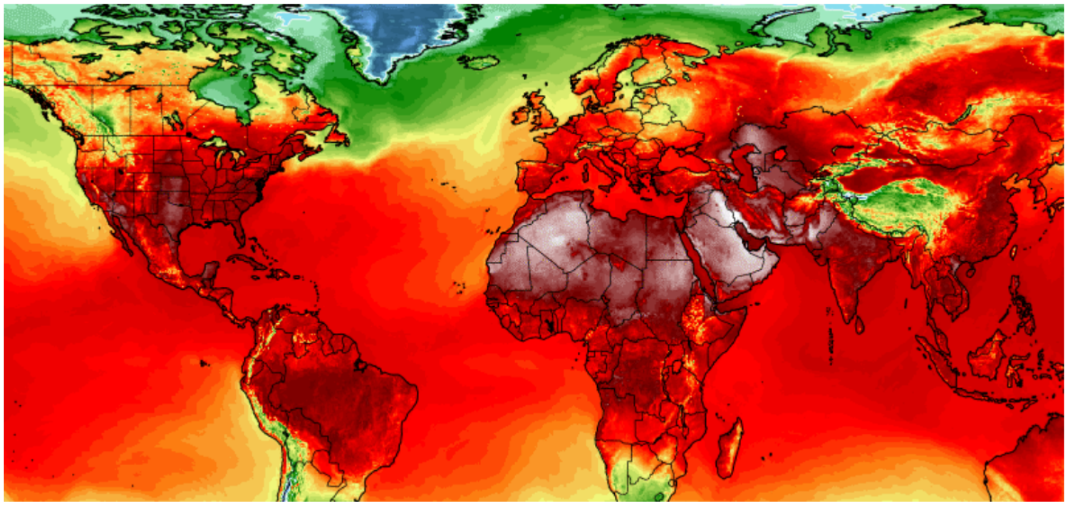

Simulation of maximum temperatures on July 3 from American (GFS) weather model at two meters above the ground. (University of Maine Climate Reanalyzer)

Figure 1-2: All-time heat records have been set all over the world during the first week of July 2018, Washington Post

1.2.2 Extreme Events-Resilience

Cities worldwide have experienced a significant increase in damages and losses due to a variety of disasters in recent years. According to a recent United Nations International Strategy for Disaster Reduction (UNISDR) report (2015), natural hazards, such as hurricanes and floods, cause economic losses of up to US$300 billion each year. There is an increasing amount of evidence that the exposure of urban assets worldwide has increased faster than the decrease in vulnerability, which has generated new risks for urban assets, and consequently a steady increase in hazard-related losses. Climate change is one of the biggest global threats to human health of the 21st century[43]. Its perils to society will increasingly be connected to weather-driven hazards [37], [16], [104], because extreme weather states are expected to disproportionately rise compared with changes in climate averages [74]. Human beings are affected by extreme weather events through a set of complex pathways, including direct effects, such as death or immediate injuries, and delayed or indirect effects, such as illness, mental health effects, and effects associated with the ecology of infectious diseases and disruption of crucial infrastructure. A survey from Lancelet Planetary health projections has shown a rapid rise in the death toll due to weather-related disasters in Europe during this century under a scenario of climate and population change. During the 30-year period of 1981-2010, around 3,000 people per year lost their lives because of weather related disasters. If no adaptation measures are implemented, this number could rise substantially in the upcoming decades. It is predicted to reach 32,500 deaths (uncertainty range 10,700-59,300) by the period 2011-40 (about a ten times increase), 103,300 (48,300-179,300) by 2041-70 (about a 30 times increase), and 152,000 (80,500-239,800) by 2071-100 (about a 50 times increase). These trends are shown in Figure i-x, inform of a plot of the number of deaths and the number of people exposed to multiple weather-related hazards [38]. For instance floods on the outskirts of Athens have killed 23 people, injured dozens, and the majority of buildings, highways, and infrastructure facilities, located below sea level were drowned by floodwaters. This highlights the need to understand and study the factors that cause these catastrophic events. To achieve this goal, efficient information for buildings in urban areas is required to model urban environments and to study urban vulnerabilities. While rebuilding infrastructure to be more resilient will reduce the risk of future damage, it is not feasible to rebuild entire cities. It is possible, however, to identify the specific buildings in cities that are most vulnerable to failure as a result of intensified wind loads and to make those buildings more resilient vis-Ãă-vis to hurricane damage through e.g. hurricane-proof retrofitting techniques. [83]

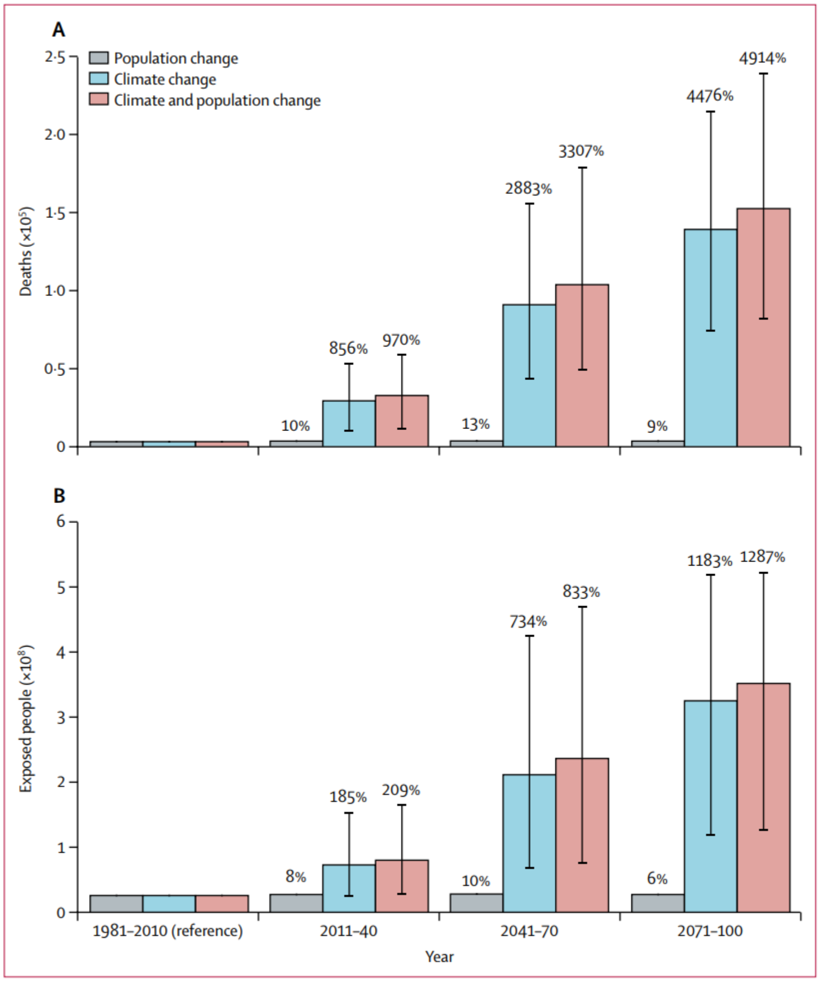

Figure 1-3: Overall risks of weather-related hazards to the European population for each time period,Lancelet Planetary health

1.3 Modeling of Cities

Models are abstractions, simplifications of the 'real thing'. According to Morrison[3] models play an autonomous role in science and design. In other words, models are not theories, nor are they equivalent to the realities they seek to represent or manipulate. Models thus act as instruments that enable scientists and engineers to explore the world, to predict it and to plan for it prior to 'acting' on the world in some irrevocable way,[3].

1.3.1 Existing City Models

There have been different ways of modeling cities, either for city planning or to conduct different static and dynamic analyses. These are:

1. **Land use transportation models** were the first mathematical models that simulated how activities such as employment, population and the trips are connected through the journey to work located at different areas or points represented as small zones within the city. However, these models are limited in their predictive capabilities. That is, such models fail to generate compact, radial, ribbon, sectorial and other morphologies that are icons of urban planning,[3].

2. **Morphological models** are cellular automata models that aim to capture urban development, by simulating urban morphologies. Land development is based on accessibility to land use types and activities at a distance from the site in question subject to various physical constraints and land suitability encoded as cellular development rules operated sequentially in time,[3].

   Jobstyl et al. [16] introduced the usage of the radial distribution function, g(r), for analyzing city texture. In the context of buildings, g(r) is the probability of finding a building at distance r from the reference building relative to the average. This method will be used to identify different city textures, as it will be explained more thoroughly in the following chapters.

3. **3-D city models**are generated using rapid-capture techniques such as airborne laser scanning, that permit the generation of 3-D representations of buildings in block form and which can be improved with land parcel and street geometry data. What makes the current generation of digital 3-D models important is the notion that such models are databases that can store any kind of spatial urban data with just their geographical reference. That is, these models do not only represent the digital geometry of traditional models, but also represent large-scale databases which can be viewed in 3-D. However, such 3-D models of cities are still very limited, with usually just small samples available to the public,[3].

1.4 CFD Analysis for Urban Design and Computational Cost

Between 1993-2012 more than 75% of catastrophic losses in the United States was caused by windstorms (1). The Congressional Budget Office estimated the average annual damage to be $28 billion dollars (0.16 % of GDP), with a potential rise of 55% to $38 billion by 2075, which is attributed to coastal development(2).[50] This economic impact of wind related events calls for reevaluation of engineering approaches. 2017 was one of the most devastating U.S. hurricane seasons ever recorded. State Departments of Public Safety across the U.S. tens of thousands of destroyed homes and hundreds of thousands more as damaged. Although, the total economic impact continues to be measured, estimates from NOAA's National Centers for Environmental Information place damage costs for weather and climate related disaster events at over $300B, with hurricane-related costs accounting for more than $200B of that total,[50]. To increase the resilience of cities, there is thus a need to identify the most vulnerable buildings in cities, and to make those buildings more resistant to hurricane damage. With this focus in mind, this research aims to examine how additional long-range city texture parameters can be used to create urban models that enhance previously established computational fluid dynamics (CFD) methods. This method solves and analyzes problems that involve flow of fluids. In the field of architecture, urban design and urban planning, CFD is useful for analysis and understanding of the loads on buildings during hurricanes and floods.

When dealing with real cities, the problem becomes more complex. First of all, a simulation domain is required that is significant larger than the one usually considered in micro-scale simulations. Moreover, the emissions, hurricanes, floods are parameters that affect a larger area, or even the whole city. Finally, there are limitations in micro-scale simulations regarding the geometry complexity and the associated mesh grid density,[18]. Thus, a CFD simulation and analysis of the whole city introduces an enormous computational cost and a highly consuming simulation time. For this reason there is a need for reduced models, in a way that maintains the required information for each approach.

Such models must be statistically representative of city textures. This requires obtaining map data, composed of buildings and their geographical location. This type of information is referred to as Geographic Information System (GIS) Data.

1.5 Research Objectives

This research extends a city texture approach of Sobstyl et.al [84] using GIS data. This extended g(r) approach is validated for UHI associated with daytime temperature using satellite data to extract the surface temperature of cities and their surroundings. The novelty of the presented approach is the use of open-source data for determination of the radial distribution function of cities. These data are then used to generate synthetic cities by applying computational fluid dynamics. Finally the synthetic cities are subject to different wind speeds.

1.6 Thesis Outline

Following this introduction presents the four chapters compose this thesis. Chapter 2 presents the Open-Source Software for data collection, and the models use, which employs to extract city data. In chapter 3 the methodology for obtaining Land surface temperature and computing the Surface Urban Heat Island (SUHI) using Satellite Data and OpenSteetMap Boundaries is explained. Chapter 4 presents the MC approach to generate synthetic cities and the correlation between city structure and urban physics phenomena are disassed. In chapter 5 the different approaches of Computational Fluid Dynamics and its application to our synthetic models is presented. The thesis finishes with conclusions and recommendations for future research.

Chapter 2

Open-Source Software for data collection

2.1 Introduction

This chapter addresses the first research objective which is obtaining building footprints from OpenStreetMap, for the purpose of quantifying city texture. The method of data acquisition and pre- and post-processing is explained. Open data are still suffering from incompleteness at a global scale of building footprints. Thus to confirm the accuracy of the methodology and quality of data, the radial distribution function is validated thus obtained with the proposed method against results from city data.

2.2 OpenStreetMap

In order to calculate Radial distribution function g(r) for city texture there is a need to obtain building data. This data specifies building footprints and geographical locations. With building footprints additional building parameters such as building areas can be obtained. After editing and converting buildings to points, radial distribution function g(r) can be derived. However, there are difficulties to obtain data for cities outside the U.S. Especially for Europe. Universities and local authorities do not provide appropriate data. For German cities, while the data sets exist, they can be very costly. For instance, Stuttgart's data would cost 30,000$, e for Athens there is no available GIS data. This motivates using open source data from online maps, like OpenStreetMap, which is an online mapping tool like Google Maps with the main difference that it doesn't require licensing for obtaining data. By using OpenStreetMaps sufficient information can be obtained for many densely populated cities across the globe.

2.2.1 OpenStreetMap Comments

The use of OpenStreetMap (OSM) is motivated by restrictions regarding the use or availability of global GIS data. OSM is a collaborative project aiming at creating a free editable map of the world,[70]. OSM provides sufficient information for many highly populated cities across the world. OSM emphasizes local knowledge based upon aerial imagery, GPS devices, and low-tech field maps to verify that OSM is accurate and up to date. OpenStreetMap's community includes enthusiast mappers, GIS professionals, engineers running the OSM servers, humanitarians mapping of disaster-affected areas, and many more,[93]. OSM data are constantly updated, with updates made as frequent as on an hourly basis. Contributors are volunteers (over 1,000,000 contributors so far, and growing every day) - who know the area well,[94]. Moreover OpenStreetMap is an open source data, which means that anybody can freely use it.

2.2.2 Downloading OSM Data

OpenstreetMap has open map data. It is possible to download map data from the OSM dataset in a number of ways. The full dataset is available from the OSM website download area.*www.openstreetmap.org* It is also possible to select smaller areas to download. Data normally come in XML format or as OSM files. Extensible Markup Language (XML) is a markup language that defines a set of rules for encoding documents in a format that is both human- and machine-readable,[102].Files can be downloaded either from the OSM website, or by using XAPI. API is the acronym for

Application Programming Interface, which is a software intermediary that allows two applications to talk to each other and XAPI is an extended version of API,[95].

2.3 Methodology

The workflow shown in Fig. 2-1 below, defines the methodology that has been developed to obtain OSM data. The approach is applied to extract 2D building footprints from an online map. It is worth mentioning that for some cities it is also possible to extract heights of buildings, but for most cities these data, as of now, are still incomplete. The workflow method is grouped in three basic steps. The flowchart shows the process of converting buildings into points by editing complex map data, which subsequently is the input file for city texture calculations. This workflow has been implemented in an automatic manner so that a user only needs to input GPS coordinates of the city to obtain building footprints in a format required for city texture calculations.

To extract and edit map data websites and GIS software packages have been utilized. In addition to the OSM website, QGIS has been used as well, which is a free and Open Source Geographic Information System. ArcGIS, which is another GIS for analyzing and editing maps [96] and Wambacher-osm, a Boundaries Map which provides a comfortable overview of the administrative boundaries in the OSM dataset, have been used also. The latter also provides downloading capabilities for city boundaries,[69]. For further processing Matlab Software and Python scripts have been taken into account.

2.3.1 OSM Data Analysis

2.3.2 City Boundaries

For downloading larger areas greater than a bounding box of about 0.5 degree by 0.5 degree, XAPI, which for large cities appears to be the most efficient way, had to be used.

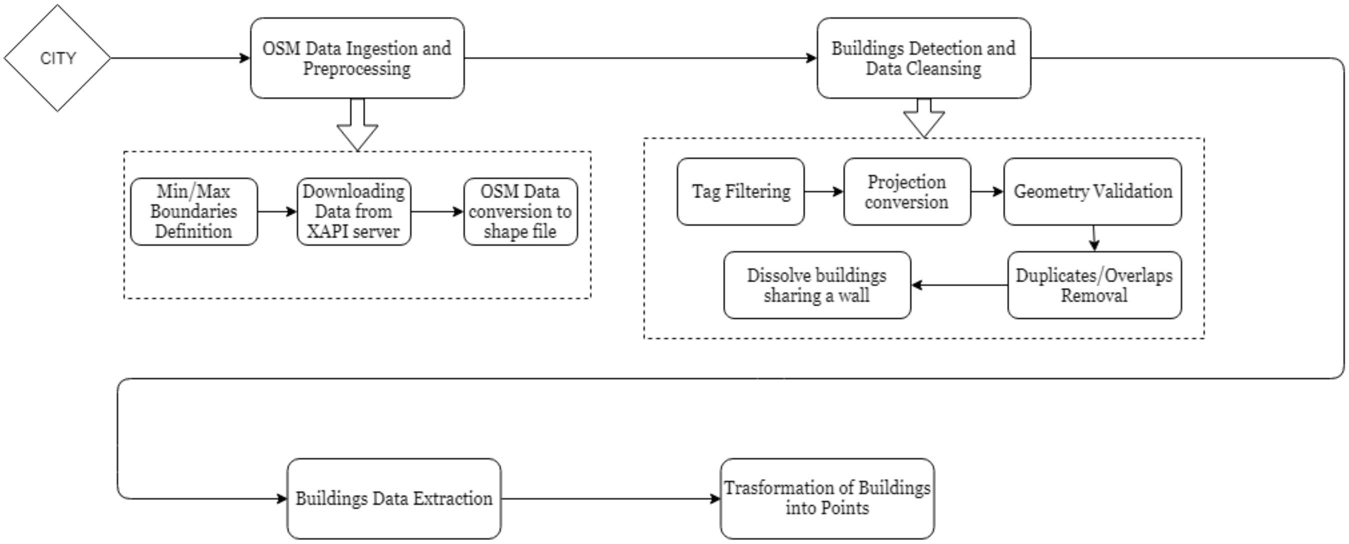

Figure 2-1: General Workflow of building download and processing

To download the data, GPS boundaries have to be defined. The boundaries are needed in order to determine which part of the map should be downloaded. The definition of boundaries of each city is also required in order to extract online data in the corresponding region. This is achieved by defining longitude and latitude boundaries for each city. In the case of larger cities, the region needs to be splitted into rectangles. This is because the online downloading platform has a limit w.r.t. the amount of data it is able to process. Once downloaded, buildings are converted into an appropriate processing form.

Step 1: Download data with XAPI

Using the Ubuntu terminal and XAPI, the OSM file of a city is downloaded.

The coordinates form a rectangle. This rectangle has the maximum and minimum coordinates of the boarder boundaries chosen before. This way of downloading data makes the procedure more efficient and quick. This is very useful since large files of a a city, cannot be downloaded from the website.

A region, with a lot of data,has to be specified. The command line used for this as follows:

```
wget -O boston.osm "http:/overpass.openstreetmap.ru/
 cgixapi_meta*[bbox=-71.19,42.22,-70.986,42.399]"
```

Step 2: Download data with XAPI in blocks

Due to limitations of online downloading platforms, in the case of very large cities (i.e. Chicago or New York), the region has to be divided into rectangles. The algorithm splits large areas into rectangles. The reconstruction of the city is achieved at the end by appending the attribute matrices by all the neighborhoods/rectangles.

2.3.3 Step 3:Data Preprocessing

Conversion from osm to shape file

The next step is to convert an osm map file to a shape file. QGIS software, converts the downloaded osm file into a shape file in which buildings are presented as polygons. This requires an appropriate shape file format, easy to operate.

Shape File Format

The shapefile format is a popular geospatial vector data format for geographic information system (GIS) software. It is developed and regulated by Esri as a (mostly) open specification for data interoperability among Esri and other GIS software products. The shapefile format can spatially describe vector features: points, lines, and polygons,[101].

2.3.4 Building Detection and Data Cleansing

First, the extraction of buildings is required, as the online data includes all the information found in a map, which in addition to buildings also includes roads, intersections, sidewalks, various building tags (such as functional building attributes, industrial or residential). This information is not required for this analysis, therefore it can be removed. The extraction is based on tags. Buildings have their own tags and can be separated.

Building Tag

The building tag is used to mark a given object as a building. The most basic tag use is building=yes, but the value may be used to classify the type of a building. Tagging is a single building outline that can be created for each building complex or block; which may relate to a single detached property, or to a row of individual terraced houses or to some more complex arrangement of properties,[94].

Buildings Within the City

The broader boundaries of a city get mapped onto the exact borders of

a city. The tool to achieve this, is provided by `https://wambachers-osm`. This tool also allows to download the shapefile, which directly provides boundaries in a single file. This procedure is also the difference from the one where the data are directly downloaded from OSM, which provides

borders in pieces. In order to get the building within a city two shapefiles are intersected/divided from OSM downloaded city together with its boundaries.

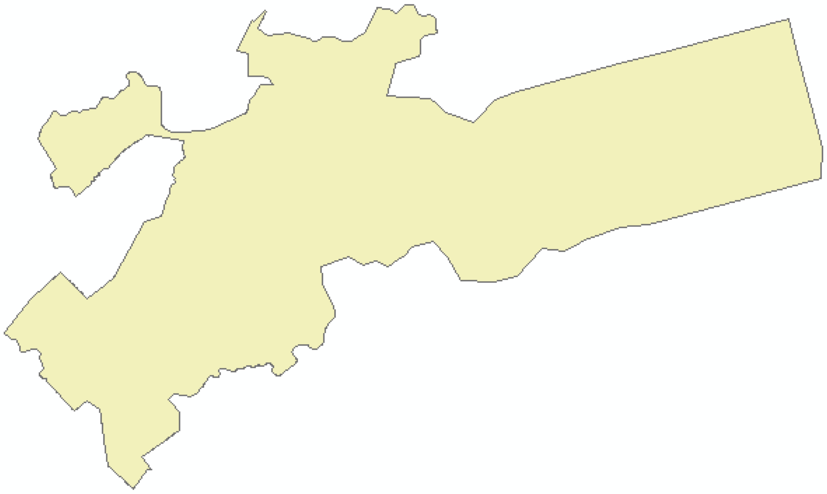

Figure 2-2: Boundaries of city of Boston obtained by OpenstreetMap.

Geometry Validation

It is not uncommon for buildings to initially be described as simple group outlines and later be improved with more detailed outlines and to be split into individual properties. This procedure leads often to imperfections, like overlapping, invalid or duplicate polygons. These are commonly found in OSM data.

Dissolve

The next step consists to dissolve buildings, or in other words merge buildings. This tool aggregates features based on specified attributes. That is, it combines buildings that share a wall. This is required because, for temperature or wind calculations, two buildings that share a wall are essentially considered a single building. This step was primarily applied based on the methodology of quantifying city texture, with the objective to focus on the energy transfer between separated buildings or blocks,[84]. However, this step had to be omitted, since after dissolving buildings the reduction of buildings in several cities was 50%-80%, which resulted in an insufficient number of buildings to calculate g(r). For example, there were 20,395 buildings for Madrid before dissolving, which turned to just 3,549 after applying the procedure. This amounts to a reduction of 82.6 % buildings for Madrid. More values are shown in the table below.

City	**from**	**to**	**Percentage%**
Paris	103366	16034	84.4
Rome	20451	10610	48.1
Milan	6375	1217	80.9
Prague	19075	6273	63.11
Rio de Janeiro	17507	2662	84.79

(a) Dissolved buildings

(b) Non-dissolved buildings

Figure 2-3: Dissolve and Non- Dissolved buildings

Eliminate Holes

This creates a new output feature class containing the features from the input polygons with holes of a specified size of the polygon deleted. Since polygon holes are considered parts of the polygon, they can be deleted or filled using this tool. If the hole area is smaller than the specified size, the hole is eliminated and the space is filled in the output. Any part that is inside the deleted hole is also eliminated in the output.

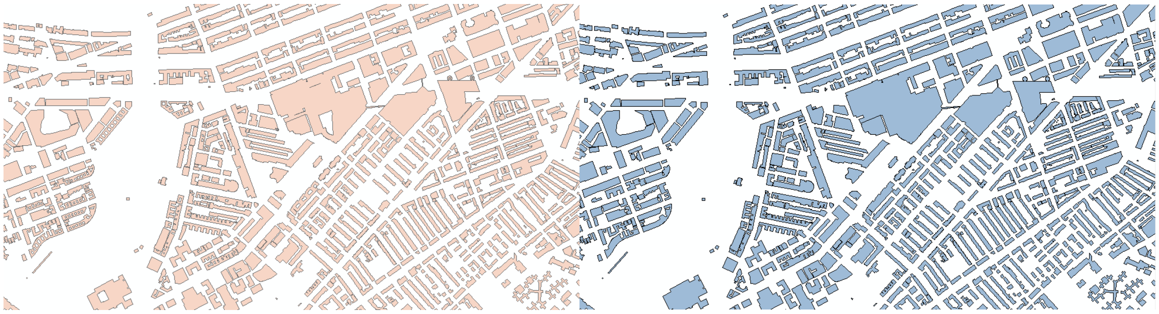

(a) Buildings with holes (b) Buildings with no holes

Figure 2-4: Before and after the Eliminate Polygon Part Procedure

Projection Conversion

GIS projection is a mathematical transformation that take spherical coordinates (latitude and longitude) and transform them to a XY (planar) coordinate system. This enables to create a map that accurately shows distances, areas, or directions. With this information, accurately work can be achieved by using the data to calculate areas and distances and measure directions. As implemented in Geographic Information Systems, projections are transformations from spherical coordinates to XY coordinates systems and transformations from one XY coordinate system to another. Projections are chosen based on the needs of the map or data analysis and on the area of the world. Projections are useful for a limited set of purposes or scales. Finally, projections are based on local needs and standards. The way to complete that, is using the coordinates of a city and a table provided of ArcMap in order to select the right projections. The name of the projection or a specific code which defines the projections of different areas of the world can be used to automize the method. An obstacle is that the projection needs to be found in order to define code or name as an input to the algorithm.

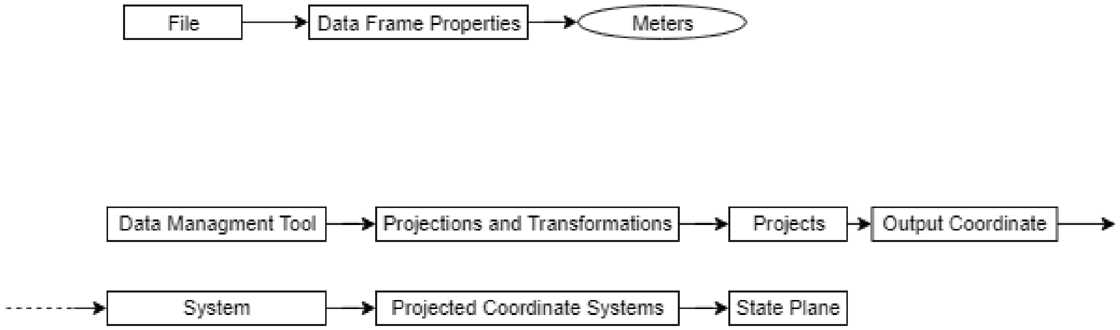

Figure 2-5: ArcMap Steps for Projection Conversion

2.3.5 Building Data Extraction

Area of Buildings

An important step of calculating building needs is to project the coordinates to meters. More specifically a field in the attribute table has to be added, which reports all the necessary information for the file. After naming the field 'Area' the type is specified to double and the precision to 15 and scale 2.

Area of Boundaries

Following the same procedure for the boundaries of the city, the total area of the city has to be calculated in order to compute the density. As explained in further steps this is a criterion to decide whether the data are sufficient.

Conversion Building to Point

The final step of this workflow and actual objective of data extraction is to convert buildings into points. This conversion requires some statistical analysis, performed by the GIS software. The goal of this step is to have a representative point lying inside the building, to represent it. First the geometric properties of buildings are aggregated into an attribute vector form for each point. That means that there is a table where each row represents the attribute of each point and its corresponding building. By these means a point representation of the buildings is achieved, without losing any information of the geometry, such as its perimeter or area. In previous work [84] buildings transformed into a set of single points using buildings' 2-D center of mass. That approach can lead to a point outside the building, when the shape is irregular.

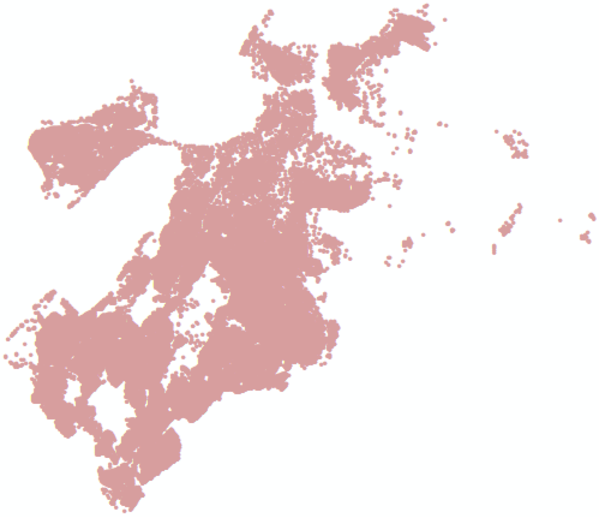

Figure 2-6: Buildings converted to points

Figure 2-7: Buildings converted to points zoomed

2.4 Selection of Cities

A first approach of city selection is exploring the availability of data in OSM. After completing this method density has to be calculated in order to verify the selection.

The accuracy offered by OSM is not always sufficient. For instance, many cities have missing building footprints,not enough building information. A density criterion for selection of GIS samples has been adopted for ensuring accurate results:

$$\rho = \frac{1}{A_{city}} \sum_{i=1}^{N} A_{b_i} > 0.1 \tag{2.1}$$

City	Density
Cape Town	0.094487
Sao Paulo	0.436305
Mexico city	0.277093
Rio de Janeiro	0.323025
Bengaluru	0.224391
Jerusalem	0.113991
Moscow	0.324770
Singapore	0.073302
St. Petersburg	0.235562
Tel Aviv	0.160751
Tokyo	0.136703
Athens	0.385946
Berlin	0.187805
Bucharest	0.121718
Dublin	0.219291
London	0.135134
Madrid	0.364349
Milan	0.422862

City	Density
Paris	0.320
Prague	0.218
Rome	0.276
Sofia	0.139
Stuttgart	0.325
New York	0.562
Naples	0.101
Boston	0.085
Jacksonville	0.0095
Kansas city	0.036
Miami	0.079
New Orleans	0.036
St. Petersburg USA	0.037
San Francisco	0.128
Vancouver	0.174
Montreal	0.128

Table 2.1: Densities of Cities

The table depicts that cities like Boston, Miami,New Orleans don't fulfill the density criterion. This occurs to cities, which include a large see area in their boundaries.

On the other hand Kansas and Jacksonville have very large boundaries. The first counts 825 km^2, where the second onesâĂŹ boundaries are 2.266 km^2. However, the building footprint data are very dense in the city center that allows their usage for further calculations.

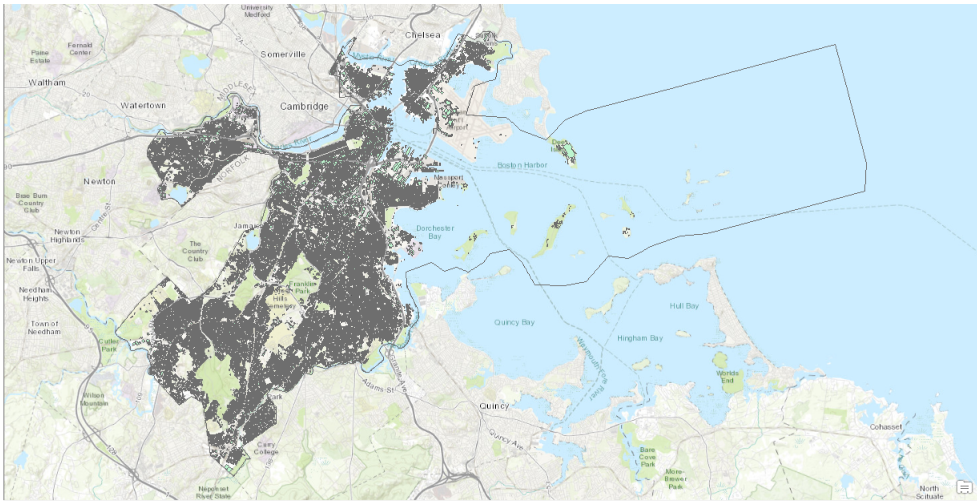

Figure 2-8: Boundaries of Boston covering an extensive area in the sea

2.5 Validation of open source data utilization

This section presents the accuracy of the usage of open source data for the employment of city texture calculations using the radial distribution function, g(r). Specifically, for this comparison the radial distribution function has been computed using data from GIS departments and from OSM. The g(r) has been calculated in the same way as in [84]. That means using a buffer around specific coordinates in the city. A different approach for the g(r), which will be explained in chapter 3, will be used later on.

2.5.1 Radial Distribution Function

The first step of validation is using the radial distribution function, a method which will be explained thoroughly in chapter 3. In brief, in the context of buildings within a city, g(r) is a 2-d spatial distribution of local density relative to the average density of buildings. More specifically, it quantifies the probability of finding a neighboring building at a given distance relative to the building of reference. For instance, for Chicago, the probability of finding a building at a distance of 30 feet is almost 6 times higher than at a distance of 300 feet. To validate open source data, g(r) analysis has been performed for 4 cities.

2.5.2 Comparison

The following validation is based on the comparison of OpenStreetMap data and GIS departments data using the methodology of the publication,[84]. Main difference of the validation and the approach presented previously is the sample of buildings. Not the whole city has been analyzed, the computation in publication and in validation is based on buildings within a 3-mile radius. The figures 2-9 - 2-12, depict radial distribution functions for validated cities.

2.5.3 Validation of OSM using g(r) graph

Mean Absolute Error (MAE) and Root mean squared error (RMSE) are two of the most common metrics used to measure accuracy for continuous variables. These two error metrics are usually used for prediction tasks,[101]. For the diagrams below four classic error metrics have been computed: the Mean Absolute Error, the Root Mean Square Error, the difference of Means and the difference of Standard Deviations.

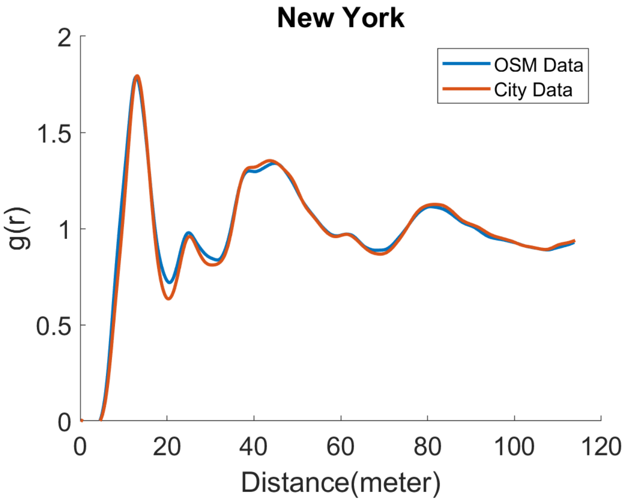

Figure 2-9: Radial distribution function for New York using OSM and Data from GIS Department

Mean Absolute Error (MAE):

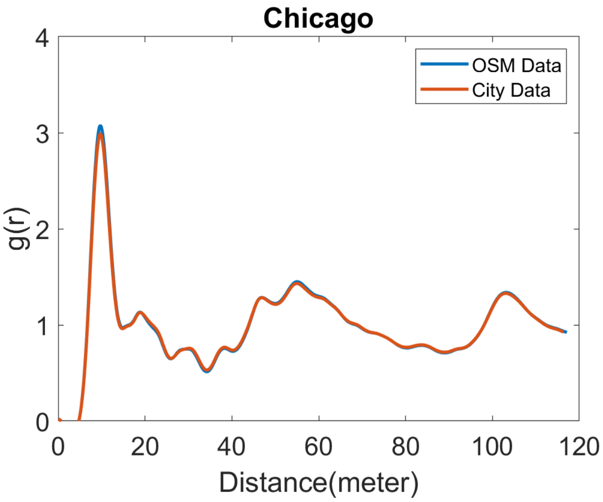

Figure 2-10: Radial distribution function for Chicago using OSM and Data from GIS Department

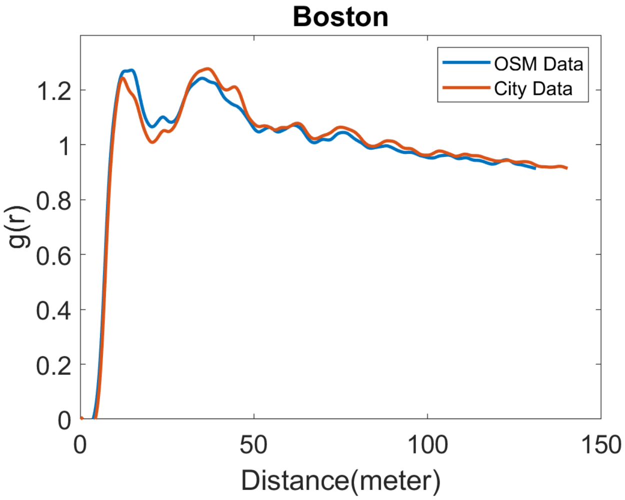

Figure 2-11: Radial distribution function for Boston using OSM and Data from GIS Department

MAE measures the average magnitude of the errors between two curves, without considering their direction. It's the average over the sample of the absolute differences between the two observed values, where all individual differences have equal weight,[2].

$$MAE = \frac{1}{N}\sum_{i=1}^{N} |g_i - g_i'| \tag{2.2}$$

where N = number of observations,

g_i = value of RDF taken from GIS departments,

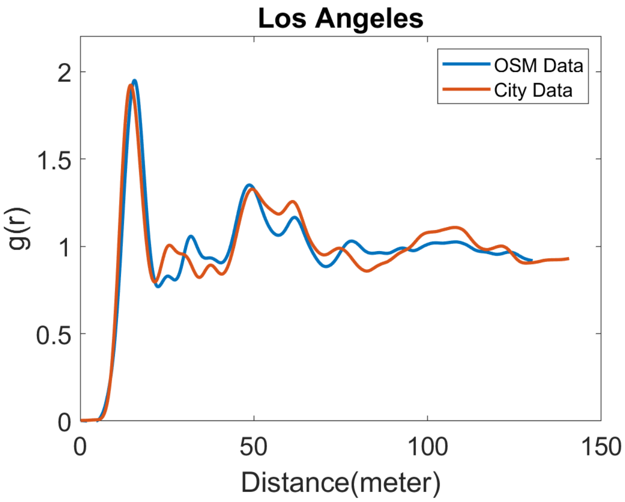

Figure 2-12: Radial distribution graph for Los Angeles using OSM and Data from GIS Department

g_i' = value of RDF taken from OpenstreetMap

Root mean squared error (RMSE):

RMSE is a quadratic scoring rule that also measures the average magnitude of the error. It's the square root of the average of squared differences between the two observed values,[2].

$$RMSE = \sqrt{\frac{1}{N}\sum_{i=1}^{N}(g_i - g_i')^2} \tag{2.3}$$

where N = number of observations,

g_i = value of RDF taken from GIS departments,

g_i' = value of RDF taken from OpenstreetMap

The values in the table show that a relatively minor percentage error is obtained between OSM data and the building footpritns obtained from GIS departments.

Comments to the errors

As it can be observed from table 2.2 for all four cities, the various error metrics MAE, RMSE, the difference Mean value and the difference in the standard deviation, have

City	MAE	Mean Diff	RMSE	Std diff
Boston, MA	0.0784	0.0011	0.1152	0.0033
Chicago, IL	0.0657	0.0024	0.1043	0.0157
Los Angeles, CA	0.1202	0.0068	0.1902	0.0078
New York, NY	0.0571	0.0098	0.0889	0.000168

Table 2.2: Error metrics

small magnitude in comparison with the actual values of the two examined curves, since the values of the error have the same units as the curves. That indicates that a high accuracy can be achieved using the OpenStreetmap data. Concluding the above is also possible by visualizing the computed rdf values for both approaches, as shown in fig. 2-4

2.5.4 Validation of OSM using g(r) parameters

In the context of cities, distances have been compared. To be exact, the first peak of g(r) has been used in order to obtain five variables: (1) the characteristic local cluster size, R, (2) the average distance between buildings, d, (3) average number of local buildings, C_n, (4) the local angular order of buildings, ϕ, and (5) the density of the local cluster, ρ local. These values are basic characteristics that can be obtained directly from g(r). The values of these parameters are shown in the tables 2.3 and 2.4. However, a more through explanation of these variables will come in chapter 3. For now, the comparison is between OSM and the data obtained from GIS departments, which were used in the previous study.

City	R(feet)	L(feet)	d(feet)	ϕ	Cn
Boston, MA	70.80	36.97	48.22	0.6347	2.7403
Chicago, IL	55.67	37.14	32.48	0.8357	2.2753
Los Angeles, CA	69.65	43.99	48.55	0.7012	2.3471
New York, NY	66.86	40.87	42.97	0.8178	2.2891

Table 2.3: Data from GIS Departments

City	**R(feet)**	**L(feet)**	**d(feet)**	ϕ	**Cn**
Boston, MA	67.94	43.00	50.31	0.3937	2.7895
Chicago, IL	46.45	38.39	30.71	0.4991	2.0056
Los Angeles, CA	72.56	42.68	51.22	0.4015	2.7412
New York, NY	68.24	37.29	40.72	0.4410	2.3754

Table 2.4: Data from OpenStreetMap

Comments to the parameter values

For the validation, the building data used was subject to the same procedure as in the publication[84], but with some changes. Buildings to points were not converted using the 2-D center of mass. That leads to a different location of point and also a difference in values in the local angular order of buildings.

Areas of merged buildings have been analyzed as well and the findings were, that in a logarithmic mode probability distribution function of buildings areas can be adequately captured with a bi-modal which forms distinction between unoccupied and occupied buildings, for instance garages and residential or commercial units, respectively,[84]. Despite all accurate data, the cut of point between garages and no garages was not clear, that means more or less buildings with different size was added to the sample. That leads to the slight differences in the average building size, the characteristic local cluster size, R, the average distance between buildings, d and the average number of local buildings. However the differences in the parameters are only slightly different and that can conclude to an eminent accuracy of OpenStreetMap data.

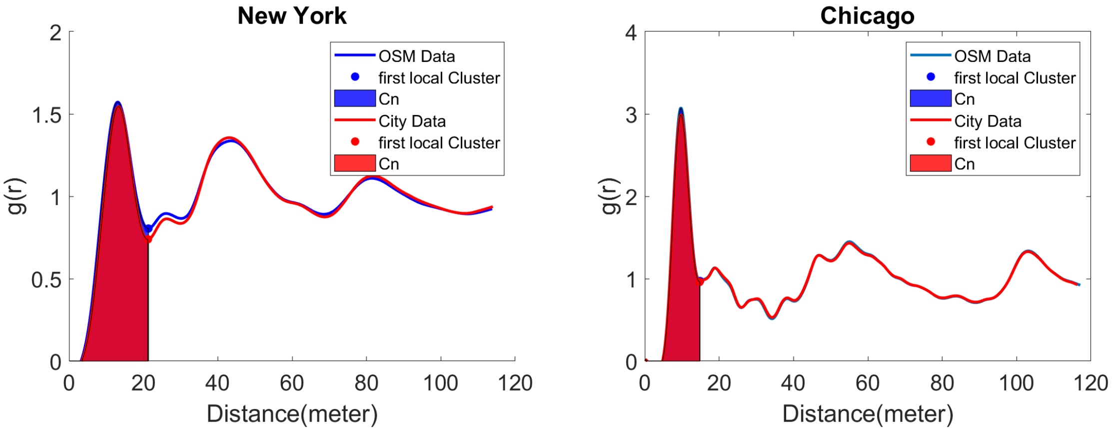

(a) RDF New York (b) RDF Chicago

Figure 2-13: Radial distribution function and Number of neighboring buildings

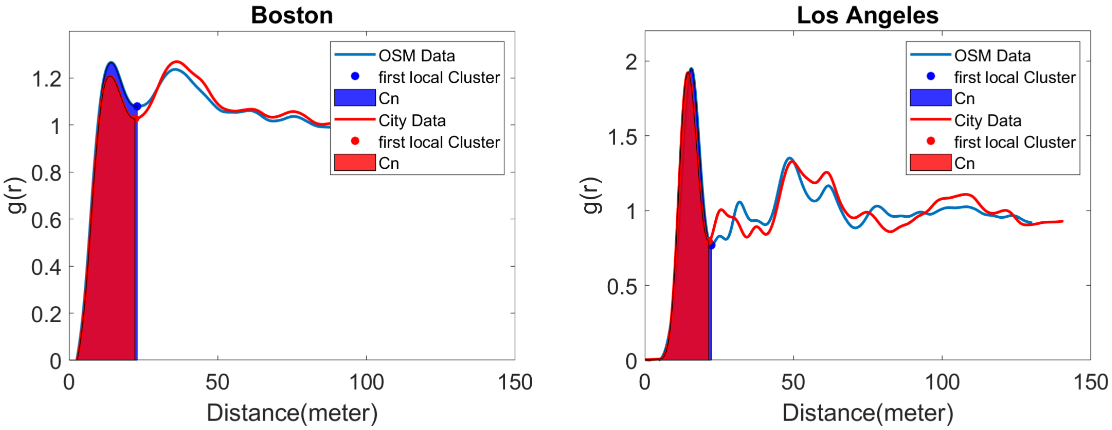

(a) RDF Boston (b) RDF Los Angeles

Figure 2-14: Radial distribution function and Number of neighboring buildings

2.6 Summary

In this chapter a new method of obtaining building data from OpenStreetMap has been established. The methodology of extracting building footprints and the pre and post processing of this approach is shown. The data is being validated by computing the radial distribution function and it's parameters and comparing these results to results of the GIS departments.

Chapter 3

Surface Urban Heat Island (SUHI) and city texture

3.1 Introduction

In this chapter the focus relies on the first research objective by quantifying surface urban heat island for 35 cities across the world. First the approach of separating the rural and urban areas will be introduced in order to calculate the land surface temperature for these two areas . As a final step, the correlation of city texture and SUHI will be analyzed. Throughout the remaining part of this thesis, surface urban heat island will be referred to as UHI.

3.2 Urban Heat Island UHI

UHI is a climate phenomenon that results in an increased air temperature in cities when compared to their rural surroundings. More than 50% of human population lives in the cities, urbanization has become an important contributor for global warming,[20]. Accurate quantification of UHI can help to efficiently evaluate the potential heat risk and to guide the city management and development for government and city planners. The surface UHI relies on the definition of urban and rural stations or pixels,[36]. UHI phenomenon may be evaluated by comparing the air temperature in urban and rural environments based on automatic and conventional weather stations and also by land-surface temperature (LST), usually obtained with thermal infrared (TIR) remote sensing data. On the one hand situ air temperature data have the advantage of a high temporal resolution and historical time series, but a low spatial resolution as well. On the other hand, remote sensing LST data have in general a low temporal resolution, but a high spatial distribution and it is more easily related to surface conditions. In fact, it is possible to retrieve biophysical land-surface characteristics and to describe urban environment materials based on remote sensing data. Consequently, remote sensing has the potential to improve understanding the UHI phenomenon and its effects, and several studies have been assessed UHI using LST retrievals, [73]. A previous approach has established the correlation between air UHI during nighttime and city texture. The goal of this thesis was to establish a correlation between Surface UHI during daytime and city texture. UHI has a greater impact in people's lives, the majority of people are outside during these hours and general life is more vivacious in cities during the day. SUHI is introduced here since it gives continuous information about the temperatures, where UHI in a previous research was based on temperature values of one station.

3.3 Satellite Data

3.3.1 LandSat Satellite

The LandSat satellite passes over the same place on earth every 16 days. Its orbit goes from pole to pole and captures a new place. It's been doing this for 40 years but since December 2008, they rewrote their data policy to one in which all LandSat data were available to anybody without restriction and at no cost. There have been a various LandSat satellites but on February of 2013 LandSat 8 was launched with a much higher resolution compared to any other satellite imagery. The resolution for previous LandSat 7 was 500m, while for LandSat 8 the resolution is 100m,[1]. That gives the opportunity to receive very accurate results and to calculate the land surface temperature. There are also other satellite data such as, MODIS which has been used in many researches for quantifying the UHI phenomenon,[?], however LandSat 8 has the highest resolution.

Landsat 8 measures different ranges of frequencies along the electromagnetic spectrum of a color, although not necessarily a color visible to the human eye. Each range is called a band, and Landsat 8 has 11 bands. Landsat numbers its red, green, and blue sensors as 4, 3, and 2, so when we combine them we get a true-color image,[63].

Data are collected by the instruments onboard, using two primary imaging instruments. Landsat 8 carries two push-broom instruments: The Operational Land Imager (OLI) and the Thermal Infrared Sensor (TIRS), [1]. More specifically OLI acquires images of the earth's surface in nine different bands of visible and invisible (infrared) radiance. Bands 4,5 which are used in this thesis have a 30 meter resolution. These are used to calculate the Normalized Difference Vegetation Index, explained during the methodology. The TIRS gathers images of the earth's surface in two infrared (thermal) bands , band 10 and 11. that are particularly useful providing accurate surface temperatures of the planet's land areas,[1].

3.4 Methodology for SUHI Calculation using satellite imagery

3.4.1 Data Collection

First step of this approach is to collect the data. The city selection is based on the cities in chapter 2. As mentioned above the Satellite has been launched since 2013, thus the available data are limited. The collection of data depends on weather conditions and quality restrictions. Satellite images for temperature over zero degrees were chosen to eliminate the possibility of ice and snow on the images, since the method calculating the Land Surface Temperature does not include these phenomena. The US Geological Survey includes a quality assessment, which contains quality statistics gathered from the image data and cloud mask information for the scene. A quality assessment band improves the integrity of science investigations by indicating which pixels might be affected by instrument artifacts or be subject to cloud contamination. In the methodology chosen an important index is the Normalized Difference Vegetation Index (NDVI) and it has been noticed that, while calculating it over pixels that contain clouds it shows anomalous values. If such pixels were included in a phenology study, the results might not show the true characteristics of seasonal vegetation growth. Cloud-contaminated pixels will lower NDVI values and measures such as the timing of 'green up' or peak maturity would appear later than they actually occurred,[3].

These anomalies of NDVI led to a more strict data selection, making the task of collecting a clear not cloudy snapshot for north European countries, difficult. Some of them were constricted to maximum two satellite images. For cities like Athens, Rome, Boston the weather conditions during spring and summer made it possible to download more than 15 satellite images. Another reason of data availability restriction has been smog. This phenomenon was very extent in the city of Singapore, for which only one acceptable image could be obtained.

3.4.2 Separation of Urban and rural area.

The first step was to define the boundaries of rural and urban area. A first attempt was to scale the boundaries of the city. This seems to be a satisfactory approach for cities with a circular shape, such as Berlin, Paris and London, but for cities like New York and Athens this could not be applied. The explanation to that is based on the fact, that these boundaries were mainly expanded in one direction and the rural area wasn't homogeneous in all direction.

That led to the solution of using a buffer, which radius is computed by increasing the city boundaries up to 25 km. The buffer size or in other words the boundaries between rural and urban area is an approximation, based on similar researches and observation of the satellite data,[21]. This distance was the minimum to have sufficient rural data. Using a bigger buffer increased the risk of overlapping with other urban areas.

This method has been implemented in an automatic manner, by combining OpenStreetMap boundaries and satellite imagery.

- The boundaries of the city are dissolved, that means merged into one polygon, projected and transformed into meters after that the area of the boundaries can be calculated. Assuming that the area represents a circle the hypothetical radius has been calculated.
- The polygon boundaries are represented as a point, which is the center of mass.
- The next step is to create a buffer. The center of the buffer is the point created in previous steps and the radius= hypothetical radius + 25 km
- The last step is to create the two different boundaries, for rural and urban area. This is done by taking the symmetrical difference between the buffer and the city boundaries. The results are shown in the pictures below.

Figure 3-1: Buffer Boundaries of Athens

3.4.3 Land Surface Temperature Method

This methodology has also been applied in an automated manner using python and ArcGIS, functions. The required inputs are the rural and urban boundaries from the previous methodology and the downloaded satellite data. The workflow of this methodology is shown in the figure below.

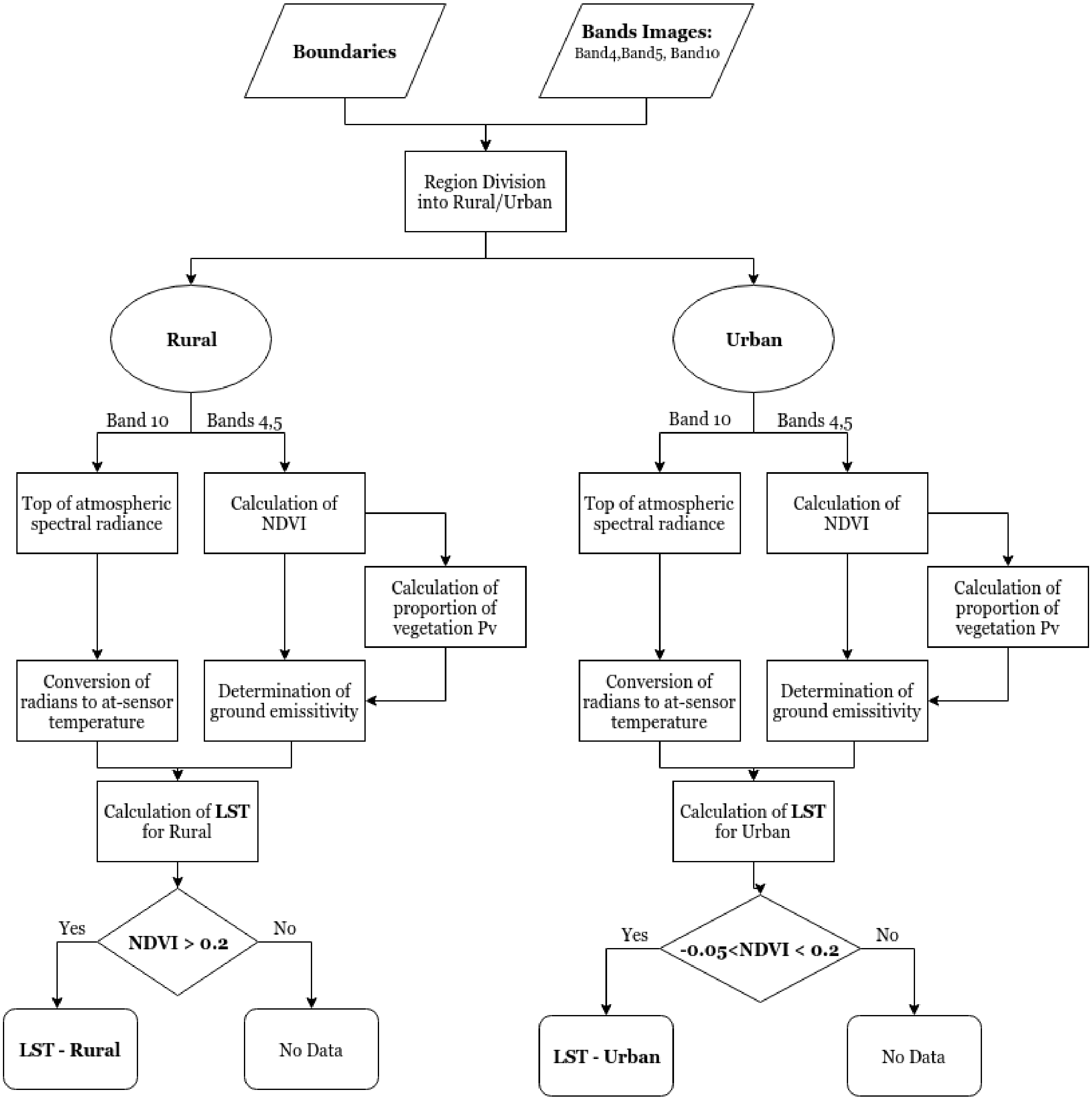

Figure 3-2: General Workflow for LST computations

- To calculate mean temperatures for rural and urban areas, the satellite images have been 'cropped' by using the specified boundaries. This was applied on all necessary bands for these calculations. The use of bands is shown in further steps.

- To extract temperature values of the pixels we follow the method provided by

USGS. .

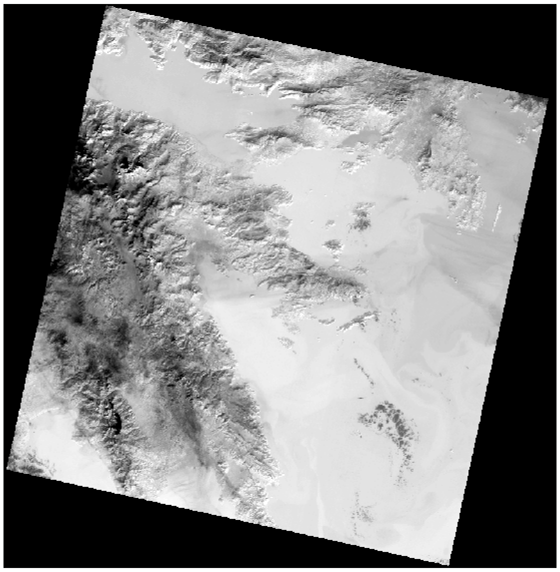

Figure 3-3: Satellite image for Athens

(a) Satellite image Athens urban

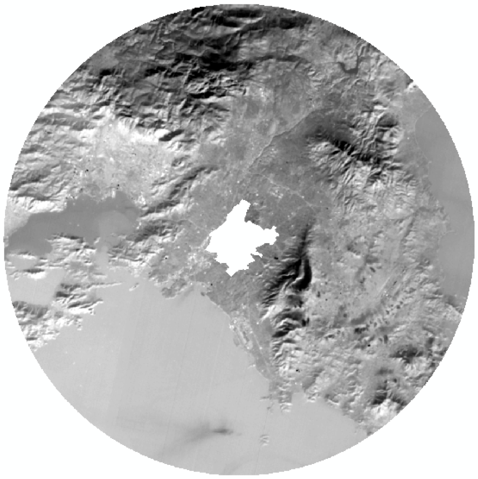

(b) Satellite image Athens rural

STEP 1- Top of Atmospheric Spectral Radiance

OLI and TIRS at Sensor Spectral Radiance Images are processed in units of absolute radiance. Afterwards these values can be converted to spectral radiance using the radiance scaling factors provided in the metadata file [5]:

The first step of the algorithm is the input of Band 10. After inputting band 10, in the background, the tool uses formulas taken from the USGS web page for retrieving the top of atmospheric (TOA) spectral radiance (L_λ) [12]

$$L_\lambda = M_L * Q_{cal} + A_L \tag{3.1}$$

where: L_λ = Spectral radiance ($\frac{W}{m^2*sr*\mu m}$)

M_L = Radiance multiplicative scaling factor for the band from the metadata

A_L = Radiance additive scaling factor for the band from the metadata

Q_{cal} = is the thermal infrared sensor Band 10 data.

STEP 2-Conversion of Radiance to At-Sensor Temperature

After the digital numbers (DNs) are converted to reflection, the TIRS band data are converted from spectral radiance to brightness temperature (BT) using the thermal constants provided in the metadata file. The following equation is used in the algorithm to convert reflectance to BT,[12].

TIRS Top of Atmosphere Brightness Temperature (TIRS) data can also be converted from spectral radiance (as described above) to brightness temperature, which is the effective temperature viewed by the satellite under an assumption of unity emissivity. The conversion formula is as follows:

$$BT = \frac{K_2}{ln(\frac{K_1}{L_\lambda} + 1)} \tag{3.2}$$

where: BT = TOA Brightness Temperature, in Kelvin.
L_λ = Spectral radiance ($\frac{Watts}{m^2*sr*\mu m}$)
K_1 = Thermal conversion constant for the band from the metadata
K_2 = Thermal conversion constant for the band from the metadata) [5]

STEP 3- NDVI Method

Remote sensing phenology studies use data gathered by satellite sensors that measure wavelengths of light absorbed and reflected by green plants. Certain pigment in plant leaves strongly absorb wavelengths of visible (red) light. The leaves themselves strongly reflect wavelengths of near-infrared light, which is invisible to human eyes. As a plant canopy changes from early spring growth to late-season maturity and senescence, these reflectance properties also change,[11]. By transforming raw satellite data into NDVI values, researchers can create images and other products that give a rough measure of vegetation type, amount, and condition on land surfaces around the world,[11] Although there are several vegetation indices, one of the most widely used is the Normalized Difference Vegetation Index (NDVI). NDVI values range from +1.0 to -1.0. Areas of barren rock, sand, or snow usually show very low NDVI values (for example, 0.1 or less). Sparse vegetation such as shrubs and grasslands or senescing crops may result in moderate NDVI values (approximately 0.2 to 0.5). High NDVI values (approximately 0.6 to 0.9) correspond to dense vegetation such as that found in temperate and tropical forests or crops at their peak growth stage,[11].

Landsat visible and near-infrared bands are used for calculating the Normal Difference Vegetation Index (NDVI). The calculation of the NDVI is important because, afterward, the proportion of the vegetation is calculated, and is highly related with the NDVI, and emissivity.

$$NDVI = \frac{NIR - R}{NIR + R} \tag{3.3}$$

:where NIR represents the near-infrared band (Band 5) and R represents the red band (Band 4)[12].

STEP 4- Emissivity Correction using NDVI Method

The land surface emissivity (LSE) must be known in order to estimate LST, since the LSE is a proportionality factor that scales blackbody radiance (Planck's law) to predict emitted radiance, and it is the efficiency of transmitting thermal energy across the surface into the atmosphere,[14]. The determination of the ground emissivity is calculated conditionally as suggested in [15]:

$$\epsilon_\lambda = \epsilon_{v\lambda} * P_v + \epsilon_{s\lambda} * (1 - P_v) + C_\lambda \tag{3.4}$$

$$\epsilon_\lambda = \begin{cases} \epsilon_{s\lambda}, & NDVI < NDVI_s \\ \epsilon_{v\lambda} P_v + \epsilon_{s\lambda}(1 - P_v) + C & NDVI_s \leq NDVI \leq NDVI_v \\ \epsilon_{sl} + C & NDVI \geq NDVI_v \end{cases}$$

Where $\epsilon_{v\lambda}$ and $\epsilon_{s\lambda}$ are the vegetation and soil emissivities, respectively. The condition can be represented with the following formula. When the NDVI is less than 0, it is classified as water, and the emissivity value of 0.991 is assigned. For NDVI values between 0 and 0.2, it is considered that the land is covered with soil, and the emissivity value of 0.996 is assigned. Values between 0.2 and 0.5 are considered mixtures of soil and vegetation cover and (6) is applied to retrieve the emissivity. In the last case, when the NDVI value is greater than 0.5, it is considered to be covered with vegetation, and the value of 0.973 is assigned,[12].

STEP 5- Land Surface Temperature

Using the corrected emissivity values the land surface temperature has been calculated.

$$LST = \frac{BT}{1 + (\frac{\lambda * BT}{\rho} * ln(\epsilon_\lambda)} \tag{3.5}$$

where the LST is in Celsius (○C), BT is at-sensor BT (○C), $\lambda = 10.895$ is the wavelength of emitted radiance, is the emissivity ϵ_λ and

$$\rho = h * \frac{c}{\sigma} = 1.438 * 10^{-2} m * K \tag{3.6}$$

where σ is the Boltzmann constant ($1.38 * 10^{23} J/K$), h is Planck's constant ($6.626 * 10^{34} J * s$), and c is the velocity of light ($2.998 * 10^8 m/s$) [18].

STEP 6- Mean Temperature values for rural and urban areas

An additional use of NDVI has been established to separate the green and urban areas. To calculate the mean temperature of urban and rural areas an additional constraint is added into the algorithm. For rural areas buildings or non-vegetation data are converted into no data values and respectively the same procedure is used for urban areas, where parks and green areas are eliminated. The importance of that step is based on the lower temperatures of green areas and higher temperatures of buildings and street. For example by adding central Park into the urban temperature would decrease the mean temperature of the city. UHI is calculated as the difference of these mean values.

3.5 Results

3.5.1 Land Surface Temperature and NDVI maps

The results of this procedure are first of all satellite images with the temperature values in their pixels. Two cities of the 35 cities are presented in the figures below. As the figure for Athens depicts, even with a 25 km radius outside the city boundaries many areas there are still a few areas with high temperature values. Areas like Elefsina where many industries are located, such as the Greek oil companies, have also high temperature values. The white values on the images are pixels with no data. It can be noticed, that there are bigger areas on the map with no data in Athens. As described in the previous step for rural areas all non-vegetation areas or in other words all the pixels in rural areas which are buildings or steets are eliminated. This can also be verified by observing the NDVI figure of Athens. This actually shows which areas are green in the rural area and which areas are covered with buildings. Paris on the other hand has a much clearer distinction between rural and urban area. The white values which are no-data, on the rural area of Paris are around the city where buildings are located. In the urban area the no data areas are parks and green areas. The distinction between the areas can be observed as already mentioned on the NDVI figure of Paris.

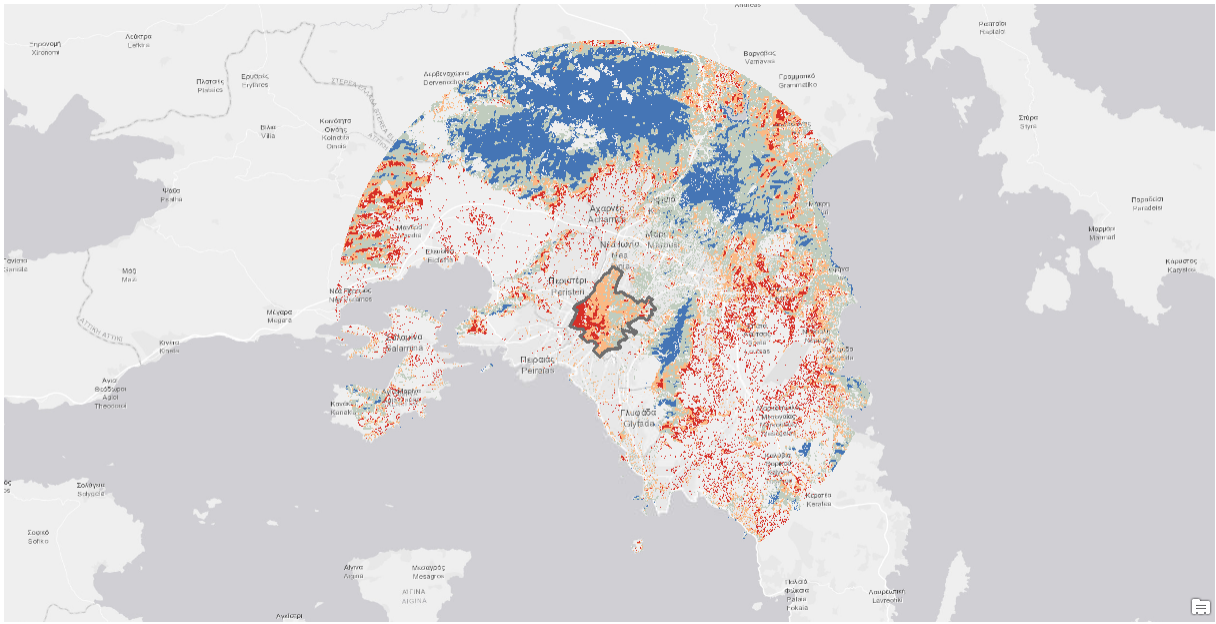

Figure 3-5: Land surface Temperature Athens

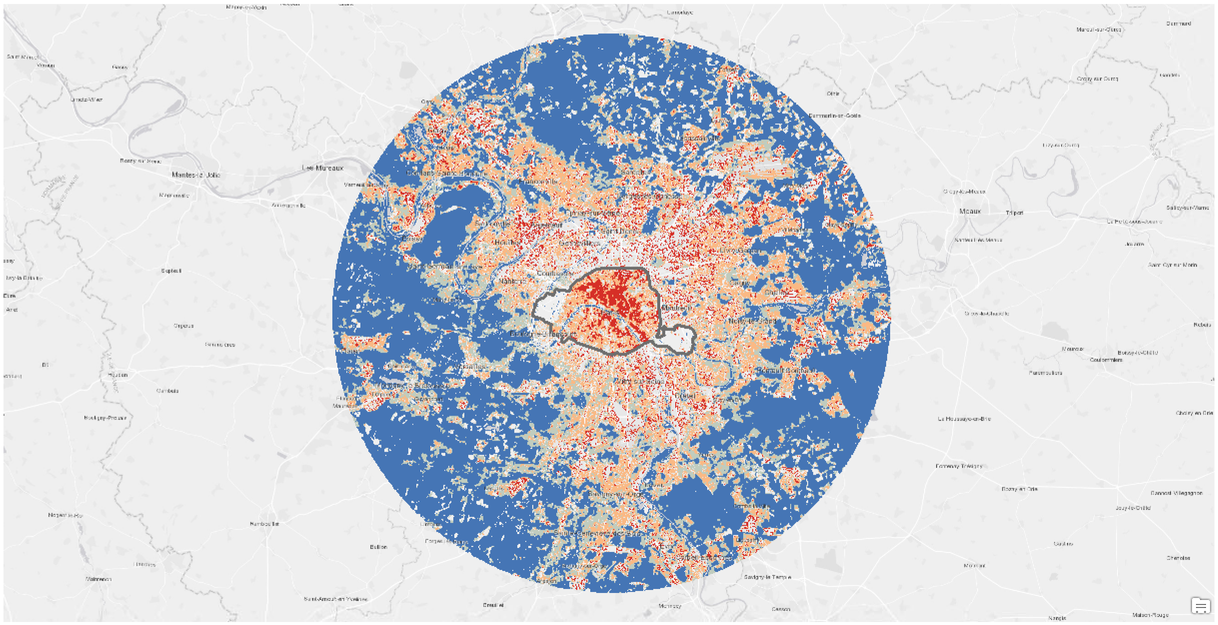

Figure 3-6: Land surface temperature Paris

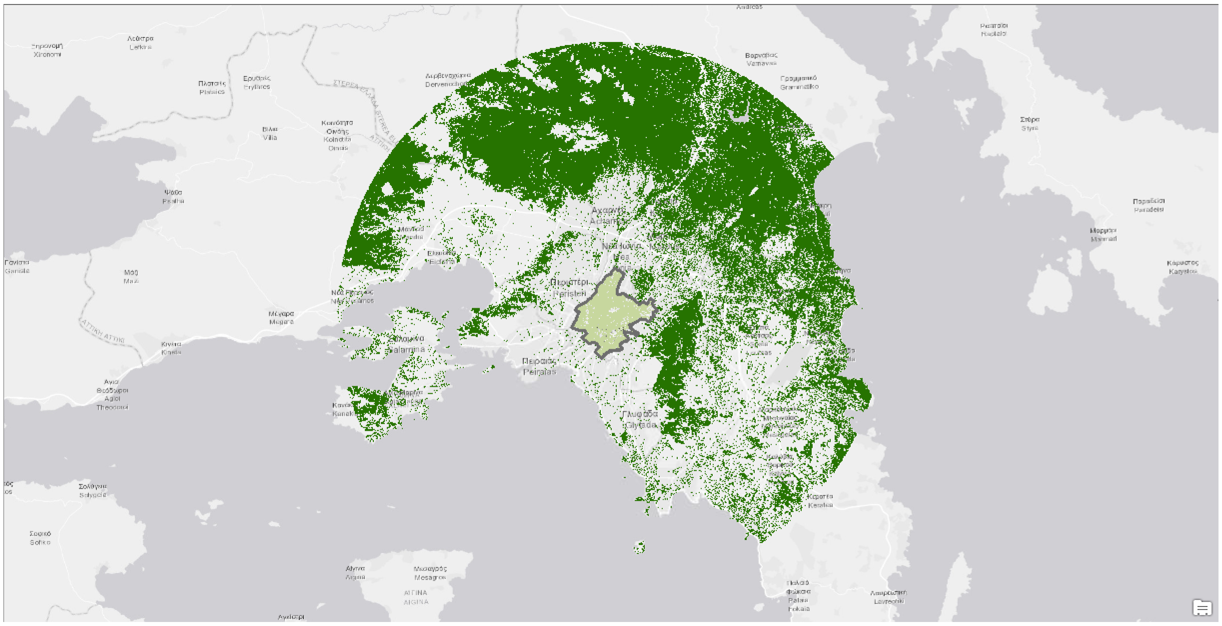

Figure 3-7: NDVI for Athens

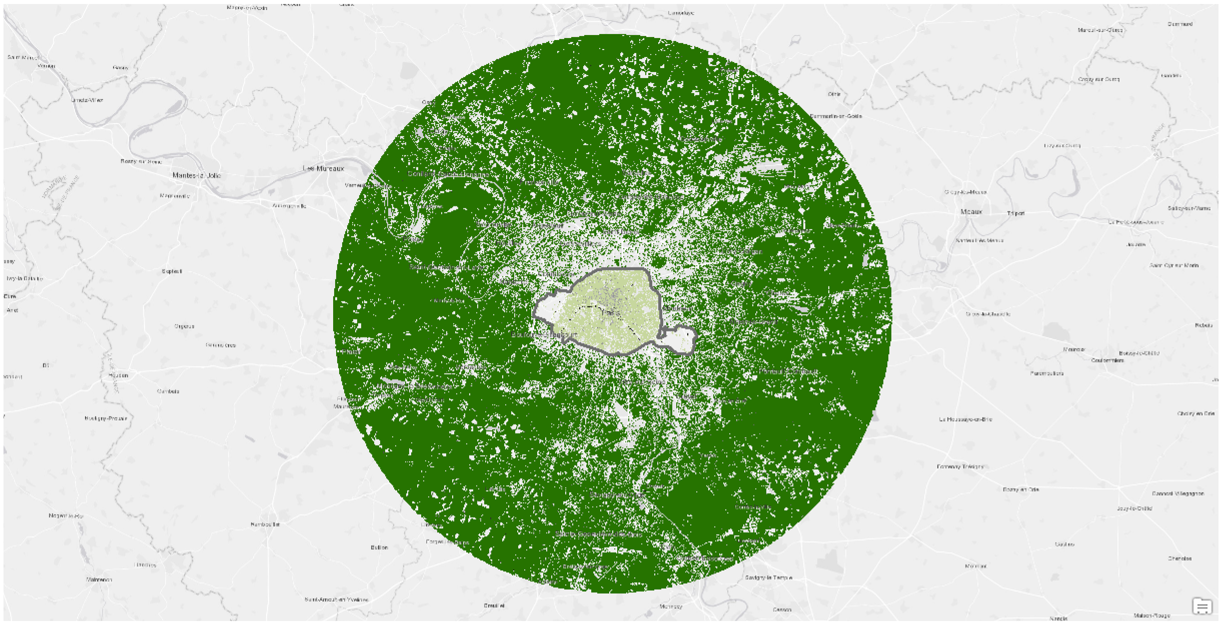

Figure 3-8: NDVI for Paris

3.5.2 UHI observations

An interesting outcome of this analysis is the correlation of temperature and the UHI. As shown in the graphs below, there is a linear correlation between rural and urban temperature. That means that as the rural temperature increases the temperature difference between urban and rural temperature increases. This might not have a huge effect on low temperatures, but for 30 degrees in rural area for cities such as Rome or Prague, that concludes a rural temperature of 35 degrees. Worth mentioning and reminding, this difference is UHI. This outcome highlights the UHI phenomenon. The graphs for all 35 cities are shown below. The tables illustrate the values of mean temperature for Athens and Paris and the standard deviation for which the images were calculated. The data for the other 32 cities are available in appendix A.

Date	**MeanTsR**	**MeanTsC**	**stD_TsR**	**stD_TsC**	**UHI**
2014/01/11	13.37	12.47	1.51	0.66 s	-0.90
2014/03/16	16.77	17.95	2.01	1.16	1.17
2014/04/01	20.97	21.45	2.45	1.26	0.47
2014/07/06	32.86	34.71	3.06	1.25	1.85
2014/07/22	31.10	32.27	2.31	1.04	1.16
2014/08/23	34.14	34.74	2.23	1.12	0.59
2015/01/14	10.03	8.78	1.70	0.71	-1.24
2015/05/06	27.54	29.45	3.54	0.83	1.91
2015/07/09	34.04	35.38	2.96	1.08	1.33
2015/07/25	33.39	33.75	2.82	1.09	0.35
2015/10/13	21.92	23.67	2.16	1.02	1.75
2015/11/30	12.01	12.48	2.09	0.72	0.47
2016/02/02	17.03	16.20	1.69	0.85	-0.82
2016/03/05	16.04	17.11	2.54	1.18	1.06
2016/03/21	17.47	18.93	2.06	1.08	1.45
2016/04/06	24.88	26.80	2.50	1.39	1.91
2016/04/22	24.81	27.08	3.50	1.50	2.26
2016/07/11	31.42	33.13	2.90	1.05	1.70
2016/07/27	30.44	32.83	2.73	1.20	2.39
2016/08/12	31.21	33.01	2.47	1.13	1.80
2016/09/29	24.37	25.55	2.89	1.29	1.17
2016/12/18	7.52	7.22	2.36	0.78	-0.29
2017/01/03	10.79	9.22	2.10	0.76	-1.56
2017/03/24	21.27	23.38	2.66	1.43	2.11
2017/04/25	23.55	23.93	3.10	1.28	0.38
2017/07/14	30.82	32.63	2.44	0.83	1.81
2017/07/30	32.27	34.25	2.90	1.17	1.98
2017/09/16	31.22	32.03	2.83	1.19	0.81
2017/12/05	11.47	12.00	2.33	1.08	0.52
2018/01/06	12.05	11.16	1.46	0.69	-0.89

Table 3.1: UHI values for Athens, where MeanTsR is the mean temperature of the rural area, MeanTsC the mean temperature of the urban area, std is the standard deviation for urban and rural temperatures

FileName	**MeanTsR**	**MeanTsC**	**stD_TsR**	**stD_TsC**	**UHI**
2014/02/12	4.88	5.83	1.26	0.64	0.95
2014/03/16	15.33	16.84	1.31	1.14	1.51
2014/05/19	24.07	28.58	3.20	1.65	4.51
2014/09/08	20.80	24.13	3.04	1.11	3.33
2014/11/11	8.91	9.216	1.06	0.568	0.30
2015/04/20	20.57	24.19	3.87	1.45	3.62
2015/06/07	17.71	24.85	4.77	1.87	7.14
2015/09/27	16.97	18.47	1.34	0.95	1.49
2016/06/09	21.76	27.25	3.40	1.54	5.48
2016/10/15	12.01	12.84	1.03	0.99	0.82
2016/10/31	11.53	11.59	1.05	0.84	0.05
2017/01/19	0.33	0.36	0.36	0.32	0.03
2017/04/09	23.62	26.15	2.08	1.62	2.53
2017/05/27	26.66	31.35	3.11	1.62	4.68
2018/02/23	2.28	3.50	1.01	0.86	1.21

Table 3.2: UHI values for Paris, where MeanTsR is the mean temperature of the rural area, MeanTsC the mean temperature of the urban area, std is the standard deviation for urban and rural temperatures

3.6 Summary

Using satellite data is the most common approach for obtaining Land Surface Temperatures and subsequently land surface UHI. The way that UHI is always calculated is by taking the difference between urban and rural areas. Resulting, this means that rural areas in the daytime are significantly cooler than urban areas. An outcome is as well that UHI increases with temperature. It can be taken as given, that this slightly different way of thinking about UHI, hasn't been taken into consideration yet.

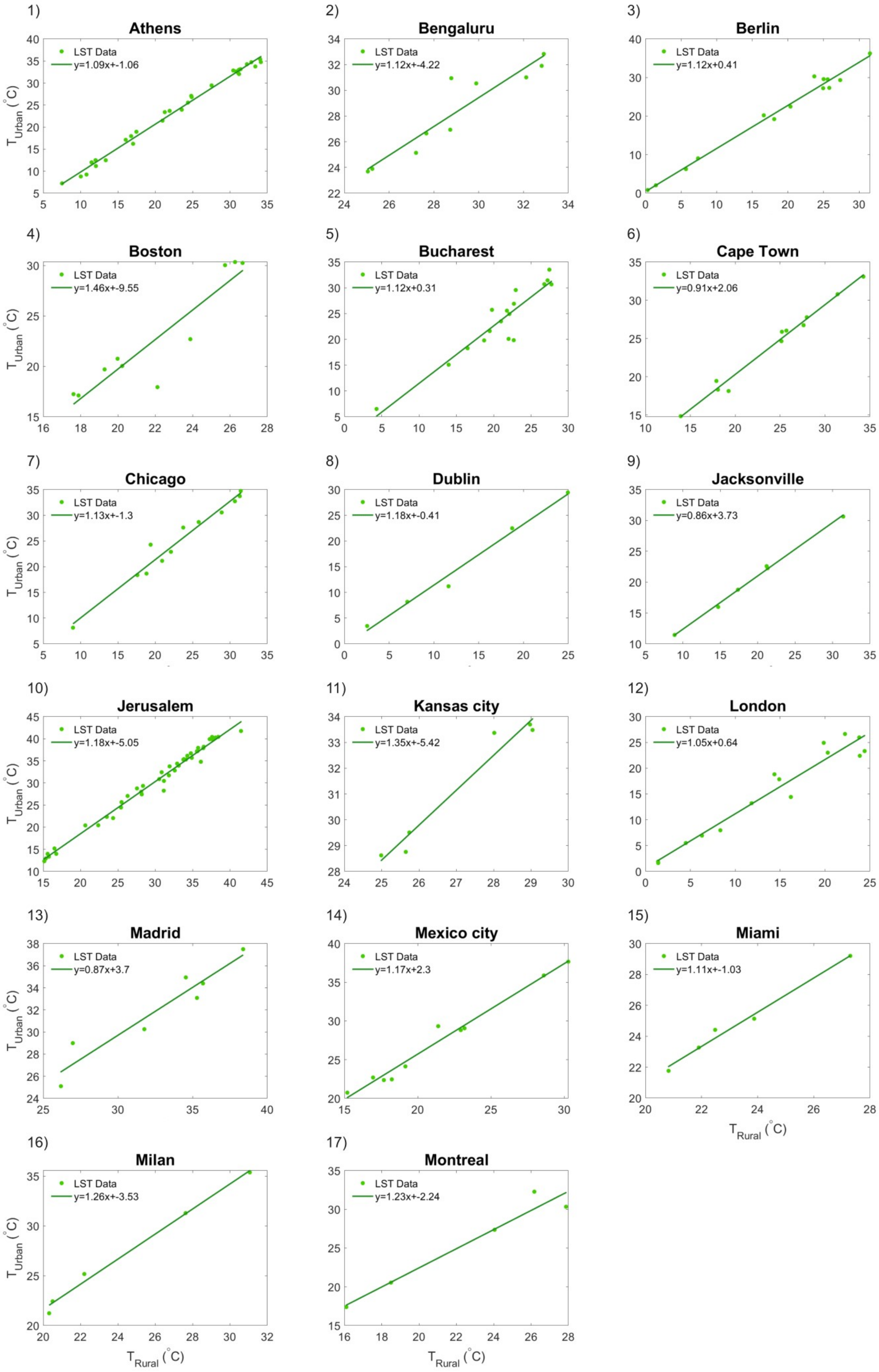

Figure 3-9: Correlation Rural and Urban Temperature

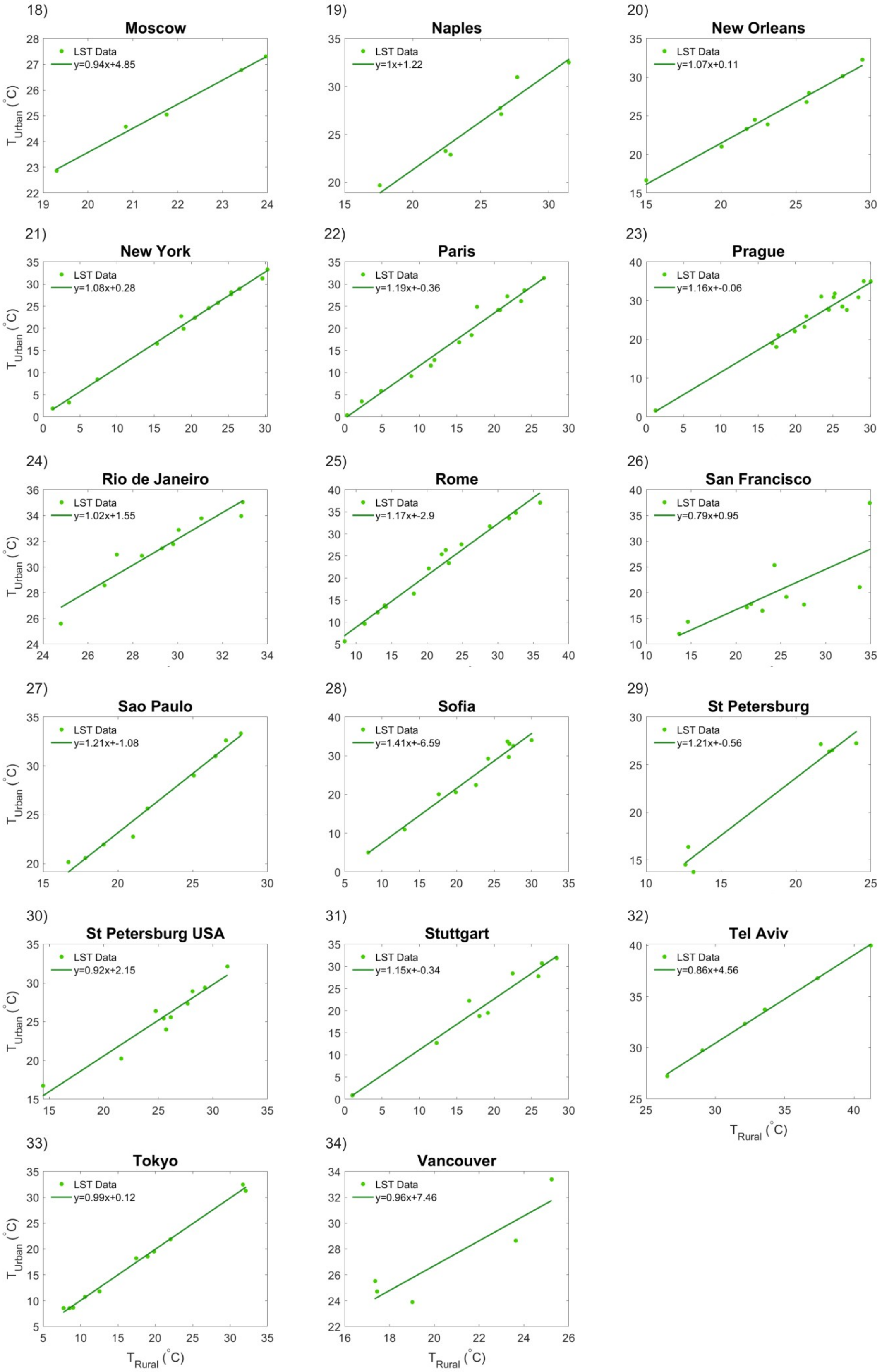

Figure 3-10: Correlation Rural and Urban Temperature

Chapter 4

Radial distribution function

4.1 Introduction

This chapter begins with instituting the parallel between molecular physics and urban designs, an analogy which allows us to utilize tools typically seen being used only in the field of statistical physics. It will be started with a global approach to quantifying cities, by using the radial distribution function, g(r). This chapter closes up by explaining the usage of g(r) in modeling of cities and its correlation with UHI effect.

4.2 Definition of Radial distribution function, g(r) in cities

The radial distribution function g(r) describes how the local density at a distance from the reference particle varies from the global average. Traditionally, it has been used to investigate the atomic-scale structure of condensed matter. In the context of buildings, g(r) is the probability of finding a building at distance r from the reference building relative to the average. The density in the statistical physics is the average density of particles, which are similar in size. This poses some limitations when this method is utilized for cities, where buildings across the whole urban network may have significant variation of sizes. As a results, an average building size L is obtained and is assumed to be a representative particle size. Peaks in g(r) appear when the local density of buildings deviates from the average density of a system. These peaks can be studied to extract information about sizes of building clusters using a function's minima. The distance at which g(r) reaches its first minimum is defined as the local cluster size R. Such a defined cluster size is critical in deriving city texture parameters, namely, the number of local neighbors, average distance between them, local density, and angular distortion between buildings that is captured with the local 2-D Mermin order parameter. More specifically, utilizing g(r) to quantify city texture, it comes out that cities have distinct textures that resemble structures of crystals, liquids, or gases,[84].

Correlation of urban and particle physics:

In order to extract statistical characteristics the structure of cities will be correlated to the structure of particles. These have been coalesced with an analogy between buildings and particles. The fundamental information derived from RDF is the probability of finding a neighboring particle or building at a given distance from the reference point. As soon as local density deviates from the average density of a system, peaks in the distribution eventuate; in statistical particle physics terms, this is explained as the probability of finding an atom at distance r from the reference atom relative to randomly distributed system of atoms that at large distances converges to unity. Those terms utilized at the city scale allow as to define the average building density as:

Using this analogy allows to construe data given by the radial distribution function in order to understand the structure of the city. The necessary metrics to model the city is the building density, the average building size, the coordination number and the local density, which will be explained more thoroughly below. Average building density is defined as the ratio of the Number of buildings divided by the overall area of the city,[84].

$$\rho = \frac{N}{A} \tag{4.1}$$

where N is the total number of buildings and A is overall area of the city. This density measure is the fundamental density used in g(r) calculations defined as:

$$g(r) = \frac{1}{N} \sum_{i=1}^{N} \frac{n_i(r+dr) - n_i(r)}{\bar{\rho}_{city} 2\pi r \times dr} \tag{4.2}$$

where $n_i(r)$ denotes the number of buildings within the radial distance r from building i. Moreover, dr is the distance increment, which for RDF calculations has been chosen to be 5% of the average building size, L. That is:

$dr = 0.05L$ [4.6] $= exp(Nlog(A_i))$ [4.7] where N is the total number of buildings and A_i is the area of building i.

$$L = \exp(\frac{1}{N} \sum_{i=1}^{N} \sqrt{log(A_i)}) \tag{4.3}$$

For buildings (and cities) the first minimum of g(r) is representative of the characteristic size, R, of the local cluster, where the density of buildings within the cluster deviates strongly from the average of the system,[84] .Rmax can be calculated only for the sample of cities whose structure is following a pattern of crystals or liquids. For cities with structure of gases, it generally is not possible to calculate the first minimum as the function does not reach a minimum.

The first peak of g(r) has one more property; it quantifies the distance at which g(r) reaches its maximum. In the context of cities this is the characteristic distance, d between the building of reference and its first shell of local neighbors Cn. Since for g(r) analysis we consider buildings as particles with no size, d is the distance between buildings' centers of mass, which is not the shortest distance between walls of two buildings,[84]. We find that there is a strong correlation between R and d that is captured by the mean relation d = 0.72*R.

The Coordination Number Cn, is the number of nearest neighbors situated around the central atom in a molecule or crystal at an average distance between them, d,[84]. In the context of g(r), Cn is defined as the area under the first peak of the function. Applied to the two dimensional city texture, it can be generalized to:

$$C_n = 2pi\bar{\rho_{local}}\int_0^{rmax} rg(r)dr \tag{4.4}$$

where rmax is the distance where g(r) reaches its first minimum. In order to be able to calculate Cn the local density of buildings, local density has to be known $\bar{\rho_l}ocal$: The local density of buildings, which is defined as:

$$\bar{\rho_l}ocal = \frac{1}{n}\sum_{i=1}^{n}\frac{N_i}{A_r} \tag{4.5}$$

where N_i is the number of buildings within local area Ar defined by circle with radius, rmax from g(r).

4.3 Issues with Radial Distribution Function

This method of modeling cities has been established in previous work, where the areas of calculating the radial distribution function and its parameters were restricted to a 3-miles buffer. In this approach we quantify g(r) for the entire city. A first approach was using the same method as described in the common paper,[84]. However, this approach could not be used, which led to three changes that have been applied to correct and adjust the method to a larger scale such as the entire city.

As already mentioned in the methodology of converting osm data into points, buildings are not getting merged (methods known as dissolving) since the number of buildings has been reduced significantly for many cities in Europe. Thus, merging buildings that share a wall would not be able to provide statistically sufficient size samples for g(r) calculations.

Another reason why this approach could not be used is that g(r) would not converge to 1, which by definition should converge for an infinite system when local density transitions to the global average. To solve that, a different approach was based on the assumption that it does not converge to 1 is caused by the boundary effect. This happens because buildings close to the boundaries do not have enough neighboring buildings to define the local g(r). Buildings near the city boundary have fewer neighbors than buildings inside the city. At long distance local density becomes average density and thus g(r) should converge to 1. Focusing on the boundary effect and the main effect which came from the city boundaries was not the solution but the results improved slightly. The approach of removing the boundaries effect for city of Jerusalem is shown in the next figure. The criterion to reduce the boundaries effect is based on the rcut distance, which is the 15 meters radius buffer for which every point is calculating the g(r). The polygon-boundaries created, is reduced by this distance rcut. The points in the ring are just used as neighboring buildings.

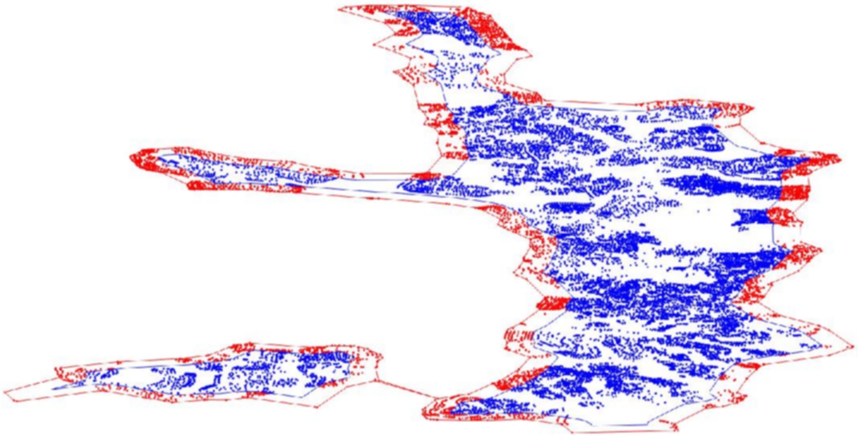

Figure 4-1: Removal of the boundaries effect for city of Jerusalem

However, reducing boundaries did not sufficiently improve g(r), which would continue to converge to a value slightly different than 1. The possible reason for multiple areas inside the city, where there are not as many buildings as in other parts of the city, would be counted in the density calculations. As a result, the global g(r) function, the average of all local g(r), at a longer range is lower than 1. This distort of g(r) is eliminated by clustering buildings in the city. There are multiple clustering algorithms available. The one selected is a common K-means clustering algorithm, which assigns buildings to a cluster with the nearest to a given building average centroid value. The number of clusters, K, are input user values, which in the context of cities, have the ability to significantly alter areas as it is shown in the figures for increasing number of clusters. This approach does not differ in accuracy compared to the previous published approaches as the small buffers, which has been used to quantify the radial distribution function is translated here into neighborhoods, the created clusters.

$$\Delta A_{cluster} = \frac{a(x_{i-1}^b - x_i^b)}{ax_{i-1}^b + c} 100\% \tag{4.6}$$

where $ax_i^b + c$ is a cluster area fitting function for cluster i

if $\Delta A_{cluster} < 1\% \Rightarrow A_{cluster} = ax_i^b + c$

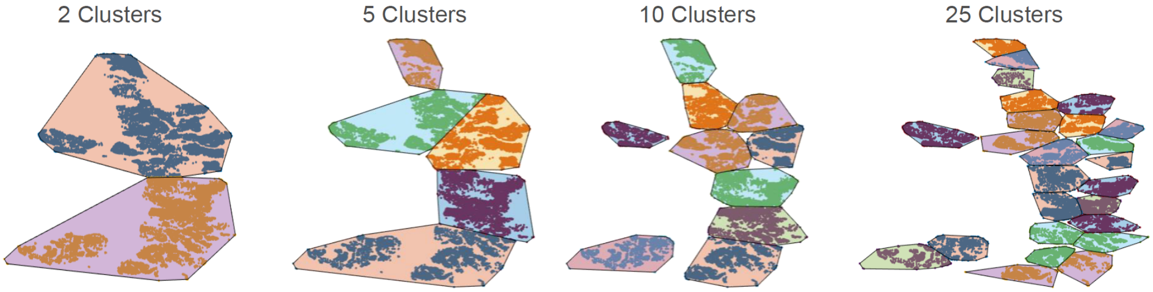

Figure 4-2: K-means clustering for city of Jerusalem

Clusters can be thought of as being neighborhoods. But at least 25 clusters are needed to eliminate the empty areas in the central part of the cities. It is no argument that clustering can help to obtain the right value for city density. To get the appropriate values the number of cluster has to be defined. It turns out that the city area, defined as the total area of all clusters follows a power decay for the increasing number of clusters, which is shown with blue line in figure 4-3.

4.3.1 Categorizing the cities by texture

As mentioned above the g(r) function can give information about the structure of the city after calculating the revised radial distribution function by getting the results shown in the graphs below. Cities that have structures similar to crystals are listed in the first table, observing the figures of these cities, g(r) patterns have numerous peaks multiple and narrow peaks, characteristics for liquids are widely spread, smooth and

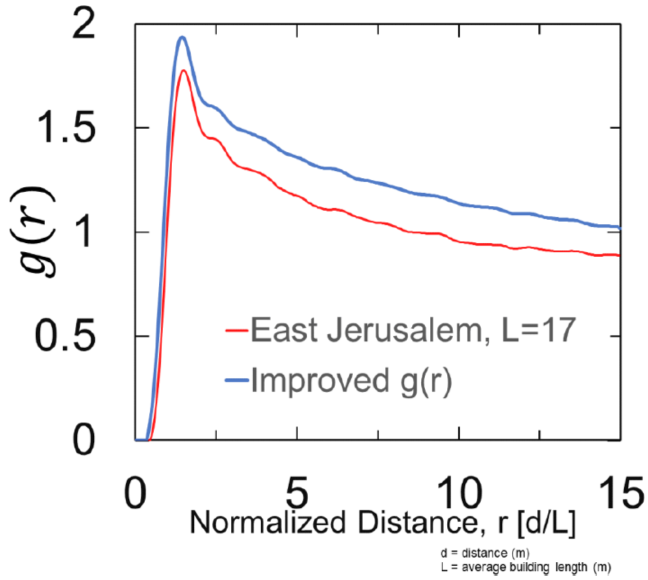

Figure 4-3: K-means clustering for city of Jerusalem

limited several peaks. For gases, cities in the table, have a single and not so easily evident peak, which means that they lack any type of structural order,[84].The graphs of g(r) are shown in figures .

Using the radial distribution function of gases, it is not possible to find the local cluster since there is no first minimum, which is a challenge since there are 15 cities which have such distribution. This first local cluster has been used to correlate the city texture to UHI in previous publications,[84]. However there has been found a strong linear correlation between the distance between buildings and the cluster size as shown in the next graph. This allows obtaining additional city texture parameters, mainly Cn and order parameter. While, there is no theory in statistical physics that would correlate Cn with ϕ, for the 35 cities it can be confirmed that there is a strong relationship between the inverse of ϕ and Cn.

Using the methodology above the radial distribution function results as shown in the figures below and the parameters are calculated.

Cities	**Structure**	**R(m)**	**d(m)**	**L(m)**	**rho**	**C_n**	**phi**
Athens	L	16.15	10.33	12.91	0.52	2.48	0.43
Bengaluru	L	11.81	10.33	9.84	0.29	2.68	0.41
Berlin	G	9.18	6.66	12.12	0.31	12.65	0.31
Boston	L	21.85	15.45	10.66	0.30	3.20	0.37
Bucharest	G	45.52	31.29	14.22	0.39	9.00	0.18
Cape Town	G	19.16	15.32	19.15	0.27	2.68	0.43
Chicago	C	13.53	9.46	9.01	0.5	3.60	0.32
Dublin	L	10.33	6.88	9.08	0.43	2.82	0.42
Jacksonville	L	25.96	15.71	13.66	0.26	2.46	0.45
Jerusalem	G	35.78	25.97	16.75	0.22	3.78	0.32
Kansas City	L	14.67	11.01	12.22	0.25	2.31	0.46
London	L	9.064	5.53	10.07	0.30	2.52	0.45
Madrid	G	20.49	14.87	16.53	0.63	3.12	0.38
Mexico_city	G	14.33	10.40	10.40	0.64	3.98	0.34
Miami	C	22.46	16.04	16.04	0.21	2.19	0.47
Milan	G	40.14	32.30	19.58	0.52	5.24	0.24
Montreal	C	10.64	7.70	7.33	0.65	2.75	0.41
Moscow	G	41.41	30.06	18.22	0.68	5.69	0.27
Naples	L	27.46	21.05	18.30	0.20	2.98	0.43
New Orleans	L	11.77	10.00	11.77	0.19	2.07	0.49
New York	C	10.28	6.07	9.34	0.5	2.53	0.44
Paris	G	18.88	13.71	11.42	0.57	3.82	0.34
Prague	L	4.82	3.61	12.04	0.32	5.06	0.39
Rio de Janeiro	G	8.82	6.40	8.54	0.78	3.05	0.37
Rome	G	34.62	25.13	14.87	0.49	7.88	0.25
San Francisco	C	14.14	8.24	11.78	0.35	2.09	0.49
Sao Paulo	G	7.22	5.24	9.53	0.49	2.21	0.47
Singapore	L	8.9750	6.28	17.94	0.53	2.19	0.48
Sofia	G	20.47	14.86	12.38	0.39	4.31	0.33
St. Petersburg	G	56.69	41.15	20.57	0.44	5.55	0.24
St. Petersburg USA	L	26.27	15.21	13.82	0.23	2.04	0.49
Stuttgart	L	23.13	14.96	13.60	0.55	3.78	0.34
Tel Aviv	L	49.29	37.18	17.29	0.33	7.85	0.18
Tokyo	G	12.80	9.29	9.29	0.29	3.43	0.34
Vancouver	C	12.01	10.44	10.44	0.30	2.07	0.49

Table 4.1: Geometric Data for cities

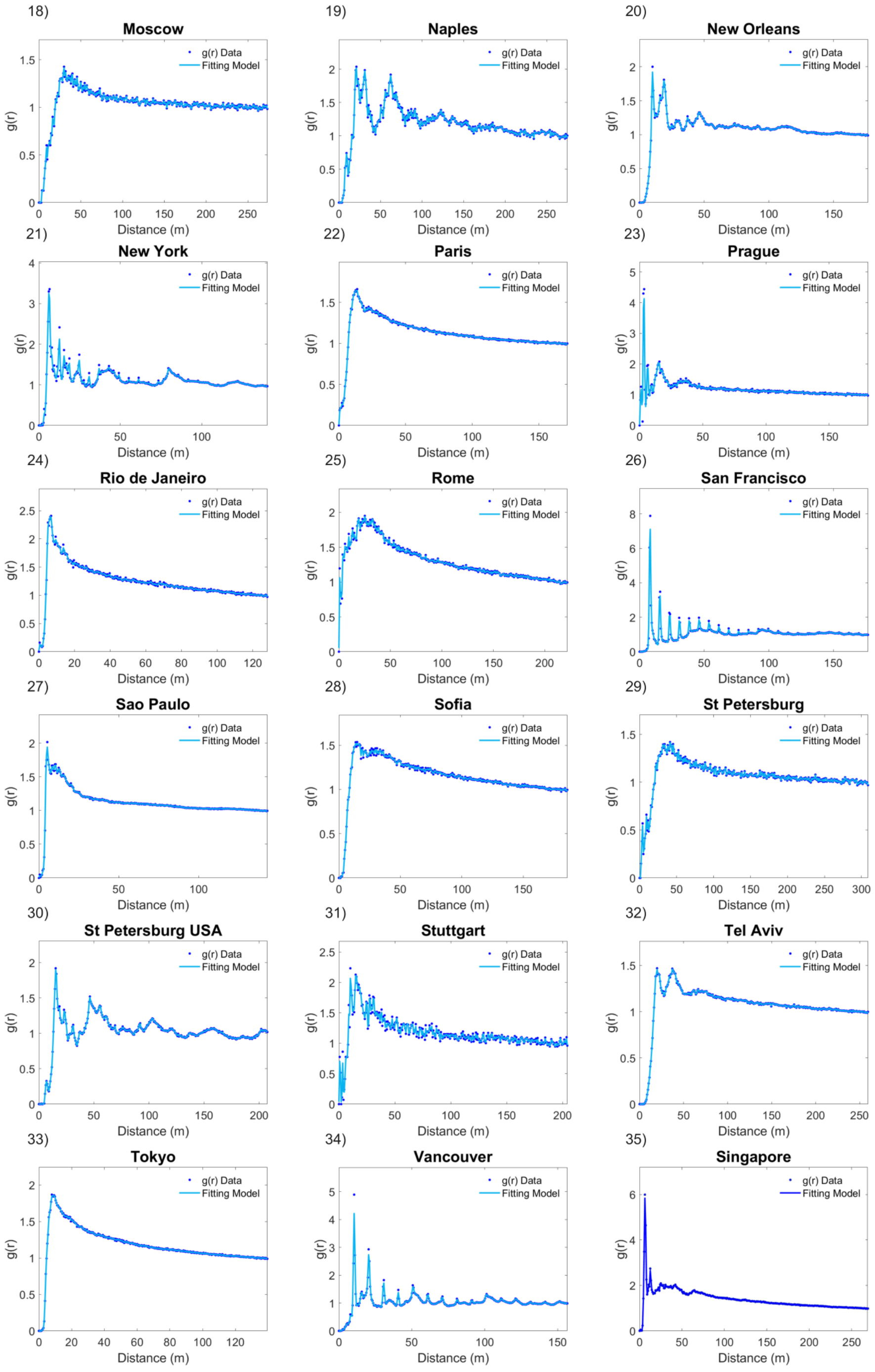

Figure 4-4: Radial distribution function for the calculated cities

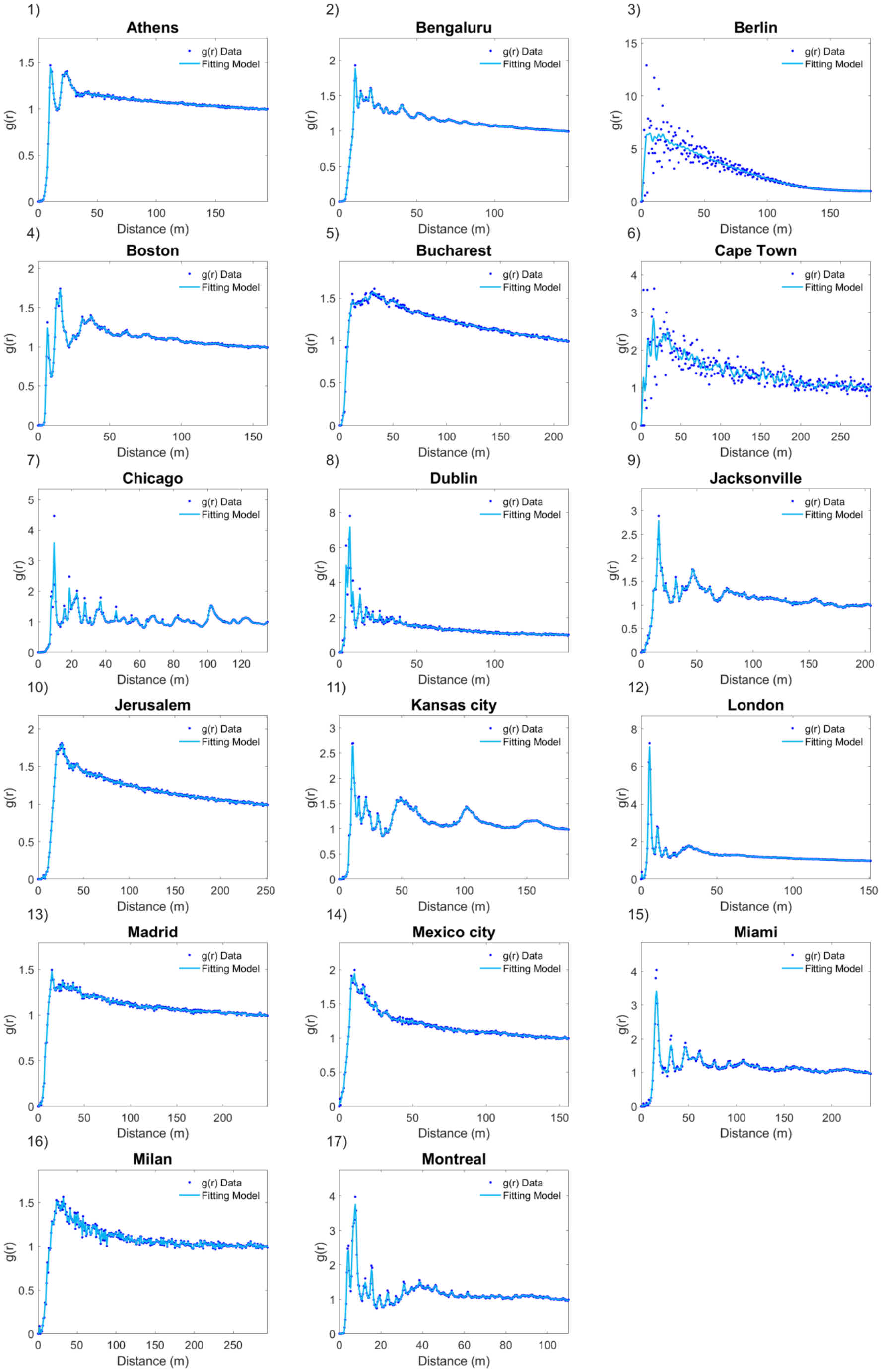

Figure 4-5: Radial distribution function for the calculated cities

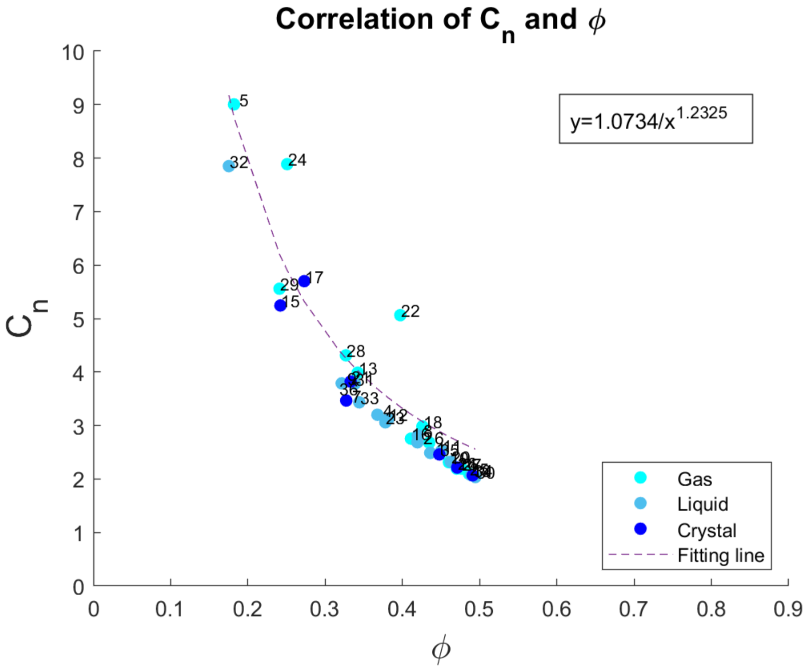

Figure 4-6: Correlation between the number of neighboring buildings Cn and the order parameter ϕ

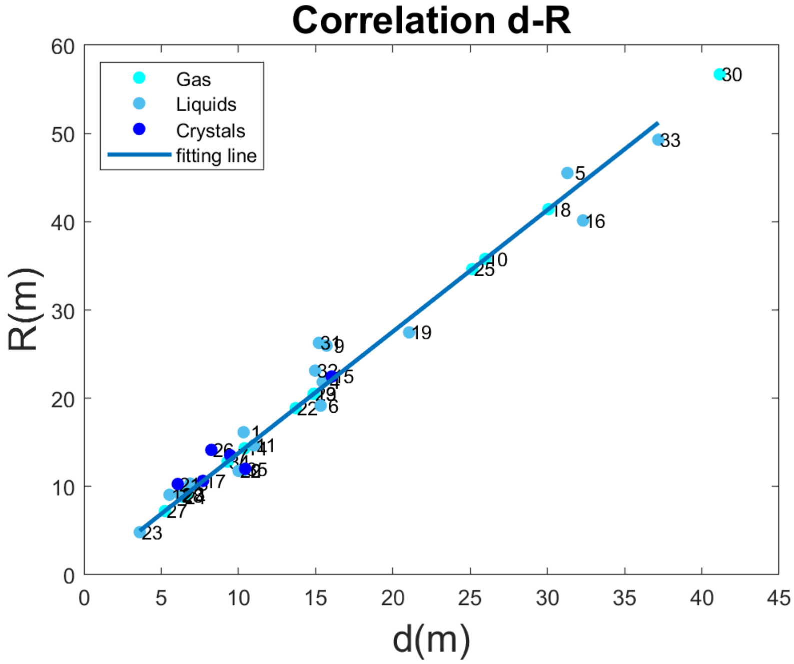

Figure 4-7: Correlation between Cluster Size and Distance between Buildings.

4.4 Correlation of city texture and UHI

Using the method to compute temperature and UHI presented in the previous chapter gives the opportunity to investigate if there is any correlation between surface UHI and city texture. It has been found that there is a high correlation between nighttime UHI and city texture by using measurement of meteorological station, however using satellite data to compute temperature gives continuous measurements for the entire city and urban area. The only restriction of this method is that there are only temperatures for a specific time, which is shown in the table below for each city. The fact of capturing images at different hours is problematic since the angle of the sun differs and the temperature data can't be easily compared. A further step could include a prediction model for this approach to estimate temperature on the same time. On the graph below the probability density function for the three structure categories, gas, liquid and crystal can be seen. The UHI is calculated by the data from the Satellite Data, which is done by taking the difference between the mean urban and rural temperatures. As the graph depicts, the distribution for gases varies the most, while it can be noticed that for crystal cities UHI is significantly confined within a smaller range. Using the definition of Shannon entropy, higher entropy means flatter histogram, which indicates sampled values to be less predictable, where for lower entropy, sample values are more predictable.

	City	time
1	Berlin	9:55
2	Jerusalem	8:10
3	Madrid	10:54
4	Mexico	16:58
5	Moscow	8:28
6	Paris	10:50
7	Rio de Janeiro	12:50
8	Rome	9:45
9	Sao Paulo	13:00
10	Sofia	9:10
11	St Petersburg	9:10
12	Tokyo	01:15

Table 4.2: Gases structured cities and the satellite capture time

	City	time
1	Athens	9:04
2	Bengaluru	5:10
3	Boston	15:26
4	Dublin	11:20
5	Jacksonville	16:00
6	Kansas city	17:00
7	London	10:50
8	Naples	15:55
9	New Orleans	16:30
10	Prague	9:55
11	Singapore	3:15
12	St. Petersburg USAâĂę	16:00
13	Stuttgart.mat	10:10
14	Tel Aviv	8:10

Table 4.3: Liquid structured cities and the satellite capture time

	City	time
1	Chicago	16:51
2	Miami	15:30
3	Montreal	15:37
4	New York	16:30
5	San Francisco	18:45
6	Vancouver	19:05

Table 4.4: Crystal structured cities and the satellite capture time

4.4.1 UHI results

At which distances g(r) reaches the first minimum, as it is the characteristic local cluster side, have to be compared. In previous calculations this characteristic cluster size was attributed to various values of urban heat islands across multiple American cities. It had to be checked if LST is highest for crystalline cities by correlating value âĂŹdâĂŹ from g(r) with average LST. As shown in the figures below, no correlation could be found between the average UHI and the average building distance. Instead of comparing the cluster size and the UHI as in previous work done by Sobstyl et al., the average building size has been used, since it can be found for all structured and unstructured cities. The cluster size can be calculated only for structured cities.

Possible explanations, why there is no correlation for daytime UHI and city texture

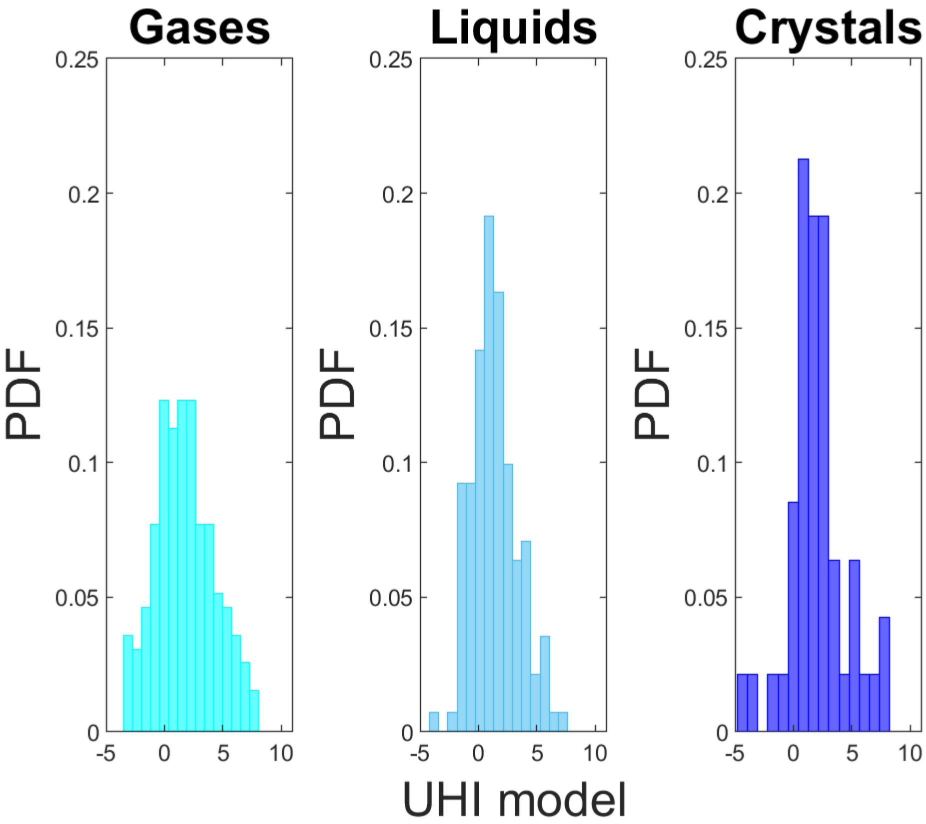

Figure 4-8: PDF-UHI for 35 cities categorized by their structure

is the differences in material in the cities the shapes of buildings and and also the time and date,[40]. Images for a specific time of the day for each city are available, but even by categorizing them by geographical location there is no ability to obtain any meaningful correlation. All the data for this correlation have temperature values between 22 and 27 degrees. These are taken in different times during the day. When the temperature is 27 degrees in the morning in Athens at noon it might be 35. The angle of the sun constitutes a major role in the temperature and in that way also the shadows.

As mentioned in the introduction during daytime the city is 'alive' and many more factors cause the UHI such as, the movement of the cars, the emission, the waste heat of air conditioning can. Further investigation on specifying the rural area could also provide more accurate results. Moreover, the mean values and the standard deviation of the created model are shown in the table below.

Structure	**mean UHI(Celsius)**	**standard deviation**
Gas	3.12	2.27
Liquid	2.29	1.58
Crystal	3.29	1.95

Table 4.5: Mean values and standard deviation calculated for the modeled UHI, by using the computed slope and rural temperature=25.5°C

The outcome that UHI changes by the change of temperature, has led to a second approach of comparing only UHI values that are in a closer interval for rural cities.

$mean(UHI) = Mean(LSTR) - Mean(LSTC)$ where $22 < LSTR < 27$

However neither could verify a correlation between UHI and city texture.

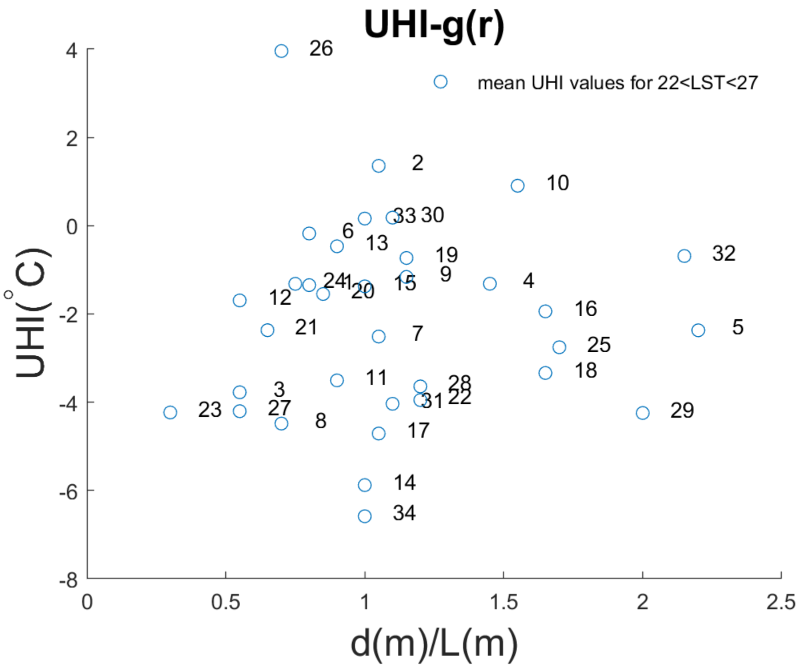

Figure 4-9: Correlation of UHI and city texture calculations

Using the method for predicting the temperature of cities, in [84], based on a prediction model which integrates the two characteristic sizes of the city, average building size and distance between buildings d. It can be assumed, that buildings of size L and mean height h=9.5m are separated by the distance d. A phenomenological factor $\gamma = 1$ for flat areas is taken. Using the equation below, the temperature difference can be predicted, the predicted UHI. However, as the model below depicts there is no correlation between the model UHI and the predicted one. The same

Structure	**mean UHI(Celsius)**	**standard deviation**
Gas	4.67	1.57
Liquid	4.85	1.62
Crystal	4.93	1.27

Table 4.6: Mean values and standard deviation calculated for the predicted UHI for rural temperature=25.5°C

parameters are being used to find if the values of modeled and predicted UHI are lying on the identity line. However the is no correlation found between these values, the prediction model is not working for the UHI, using satellite data. The probability density distribution of the three categories is shown in the graph below. Moreover, the mean values and the standard deviation of the predicted model are shown in the table below. Crystal cities have the highest predicted UHI that means that more structured cities seem to intensify this phenomenon while gas cities have the lowest. This outcome verifies the approach as described by Jobstyl,[84].

$$UHI_{predicted} = T_r[\gamma(1 + frac4LhL + d^{2^1}/4) - 1] \tag{4.7}$$

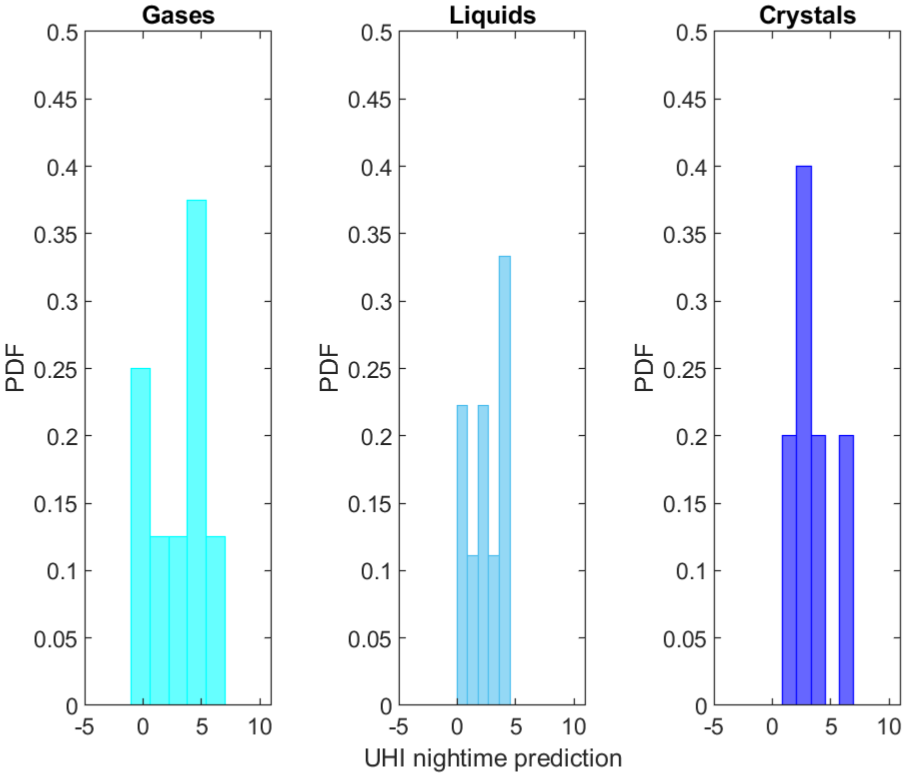

Figure 4-10: Probability density function of the predicted UHI for the different structures.

4.5 Summary

In this chapter a model where buildings resemble particles has been demonstrated, thus allowing to adopt tools from statistical physics to quantify city texture to only a few unique design parameters. A possible correlation between the UHI and the city texture has been examined and compared to the results of previous findings.

Chapter 5

Fluid Dynamic Simulation for Synthetic cities

5.1 Introduction

In this chapter the third research objective is the utilization of the radial distribution function g(r) for city modeling. In a further step, these models are being used to create synthetic cities and transform them into buildings and apply CFD simulations to quantify loads on the buildings. A brief introduction of the computational fluid dynamic methods is presented and why these are implemented to the solution. The methodology of the CFD analysis and the pre/post process will be explained step by step. As a final step, a validation of the method is required to confirm it's accuracy since there are many statistical factors that conclude to a good fluid solution.

5.2 City Modeling- Synthetic Cities

The target of this approach is to create representative samples of the cities to calculate wind loads. The fundamental method to create these samples- synthetic cities is based on Monte Carlo simulations, which are computational algorithms that rely on repeated random sampling to obtain numerical results. Their essential idea is using randomness to solve problems that might be deterministic in principle. Monte

Carlo methods are often used in generating draws from a probability distribution, such as the radial distribution function. In physics-related problems, Monte Carlo methods are useful for simulating systems with many coupled degrees of freedom, such as fluids, disordered materials, strongly coupled solids, and cellular structures). In principle, Monte Carlo methods can be used to solve any problem having a probabilistic interpretation,[98]. The present approach aims to create random city samples which respect the basic fundamentals of the city explained by the radial distribution function. The important fact is that the grand canonical Monte Carlo approach is successful in recreating statistical characterizes of disordered cities like Paris with 103367 buildings with a small model of about 900 buildings. Such created models will be used as inputs for computational fluid dynamics simulations to quantify wind failure risk metrics for cities from across the world.

5.2.1 Methodology

The focus of this investigation is creating disordered models of cities using the radial distribution function. This method has been applied in induced stiffness degradation of highly disordered porous materials and has been transferred into the city scale based on the assumption that buildings are porous. By disordered it is meant that the spatial distribution of the buildings is random and a priori does not follow a deterministic pattern. The goal is to identify, via discrete simulations, a relevant radial distribution function. This chapter focuses on the creation of synthetic cities. Understanding how the building-space configuration of a city can be set in order to have a representing sample. Two basic approaches to create the synthetic cities can be applied. A previous approach to model synthetic cities was based on a restricted randomized approach, where it could be started with a perfectly ordered grid configuration of buildings. The randomly shift of particles inside those grid cells until the g(r) of the model would match to that g(r) of the city. Random moves within a unit cell. Pores/buildings of the ordered systems are moved to random positions at a distance $0<d<l/2\text{-}R$ contained within their original unit cell. The number of buildings is kept fixed and the density decreases as the size of the building increases. The approach is based on a

two dimensional building distribution. Starting with a perfectly ordered system and disorder it, by confining buildings in their unit cell.

$$Lx = Ly = L = \sqrt{N}l. \tag{5.1}$$

The density of g(r) is tuned by computing the number of buildings and the size of the plate. In the periodic porosity arrangement of porous material systems the porosity is tuned by varying the size R of the pores and their number N.

$$\rho_{gr} = \frac{N}{L^2} \tag{5.2}$$

5.2.2 Creation of Synthetic cities

This approach works well for cities with multiple peaks in g(r), although for highly disordered cities that merely have a single peak, it results in high error values. To address the issue, it will be shifted to a fully random approach where there is no restriction, where a particle or a building should be placed for as long as it is within the box boundaries to respect the given-defined input density criterion. The distribution of particles is random and at first the initial configuration of g(r) is not similar to an actual city. To change that, the Monte Carlo (MC) approach is being used. The insertion in this approach is the number N of pores and fixed pore radius. In these MC-based generations, the density- porosity is defined by the number of buildings, eventually corrected for the level of overlapping buildings. The defined conversion criterion in this MC is whether or not the model resembles a city, to achieve the calculation of its radial distribution function. The flowchart of this approach is shown below.

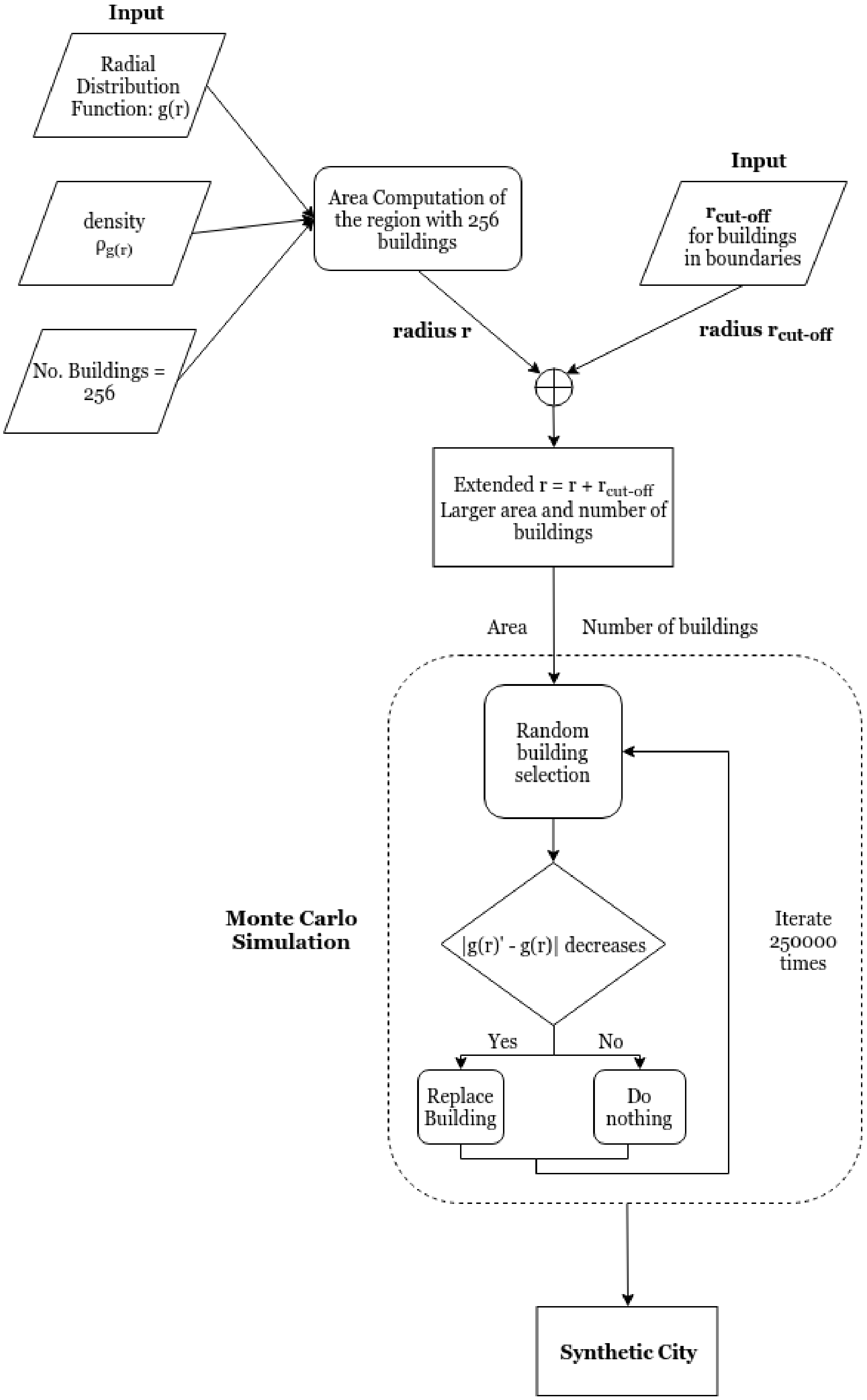

Figure 5-1: Creation of Synthetic cities workflow

More specifically, the input for creating the synthetic cities are g(r), density of g(r) that accounts as the number of buildings divided by the area of the city and the number of buildings for our synthetic city. A first estimation for the buildings number was 100 however for calculating g(r) there must be a large number of points/buildings. The approximation is generally poor if only a few buildings are randomly placed in the whole square,[98]. On average, the approximation improves as more points are placed although the computational cost restriction has led to a number of buildings of 256. These buildings are being used to define a domain of possible inputs. For the number of buildings in the rectangle, the plan is to calculate their drag coefficient in the CFD simulation. Adding the r cut-off distance gives a larger region in which the number of buildings has to be quantified. Using the area of the previous inside region and by knowing the density criterion and the extended area, the number of buildings is computed. That results to two different theoretical squares. The inner one for calculating the g(r) ,as explained in the revised g(r) definition , and the outer which is being used to avoid the boundaries effect, the use of these buildings by computing the g(r),but without computing it for these buildings. After that, the use of the Monte Carlo Simulation will generate inputs randomly over the domain, that means a random selection of a building and performing a deterministic computation on the inputs, replace it with a randomly position building only if g(r) of the new configuration matches more closely the g(r) of the city. After 50,000 iterations the results will be aggregated, by achieving a distribution that resembles well the actual g(r) for the city. While the small error still exists, it can be further reduced with more iterations. The errors are shown in the table 5-1. There are small errors for all the cities, the same error metrics have been used as in the validation of OSM data. It has been focused on less iterations but the error of g(r) was significant. The results for the five cities are shown below. The g(r) for the modeled cities and the original are shown in the figures. It can be depicted, that there is a small error between these functions; however this could be reduced more by increasing the iterations of buildings assignments. The values of cn and ϕ are shown in the table below.

The model of Athens and the original buildings on the city are shown in the graphs below. In the first figure it can be distinguished between the two boxes. The

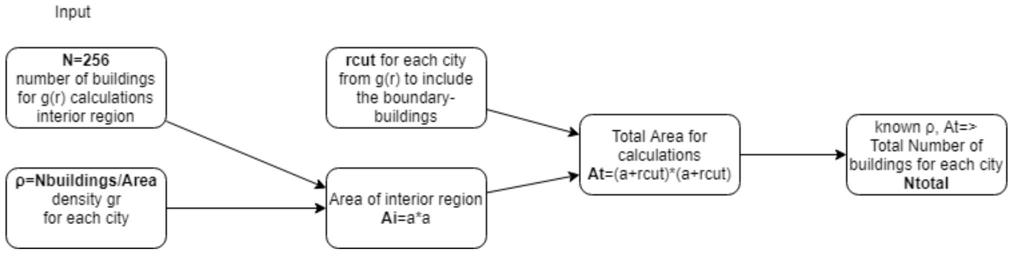

Figure 5-2: Computation approach of the Total number of buildings in the interior area and the total area

City	**rcut**	**density**	**N of building from map data**	**Ntotal for synthetic city**
Athens	193	0.0023	66164	1225
Miami	240	0.000453	24724	676
Paris	171	0.0017	103367	900
Vancouver	156	0.0018	133817	841

Table 5.1: Numerical data for created synthetic cities, different rcut and gr density concludes to different total number of buildings in the synthetic cities

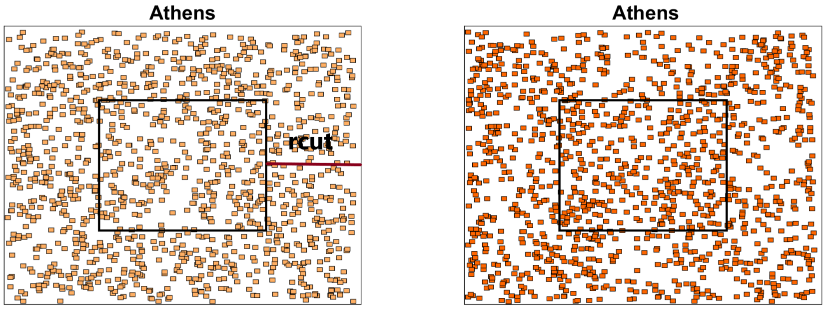

(a) Initial configuration Athens (b) Final configuration Athens

Figure 5-3: Synthetic city of Athens

inner box presents all the data, for which g(r) has been calculated, and the wind simulations, where the outer box presents all the buildings which are located at the rcut distance. As already mentioned, these points are being used to calculate the g(r) only as neighboring buildings. On the Figure 5-3 the city of Athens is illustrated. Even though these two images do not look similar as shown from the g(r) Figure 5-4, the model resembles the city of Athens with small g(r) errors. The number of neighboring buildings and the distances between them are similar.

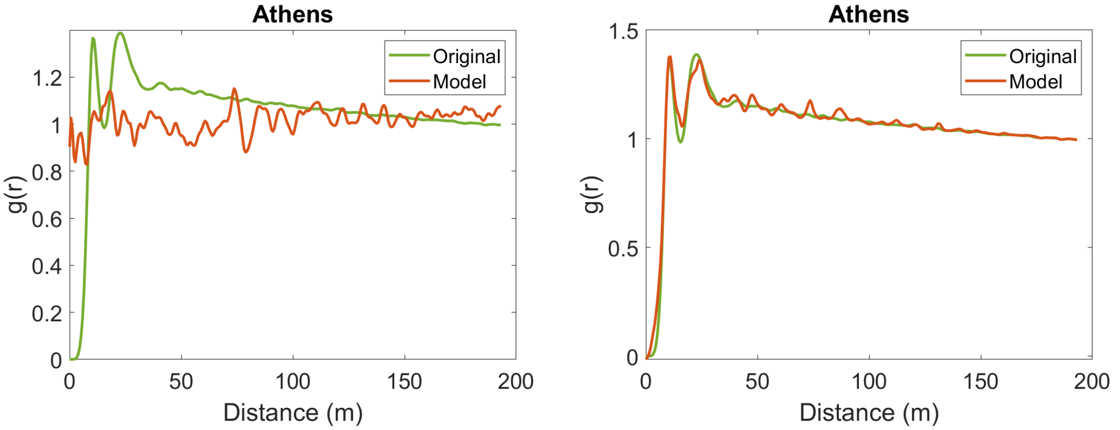

(a) Initial step of Monte Carlo simulation (b) Final step of Monte Carlo simulation

Figure 5-4: Radial distribution function for modeled and original city

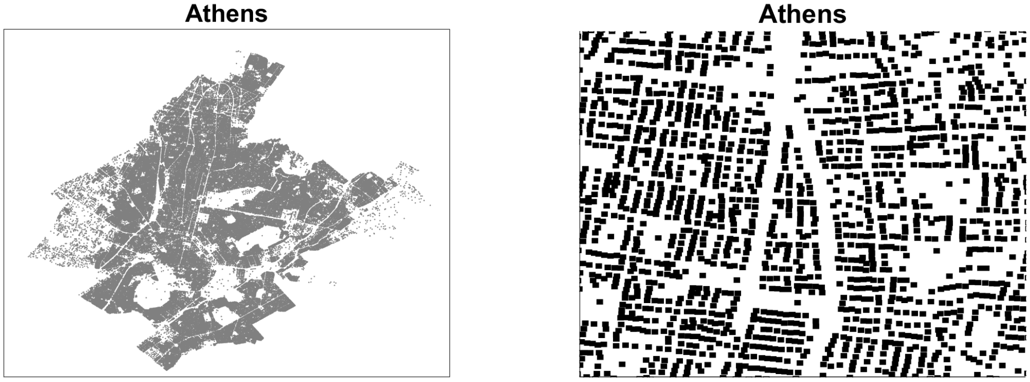

(a) Building distribution for the city of Athens (b) zoomed city of Athens

Figure 5-5: Original distribution of buildings with average building size 11m

Comments to the errors-Validation

It can be observed that among the four cities, the various error metrics MAE, RMSE, the difference Mean value and the difference in the standard deviation, have small magnitude in comparison to the actual values of the two examined curves, since the error values have the same units as the curves. That indicates that a high accuracy using 250000 iterations can be achieved. Conclude the above the computed rdf values for both approaches are visible. Moreover the values of cn and ϕ of the synthetic cities are shown below. The correlation graph between ϕ and cn includes the values calculated from the synthetic cities. However more iterations could have provided less

City	MAE	Mean Diff	RMSE	Std Diff
Athens	0.0200	0.0078	0.0518	0.0092
Miami	0.0327	0.0074	0.0856	0.0266
Paris	0.0270	0.0057	0.0636	0.0037
Vancouver	0.0438	0.0034	0.1356	0.0843

city	**Athens**	**Miami**	**Paris**	**Vancouver**
cn	2.73	2.43	3.48	2.32
phi	0.41	0.44	0.35	0.45

error a balance between computational cost and accuracy concluded to this number.

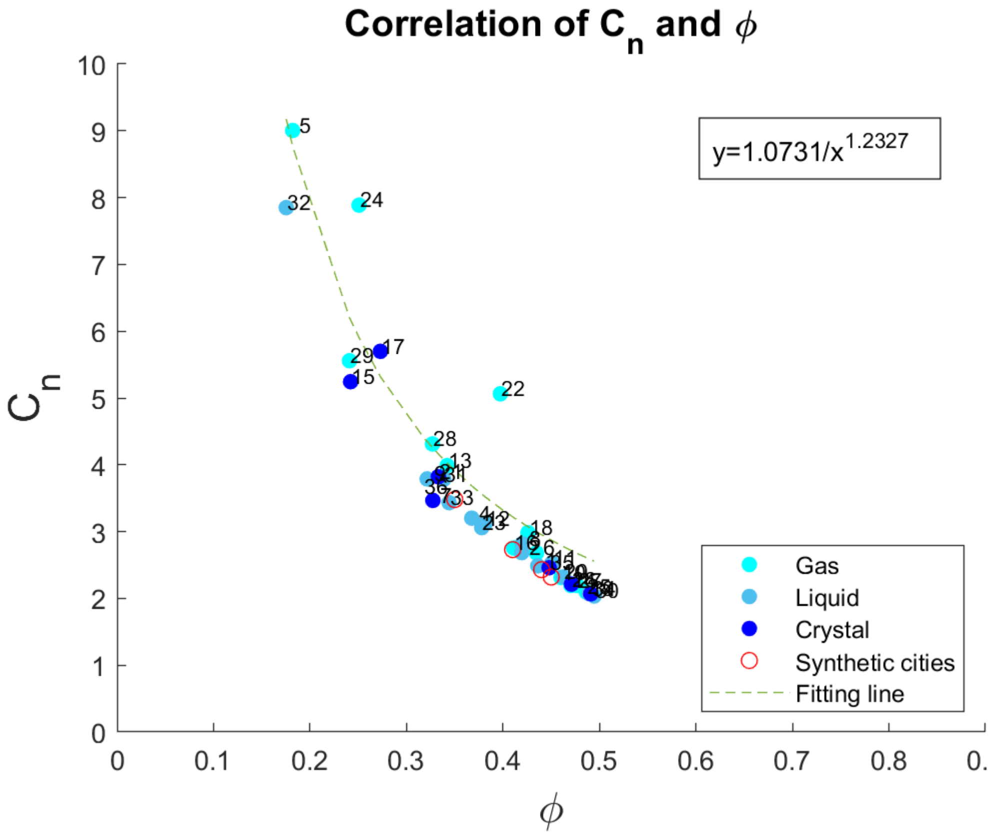

Figure 5-6: Correlation of ϕ and cn for original cities and synthetic

5.3 Theory

Understanding the relationship between turbulent flow characteristics and surface geometry is very important for mitigating urban atmospheric problems such as hurricane disasters and the heat island effect. The mean flow and turbulent statistics have been extensively studied by laboratory experiments, field campaigns, and numerical simulations. Urban geometry, even with simple obstacle arrays, has spatial heterogeneity, which makes it difficult to obtain a precise representative picture of the flow characteristics. Chen [18] made comprehensive laboratory experiments for flow over cube arrays and carefully investigated the spatial averaged turbulent flow statistics and the spatial variation. This study investigates urban canopy layers (UCLs) under neutral atmospheric condition with the same building area density and frontal area density but various urban forms. Turbulent air-flows are first predicted by CFD simulations with standard $k-\epsilon$ model evaluated by wind tunnel data. In a typical urban area where buildings are built in a cluster with random spacing, the distribution of the wind pressure on a building is influenced by interference effects from neighboring buildings, which could ultimately affect the wind flow across the building. Large-eddy simulations (LESs) were conducted for five cities of staggered random arrays with various packing densities λ_p. Large-eddy simulations have been performed for fully developed turbulent flow, however in this study we are interested in the correlation between the distribution of buildings, which resemble a city, as provided by the g(r) and the drag coefficient,[18].

In this study the confrontation with a turbulent flow in our modeled city is necessary. Turbulence is flow characterized by eddies, and apparent randomness. The presence of eddies or recirculation alone does not necessarily indicate turbulent flowâĂŤthese phenomena may be present in laminar flow as well. Mathematically, turbulent flow is represented via a Reynolds decomposition, in which the flow is broken down into the sum of an average component and a perturbation component. It is believed that turbulent flows can be described well through the use of the Navier Stokes equations. Direct numerical simulation (DNS), based on the NavierâĂŞStokes equations, makes it possible to simulate turbulent flows at moderate Reynolds numbers. Restrictions depend on the power of the computer used and the efficiency of the solution algorithm. The results of DNS have been found to agree well with experimental data for some flows.Most flows of interest have Reynolds numbers much too high for DNS to be a viable option, given the state of computational power for the next few decades, [97]. Different approaches for calculating the Navier Stokes equations have been established to solve real-life flow problems; the optimal model selection is problem dependent. A basic segregation of the flow is if itâĂŹs either steady or unsteady. A flow that is not a function of time is called steady flow. Steady-state flow refers to the condition where the fluid properties at a point in the system do not change over time. Time dependent flow is known as unsteady, also called transient. Whether a particular flow is steady or unsteady can depend on the chosen frame of reference. In a frame of reference that is stationary with respect to a background flow, the flow is unsteady. Turbulent flows are unsteady by definition. A turbulent flow can, however, be statistically stationary. This means that all statistical properties are constant in time. Often, the mean field is the object of interest, and this is constant too in a statistically stationary flow. Steady flows are often more tractable than otherwise similar unsteady flows. The governing equations of a steady problem have one dimension fewer (time) than the governing equations of the same problem without taking advantage of the steadiness of the flow field, [97]. The two main methods to solve our flow are unsteady modeling with scale-resolving simulations (SRS), such as Large Eddy Simulations and Steady State Turbulence Modeling, such as Reynolds Averaged Navier Stokes Simulations (RANS) e.g $k - \epsilon$.

5.4 Characteristics of Turbulent Flows

The flow is unsteady, irregular and has an aperiodic motion in which transported quantities such as mass, momentum, scalar species, fluctuate in time and space. These fluctuations are responsible for enhanced mixing of transported quantities Instantaneous fluctuations are random, unpredictable and irregular both in space and time. Statistical averaging of fluctuations results in accountable, turbulence related transport mechanisms. Turbulence flow contains a wide range of eddy sizes (scales), where large eddies 'carry' small eddies and the behavior of large eddies is different in each flow because they are sensitive to upstream history on the other hand the behavior of small eddies is more universal in nature, [97].

5.5 Reynolds Number

Whether a flow is laminar or turbulent depends of the relative importance of fluid friction (viscosity) and flow inertia. The ratio of inertial to viscous forces is the Reynolds number. Given the characteristic velocity scale, U, and length scale, L, for a system, the Reynolds number is Re = UL/v, where v is the kinematic viscosity of the fluid, [68]. Turbulent flow occur at large Reynolds numbers.

5.6 Smallest Scales of Turbulence

These methods are being used to eliminate the need to resolve small eddies and solve the turbulence flow. The implication of scales appears to be a major problem in solving our cfd problems. A mesh would have to be fine enough to resolve smallest eddies and large enough to capture mean flow features. In order to solve the problem the following two approaches have been used - each one of them to derive different results.

5.7 The $k - \epsilon$ method

The K-epsilon model is one of the most common turbulence models, although it just doesn't perform well in cases of large adverse pressure gradients [52]. It is a two equation model that means it includes two extra transport equations to represent the turbulent properties of the flow. This allows a two equation model to account for history effects like convection and diffusion of turbulent energy. The first transported variable is turbulent kinetic energy, k. The second transported variable in this case is the turbulent dissipation,ϵ. It is the variable that determines the scale of the turbulence, whereas the first variable k, determines the energy in the turbulence. The original impetus for the $k - \epsilon$ model was to improve the mixing-length model, as well as to find an alternative to algebraically prescribing turbulent length scales in moderate to high complexity flows. Accuracy has been shown experimentally to be reduced for flows containing large adverse pressure gradients however this method is applied in our methodology to create the input velocity, which will be explained more thoroughly in the Methodology section. The parameters as described below are being used in our simulation.

5.8 RNG k-epsilon method

The Re-Normalisation Group (RNG) $k - \epsilon$ model has a similar form to $k - epsilon$ but includes refinements. First the RNG model has an additional term in its epsilon equation that significantly improves the accuracy for rapidly strained flows. To enhance accuracy, the effect of swirl on turbulence is included in the RNG model. The turbulence kinetic energy, k and its rate of dissipation,ϵ, are obtained from the following transport equations:

$$\frac{\partial(\rho k)}{\partial t} + \frac{\partial(\rho k u_i)}{\partial x_i} = \frac{\partial(\alpha_k \mu_{eff} \frac{\partial k}{\partial} x_j}{\partial x_j} + G_k - \rho\epsilon - \Upsilon_M + S_k \tag{5.3}$$

$$\frac{\partial(\rho\epsilon)}{\partial t} + \frac{\partial(\rho\rho u_i)}{\partial x_i} = \frac{\partial(\alpha_k \mu_{eff} \frac{\partial k}{x_j}}{\partial x_j} + C_{1\epsilon}\frac{\epsilon}{k}G_k - C_{2\epsilon}\rho\frac{\epsilon^2}{k} - R_\epsilon + S_\epsilon \tag{5.4}$$

$$\mu_t = \rho C_\mu \frac{k^2}{\epsilon} \tag{5.5}$$

$$G_k = -\rho \overline{u_i' u_j'} \frac{\partial u_j}{\partial x_i} \tag{5.6}$$

$$\Upsilon_M = 2\rho\epsilon M_t^2 \tag{5.7}$$

$$M_t = \sqrt{\frac{k}{\alpha^2}} \tag{5.8}$$

$$\alpha = \sqrt{\gamma R T} \tag{5.9}$$

where G_k represents the generation of turbulence kinetic energy due to mean velocity gradients, Υ_M represents the contribution of the fluctuating dilatation in the compressible turbulence to the overall dissipation rate and the quantities α_k and α_ϵ are the inverse effective Prandtl numbers for k and epsilon, respectively. S_k and S_ϵ are user defined source terms and M_t is the turbulent Mach number.

$C_\mu = 0.0845$, $C1_\epsilon = 1.42$, $C2_\epsilon = 1.68$, inlet velocity for k-epsilon: $u = 55\frac{m}{s}$ and the time step= 0.1

5.9 Large Eddie Simulation (LES) Method

Large eddy simulation (LES) is a popular technique for simulating turbulent flows,[80],[76],[66], [48].An implication of Kolmogorov's (1941) theory of self-similarity is that the large eddies of the flow are dependent on the geometry while the smaller scales more universal. This feature allows one to explicitly solve for the large eddies in a calculation and implicitly account for the small eddies by using a subgrid-scale model (SGS model). Mathematically, one may think of separating the velocity field into a resolved and sub-grid part. The resolved part of the field represent the "large" eddies, while the subgrid part of the velocity represent the "small scales" whose effect on the resolved field is included through the subgrid-scale model, [28]. The governing equations employed for LES are obtained by filtering the time-dependent Navier-Stokes equations in either Fourier (wave-number) space or configuration (physical) space. The filtering process effectively filters out the eddies whose scales are smaller than the filter width or grid spacing used in the computations. The resulting equations thus govern the dynamics of large eddies, [25]. A filtered variable (denoted by an overbar) is defined by

$$\bar{\phi}(x) = \int_D \phi(x')G(x,x')dx'$$

, where D is the fluid domain and G is the filter function that determines the scale of the resolved eddies. More specifically in Ansys the finite volume discretization itselfs implicitly provides the filtering operation.

$$\bar{\phi}(x) = \int_V \phi(x')dx'$$

, where V is the volume of a computational cell and the filter function $G(x, x)$ implied here is then

$$G(x, x') = \begin{cases} \frac{1}{V}, & x' \in \\ 0 & x' otherwise \end{cases}$$

The filtering process of each method provides us a variation on the Naviers Stokes simulation.

$$\frac{\partial \rho}{\partial t} + \frac{\partial(\rho \bar{u_i})}{\partial x_i} = 0 \tag{5.10}$$

The filtering process of each method provides us a variation on the Naviers Stokes simulation.

$$\frac{\partial(\rho \bar{u}_i)}{\partial t} + \frac{\partial(\rho \bar{u}_i \bar{u}_j)}{\partial x_j} = \frac{\partial \sigma_{ij}}{\partial x_j} - \frac{\partial \bar{p}}{\partial x_i} - \frac{\partial \tau_{ij}}{\partial x_j} \tag{5.11}$$

It has been assumed that the filtering operation and the differentiation operation commute, which is not generally the case. It is thought that the errors associated with this assumption are usually small, though filters that commute with differentiation have been developed. The extra term $\frac{\partial \tau_{ij}}{\partial x_j}$ arises from the non linear advection terms, due to the fact that $\overline{u_j \frac{\partial u_i}{\partial x_j}} \neq \bar{u}_j \frac{\partial \bar{u}_i}{\partial x_j}$ and σ_{ij} is the stress tensor due to molecular viscosity defined by $\sigma_{ij} = [\mu(\frac{\partial \bar{u}_i}{\partial x_j} + \frac{\partial \bar{u}_j}{\partial x_i})] - \frac{2}{3}\mu \frac{\partial \bar{u}_i}{\partial x_i} \delta_{ij}$ and $\tau_{ij} = \rho \overline{u_i u_j} - \rho \bar{u}_i \bar{u}_j$

Similar equations can be derived for the subgrid- scale field. The subgrid-scale stresses resulting from the filtering operation are unknown and require modeling. These equations are shown in the Appendix.

LES method has the potential for improved accuracy when the resolution of the largest eddies are important or when unsteady data is needed. The disadvantages here are mainly that it is computationally expensive, a higher grid resolution is required and also an unsteady simulation with small time steps generates long run times and large volumes of data. As explained in the methodology used, there is a very simple geometry and that gives the opportunity to afford an LES simulation.

5.10 Methodology

Five different sets of urban configuration, one for each city are defined by considering rectangular buildings with a plan area. The distribution of the buildings is based on the created models as described in the previous section. The building models are used and the points converted into buildings. A density($\rho = 0.25$) for the city is specified and the buildings are created. The building size is selected by respecting the density and the number of buildings. After creating the initial configuration as shown below, a further condition is added. Buildings with a distance less than one meter are being merged. This step has been considered to be necessary because a one meter gap does not really represent a street in an actual city but mainly since the created mesh would not create enough nodes to calculate sufficient results in such a small canopy. The created city is shown in the figure below. During the Ansys simulation one more filtering method for the buildings is applied as described below. The variable of height selected is : 10 m.

An important factor to mention is the application of a CFD for the entire city. Based on a flow adjustment region, which is necessary to analyze correctly the drag force, there is an interest in getting the results for the interior region as shown in the figure below. The same buildings for which g(r) has been calculated. The flowchart of this approach is shown in the next figure. On this approach it has been used the same height and density for all the cities, however the distance between buildings and their distribution is changing.

It has been found that the flow reaches equilibrium more rapidly when a more turbulent approaching flow is used. Analytical studies introduced the canopy-drag

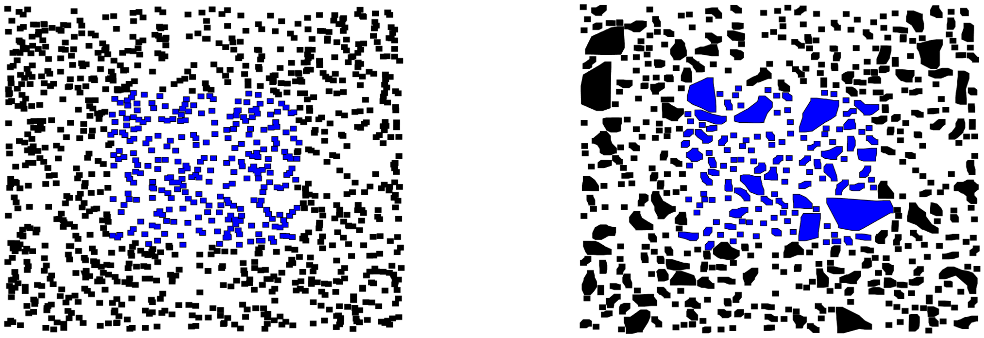

(a) Initial step of building configuration for the city of Athens

(b) Final step of building configuration for the city of Athens

Figure 5-7: Non-Dissolved and Dissolved buildings

length scale (Lc) as a fundamental dynamical length scale of urban canopies, [23] used Lc to estimate the distance for flow adjustment as a flow enters an urban canopy, [55]. The first buildings are being used for a flow adjustment region and the last ones as a flow exit region. The approaching wind is first strongly displaced and blocked by the first building, thus the drag force induced by the first building is extremely large.The drag force of the second building is small because it is strongly sheltered by the first building. Then after the flow adjustment process, the drag force reaches a flow balance in the fully-developed region,[19].

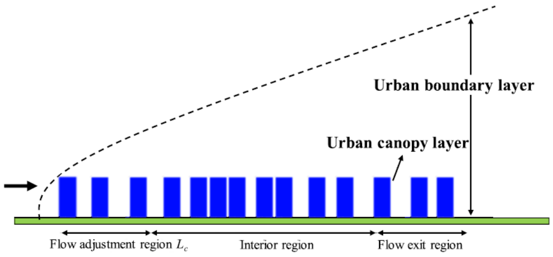

Figure 5-8: Regions of our city model

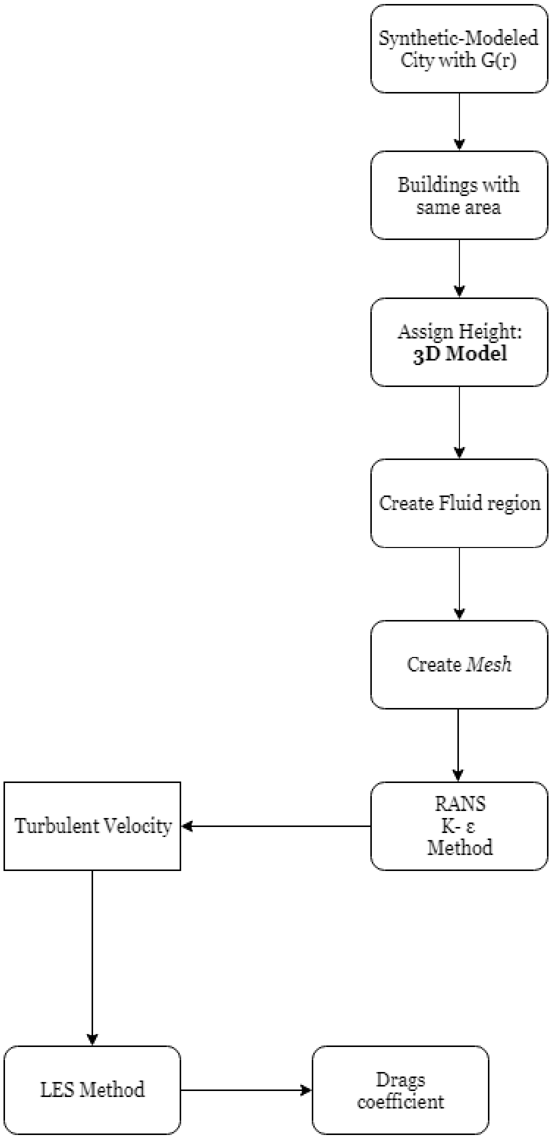

Figure 5-9: Flow chart

5.10.1 Computational grid/mesh

Grid refinement can be a critical component of achieving a grid-independent solution, which is a universally accepted CFD best practice. During the pre-processing stage, there is a need to know a suitable size for the first layer of grid cells. The initial size has a reference the building and the quality target is selected to be 0.95. The additional criterion is set to have no more than 7 million nodes due to high computational cost and time constraint. The mesh quality plays a significant role in the accuracy and stability of the numerical computation. Regardless of the type of mesh used in a domain, checking the quality of the mesh is essential. The more complex geometry is, causes complications to the mesh generation. The presented city models contain many buildings, that means many geometric obstacles which have different size and geometry and more over their distribution is the fluid region is randomly set. This is being done as explained in previous steps to find a model that represents the geometrical- spatial distribution of the buildings in the city as defined by the radial distribution function. The first mesh occurred to have lots of errors approximately 500 which were reduced to 10 ped model. To achieve this mesh repairing the default virtual topology of ansys was used, which removes edges and merges geometry. More specifically when two buildings are very close to each other having a 10 cm distance, they are merged. To repair the mesh also a non-automatically process needed to be applied due to high complexity of the geometry, to adjust different size effects. This has been a trial and error method since there is no correct answer on how to create a correct mesh. Basic requirements are the Mesh Element Distribution since poor resolution in critical regions can dramatically affect results. The Cell Quality which shows the geometry of the cells. The effect of resolution, smoothness, and cell shape on the accuracy and stability of the solution process is dependent on the flow field being simulated. Since the locations of strong flow gradients generally cannot be determined a priori, you should strive to achieve a high-quality mesh over the entire flow domain,[26].

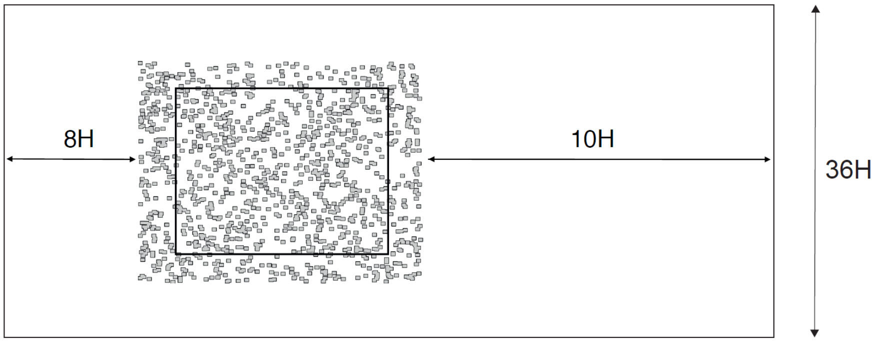

Figure 5-10: Fluent region

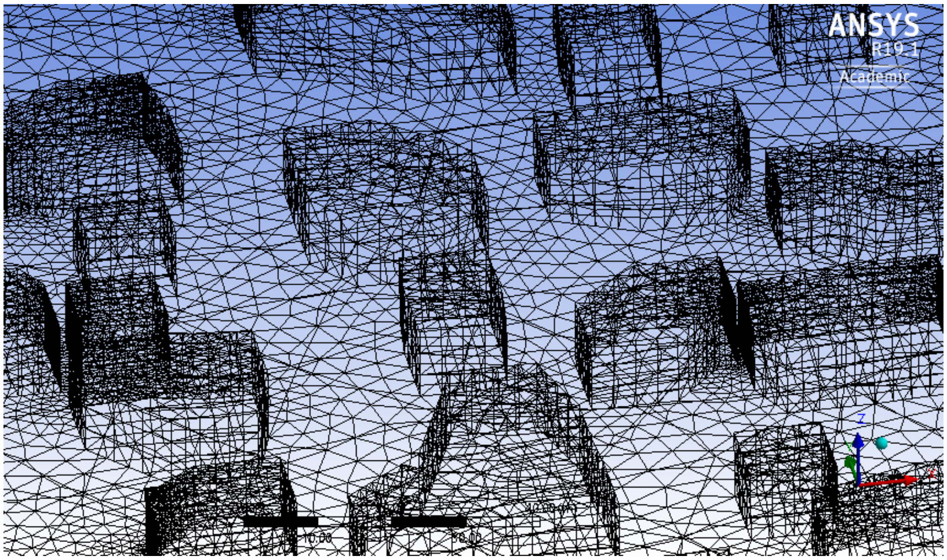

Figure 5-11: Mesh for the synthetic city

5.10.2 Validation

The two models for solving a CFD simulation have been presented in the previous section; however the application of these models and the case configuration will be presented as part of the methodology,[54].

Both models are being validated by comparing them with more simplified geometries. The validation is based on the wind tunnel experiment by Brown [17] and the results were sufficient for both $k - \epsilon$ approach and the LES. The quality and accuracy of the grid selections have been the same as for the CFD simulation of our city models.

5.10.3 Case Configuration

RANS simulation

The following approach is based on the study of Adjustment of Turbulent Boundary-Layer Flow to Idealized Urban Surfaces: A Large-Eddy Simulation Study. [Brown 2017/05]

In this study the study of RANS has been performed, a standard k-ϵ model to create representative turbulent inlet flow and include a periodic boundary condition

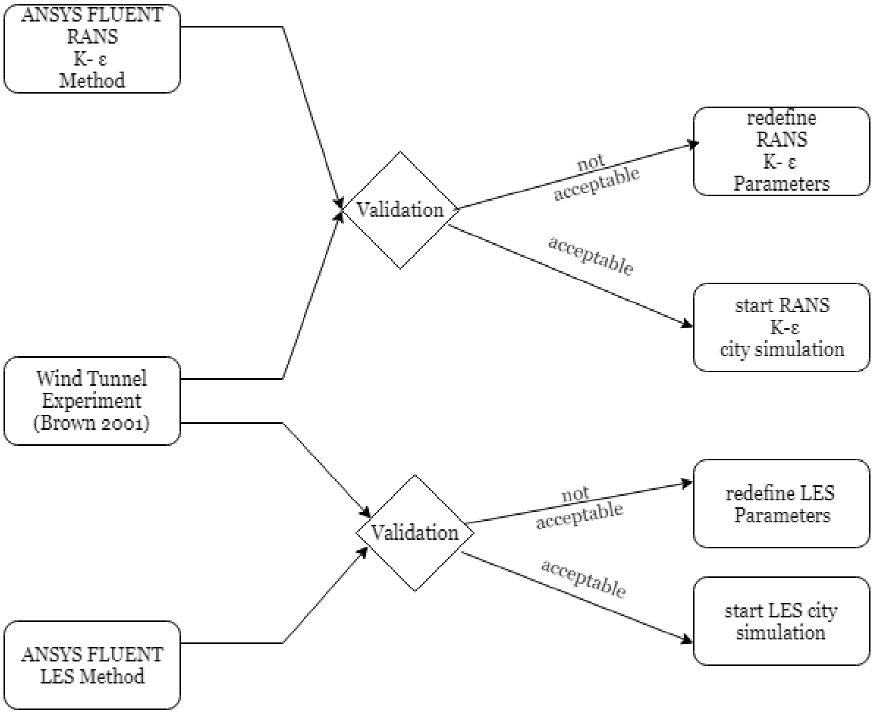

Figure 5-12: Flow chart for Validation

in the lateral direction. A precursor simulation technique was adopted, and involved running a prior simulation of the turbulent boundary-layer flow. The input velocity of this simulation was set to 55 m/s which resembles a hurricane wind velocity of category 3.The instantaneous velocity fields obtained from this simulation are saved and later used as inflows to the simulations of flow past cube arrays.

The boundary conditions for this k-epsilon simulation as described by[18].

A stress free wall for top boundary condition was considered. At the block surfaces, the surface shear stress was computed using a method similar to that for the bottom surface. This required the calculation of the instantaneous (filtered) surface she Moreover, smoothing of the velocity field inside the blocks before the velocity derivative calculations, was used to diminish the Gibbs phenomenon that occurs near sharp boundaries. The problem has been calculated with the default values of Ansys since the validation confirmed small errors by using this approach.

LES Simulation

The final computational step is to perform a Large eddy simulation (LES) as defined by the Ansys software. This model is better in predicting turbulence but require much longer computational time than the Reynolds-Averaged Navier Stokes (RANS) approaches [21]. The turbulence velocity results of the previous k-epsilon simulation and is the main input variable for the LES simulation. The desired output of this simulation is the drag force in order to calculate the drag coefficient on the buildings, that concludes to use a pressure based solver with a transient time,[23],[77]. The velocity field is obtained from the momentum and continuity equations. In the pressure-based approach, the pressure field is extracted by solving a pressure or pressure correction equation which is obtained by manipulating continuity and momentum equations. The pressure equation is derived from the continuity and the momentum equations in such a way that the velocity field, corrected by the pressure, satisfies the continuity. Since the governing equations are nonlinear and coupled to one another, the solution process involves iterations wherein the entire set of governing equations is solved repeatedly until the solution converges. In the proposed solution the max iterations per time step is adjusted to minimum value that allows convergence (about 30-35). The number of time steps is about 150-200, to achieve convergence.

5.11 Discussion for CFD computaions of cities

The first output of the CFD simulation is the velocity of the four different cities. The velocity on the ground for z=0 is also zero, respecting the no slip boundary condition. As the height increases, the velocity increases as well since the influence of the obstacles reduces. The graphs below show us the velocity in the $h/2 = 5m$ of the buildings and $h = 10m$ on the top of the buildings. In both cases the velocity increases the most, when the canopy is small. That phenomenon is based on the conversation of mass and the Bernoulli equation. When the surface A decreases, which happens in small canopies the velocity increases. Taking into account also the Bernoulli equation while the velocity increases the the pressure must decrease. The difference in pressure $DP = P_2 - P_1$ of the inside and outside area of the buildings constitutes the drag force of the building. However, on this present approach by having multiple obstacles/buildings the flow of the previous canopies effect the velocity and pressure,[12],[75]. This is why this simplified approach can be used just for a very roughly understanding of the single canopy effect. The different structures of the city conclude to a different velocity magnitude, which also effects the drag forces on the buildings.

The aim of this approach is to establish a statistically valid formula that would quantify the correlation between urban morphology and drag coefficient. The drag coefficient is a number that is being used to model all of the complex dependencies of shape and flow conditions on solid drag. This equation is simply a rearrangement of the drag equation where we solve for the drag coefficient in terms of the other variables. The drag coefficient Cd is equal to the pressure difference divided by the quantity: density rho times half the velocity V squared times the reference area A. The ansys software gives us the opportunity to calculate the pressure values on each building. By taking the average drag coefficient of each city the values diverse. As shown also in the graphs below, the crystal cities such as Vancouver and Miami intensify the drag coefficient, while gases reduces it. A typical drag coefficient value for a single cube in fluids with Reynolds 10^4 is 1.05. The distribution of buildings

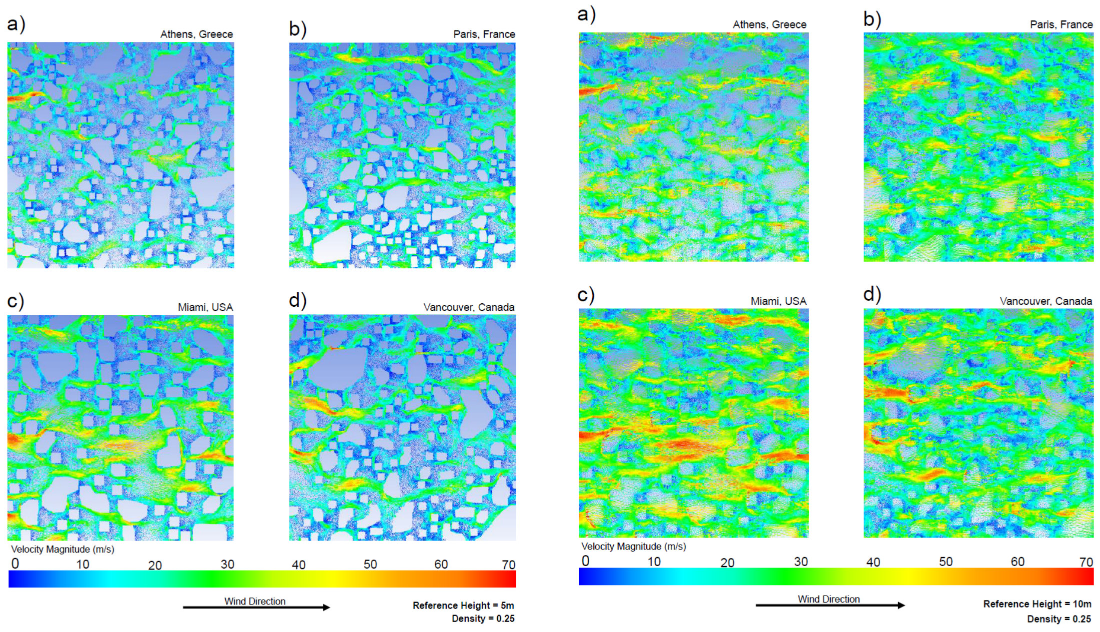

(a) Velocity at $z = h/2 = 5m$

(b) Velocity at $z = h = 10m$

Figure 5-13: Velocity magnitude over the 4 computed cities

and the type of flow affects this metric.

$$\int_A dPdA = D \tag{5.12}$$

One more calculated value is the dynamic pressure q, this value includes a more accurate way of calculating the drag coefficient. We are using the velocity and pressure values close to the buildings,[29].

$$Cd = \frac{2D}{A\rho V^2} \tag{5.13}$$

$$q = \frac{1}{2}\rho V^2 \tag{5.14}$$

The quantity one half the density times the velocity squared is called the dynamic pressure q. The drag coefficient then expresses the ratio of the drag force to the force produced by the dynamic pressure times the area,[30].

$$Cd = \frac{Dq}{A} \tag{5.15}$$

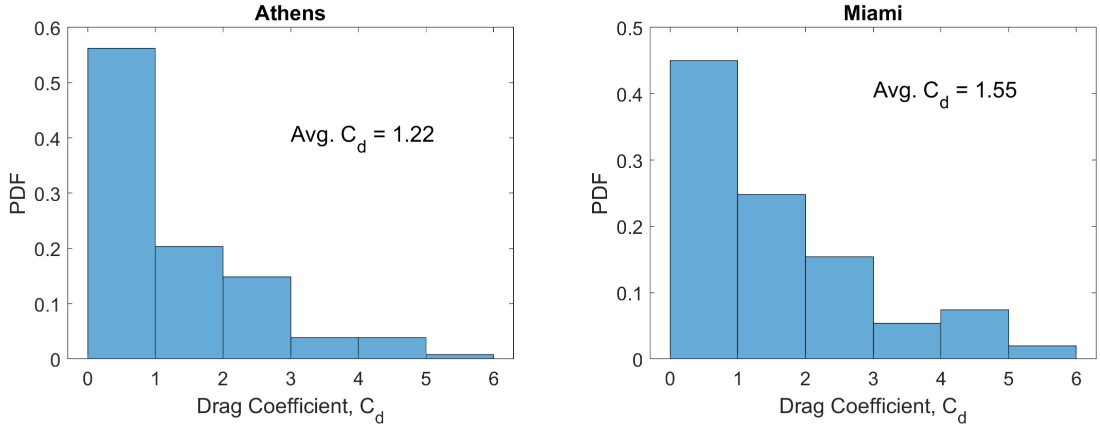

(a) Athens-Liquid structure

(b) Paris-Gas strucure

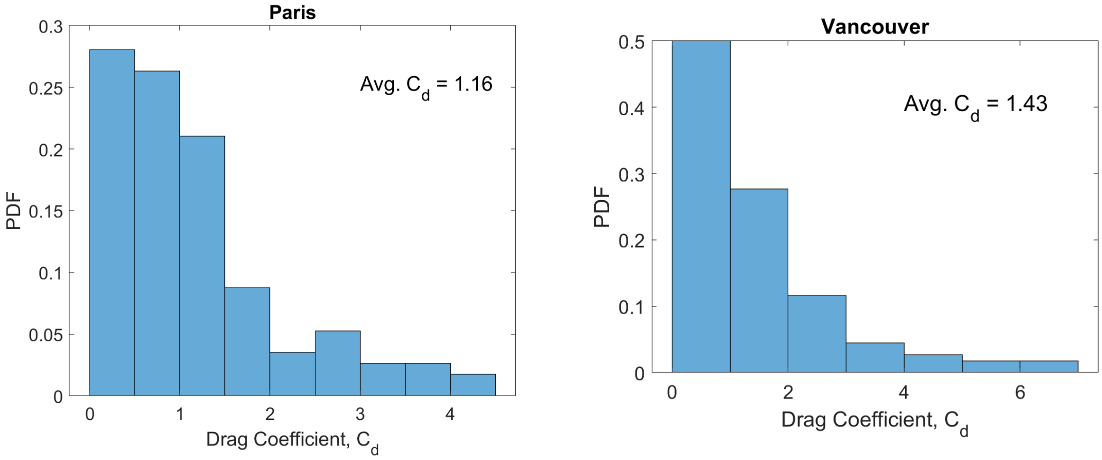

(c) Miami-Liquid strucure

(d) Vancouver crystal structure

Figure 5-14: PDF drag coefficient for the computed cities

5.12 Utilizing the calculations with CFD software PUMA

A comparison model of two buildings has been implemented to extend the methodology by using an open source CFD solver. The aim of this approach is to establish highly accurate results by using non commercial solvers. To this end, a comparison between the Ansys solutions and the CFD code, [87],[13], [88], of the of Parallel CFD & Opitimization Unit of NTUA is made.

5.12.1 Parallel Unstructured Multirow and Adjoint code, PUMA

Some details for the PUMA computations are given below. The GPU code PUMA (Parallel Unstructured Multirow and Adjoint) by the PCOpt/NTUA has been implemented to compute the pressure and velocity fields around the buildings.The mesh created for both computations has 78587 nodes and 420584 hedra. The mesh as described is depicted in the Figure 5-16.

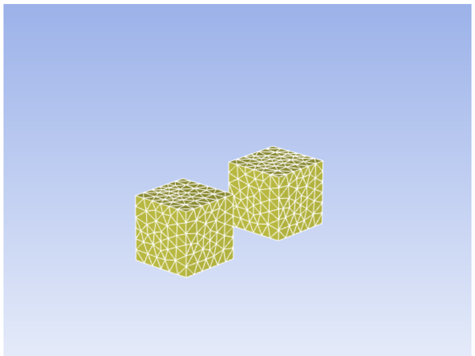

Figure 5-15: Surface mesh around two adjoint buildings used for both simulations

A steady computation is performed using the Spalart-Allmaras turbulence model with wall functions. A no-slip condition is imposed on the velocity field at all the solid boundaries of the buildings and wall functions are used for the turbulence variables at the wall. The incoming velocity is set to 55m/s which resembles a hurricane category 3. The case configuration of Ansys is done by the same way.

Flow prediction based on the PUMA code gave very quick results by using a

16 GB GPU memory NVIDIA Tesla P100 (Pascal).The overall duration of the code was 7 minutes. The same computation using Ansys software and a 3.1 GHz Core i7 (I7-7920HQ) lasts more than 1 hour. By using PUMA, the solver is approximately 50 times faster than the equivalent CPU solver,[87].The primal invicid fluxes are computed using the Roe's approximate Riemann solver adapted to incompressible flows. The discretized equations are solved in each pseudo-time step using a point-implicit Jacobi iterative scheme,[88].

5.12.2 Spalart-Allmaras model

For both simulations PUMA and Ansys the same turbulent model has been implemented. The Spalart-Allmaras model,[25] is a relatively simple one-equation model that solves a modeled transport equation for the kinematic eddy (turbulent) viscosity. This embodies a relatively new class of one-equation models in which it is not necessary to calculate a length scale related to the local shear layer thickness. The Spalart-Allmaras model was designed specifically for aerospace applications involving wall-bounded flows and has been shown to give good results for boundary layers subjected to adverse pressure gradients. It is also gaining popularity in the turbomachinery applications. In its original form, the Spalart-Allmaras model is effectively a low-Reynolds-number model, requiring the viscosity-affected region of the boundary layer to be properly resolved.

The Spalart-Allmaras [25]uses a single transport equation to model the kinematic eddy viscosity by introducing the viscosity variable, known as the Spalart-Allmaras variable, ν_t

$$\nu_t = \widetilde{\nu} f_{v1} \tag{5.16}$$

$$f_{v1} = \frac{X^3}{X^3 + C_{v1}^3} \tag{5.17}$$

$$X = \frac{\widetilde{\nu}}{\nu} \tag{5.18}$$

In order yo obtain the Spalart-Allmaras variable ν_t a single PDE is iteratively solved, which is the following.

$$\frac{\partial(\widetilde{\nu}u_j)}{\partial x_j} = C_{b1}(1-f_{t2})\widetilde{S}\widetilde{\nu} - [C_{w1}f_w - \frac{C_{b1}}{\kappa^2}f_{t2}] + (\frac{\widetilde{\nu}}{d})^2 + \frac{1}{\sigma}[\frac{\partial}{\partial x_j}((\widetilde{\nu}+\nu)\frac{\partial(\widetilde{\nu})}{\partial x_j})] + C_{b2}\frac{\partial\widetilde{\nu}}{\partial x_j}\frac{\partial\widetilde{\nu}}{\partial x_j}] \tag{5.19}$$

where $\sigma = 2/3, C_{b1} = 0.1355, C_{b2} = 0.622, \kappa = 0.41, C_{w1} = 3.239, C_{v1} = 7.1$ are the turbulence model constants.

5.12.3 Comparison of the Results

The drag coefficient values provided by both solvers, are close enough, as depicted on the table below.

	PUMA	**ANSYS**
cd	0.1219	0.1348

The drag coefficient of the second building has been compared, based on the methodology of the previous approach.The loads on the first building are not representative. On the figure 5-17 a comparison between the results of the two methods can be made.

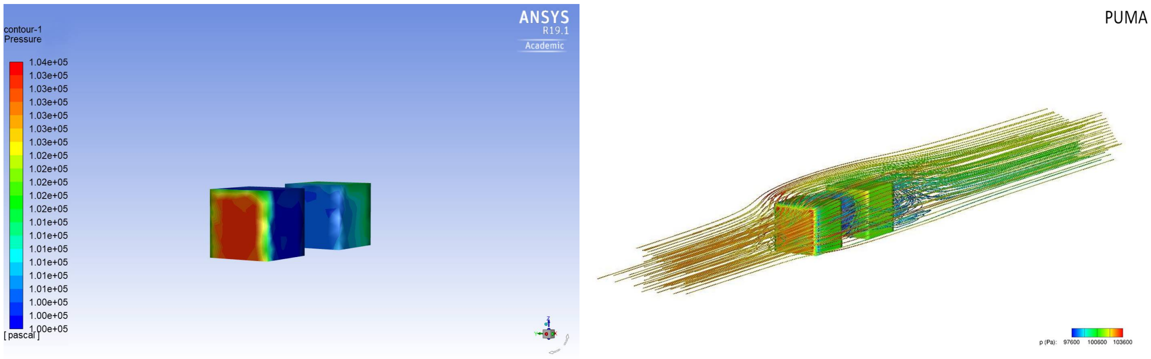

(a) Pressure distribution, ANSYS (b) Pressure distribution, PUMA

Figure 5-16: Comparison of the results using ANSYS and PUMA

The accurate results for both codes, suggest that the simulations could be implemented by using the PUMA code for the entire city. This could help to reduce the computational time since the code gives the same results in a significant faster time.

A constraint for the size of the mesh in the computations of the entire city was due to high computational time/cost, a solution, using PUMA, could help to get more accurate results.

5.13 Summary

In this chapter a model to create synthetic cities has been demonstrated. A Monte Carlo Simulation has been implemented in order to generate these synthetic cities. On this synthetic cities a cfd simulation has been applied for the investigation of the correlation between city patterns and the drag coefficient.

Chapter 6

Conclusion and Future Work

6.1 Conclusion and Future Work

It is important to recognize that herein obtained values, which we used to derive urban design guidelines, are averages obtained from GIS information for thousands of buildings with their shapes generalized to a simple square model. In real life, urban designs are highly complex procedures that focus on various pragmatic aspects of sustainability, resilience and living comfort[84]. To quantify geometrical characteristics of cities, we require input data of building footprints. While these can be obtained from GIS city departments, generally data sets of this kind are limited to large cities in the US and few cities in Europe. To overcome this issue, we established a method that allows us to obtain building footprints for any city in the world using online maps. Using buffer and clustering algorithms we were able to improve city texture computations to account for diverse shapes of cities and their non-impervious parts. To understand the impact that city texture has on surface temperature, we utilized daytime satellite images, which only in recent years have managed to capture high resolution measurements for an entire city. Lastly, using Grand Canonical Monte Carlo technique we increased statistical accuracy of our synthetic city models used in calculations of wind loads. A strong correlation between ϕ and cn has been established that allows us to create synthetic cities only by respecting the radial distribution function. All the presented parameters R,cn,ϕ,ρ_{gr},r_cut except the area of the city and buildings can be captured by g(r). For this analysis the restriction of not taking the area into account was not significant since the cfd calculations where based on same densities for all the cities. However this limitation should be prevailed in order to quantify synthetic cities in a better manner.For the cfd analysis further calculations and more cities should verify the conclusion that crystal cities intensify the drag coefficient. To establish a more accurate value for the drag coefficient of the city, a simulation with a rotating wind should be applied. An additional goal of this work was to add the height distribution of the buildings in the synthetic cities, however the lack on data in OpenStreetMap (OSM) hindered this goal though OSM data are constantly updated and the height of the buildings will be available for the most populous cities soon. The limitation of computer power as much as the lack of time forced us to a limit in cells of computations but on the same time with a large number of buildings. An investigation of the sensitivity of buildings number could establish the best correlation of computational time- mesh accuracy and the calculated drag. Moreover for UHI calculations a further investigation on the separation of rural and urban areas should be established. Additional to our approach an automatic procedure for evaluation of satellite images and download should be added as already described in chapter 3. For most of the cities five images were obtained with more data better and more accurate results could be derived. At last one very challenging computation that has not been established yet is to find the correlation between land surface temperature and air temperature.

Appendix A

Tables

Date	**Mean_TsR**	**MeanTsC**	**stD_TsR**	**std_TsC**	**UHI**
2014/04/10	18.971780	19.916831	1.793097	1.921174	0.945051
2014/07/31	25.414646	28.185454	2.633450	1.978522	2.770808
2014/09/17	22.372360	24.574625	2.608490	2.107935	2.202265
2014/10/03	20.512500	22.419661	2.108422	1.676526	1.907161
2015/01/23	1.304146	1.887326	0.767336	1.099920	0.583180
2014/03/16	7.333279	8.440672	1.829621	1.790671	1.107393
2014/04/01	15.399548	16.552726	1.796916	2.068309	1.153178
2014/05/19	23.611600	25.743500	3.044739	3.730618	2.131899
2014/07/06	30.300887	33.298153	2.845616	2.130490	2.997266
2014/08/07	26.538692	28.957320	2.510110	1.942997	2.418628
2014/12/13	3.502161	3.262574	0.829077	1.216524	-0.239587
2015/05/22	25.415871	27.727838	2.997743	2.474662	2.311967
2015/06/07	18.650106	22.747070	2.967946	2.470277	4.096964
2015/07/25	29.612320	31.283246	3.262153	4.373717	1.670926

Table A.1: UHI values for New York, where MeanTsR is the mean temperature of the rural area, MeanTsC the mean temperature of the urban area, std is the standard deviation for urban and rural temperatures

Bibliography

[1] 15 free satellite imagery data sources. `https://landsat.gsfc.nasa.gov/landsat-8/landsat-8-overview/`. [Online; accessed 19-August-2018].

[2] 15 free satellite imagery data sources. `https://gisgeography.com/free-satellite-imagery-data-list/`. [Online; accessed 19-August-2018].

[3] Landsat 8 (l8) data users handbook. `https://landsat.usgs.gov/sites/default/files/documents/LSDS-1574_L8_Data_Users_Handbook.pdf`. [Online; accessed 19-August-2018].

[4] List of european capitals. `https://www.countries-ofthe-world.com/capitals-of-europe.html`. [Online; accessed 19-August-2018].

[5] Ndvi, the foundation for remote sensing phenology. `https://phenology.cr.usgs.gov/ndvi_foundation.php`. [Online; accessed 19-August-2018].

[6] Normalized difference vegetation index (ndvi). `https://earthobservatory.nasa.gov/Features/MeasuringVegetation/measuring_vegetation_2.php`. [Online; accessed 19-August-2018].

[7] Projections in geogrpahic information systems. `http://web.mit.edu/1.961/fall2001/projections.htm`. [Online; accessed 19-August-2018].

[8] What are the band designations for the landsat satellites? `https://landsat.usgs.gov/what-are-band-designations-landsat-satellites`. [Online; accessed 19-August-2018].

[9] What are the best spectral bands to use for my study? `https://landsat.usgs.gov/what-are-best-spectral-bands-use-my-study`. [Online; accessed 19-August-2018].

[10] What is ndvi (normalized difference vegetation index)? `https://gisgeography.com/ndvi-normalized-difference-vegetation-index/`. [Online; accessed 19-August-2018].

[11] J. Allegrini and J. Carmeliet. Simulations of local heat islands in zürich with coupled CFD and building energy models. *Urban Climate*, 24:340–359, jun 2018.

[12] J. Allegrini, V. Dorer, and J. Carmeliet. Influence of morphologies on the microclimate in urban neighbourhoods. 144:108–117.

[13] V. G. Asouti, X. S. Trompoukis, I. C. Kampolis, and K. C. Giannakoglou. Unsteady cfd computations using vertex-centered finite volumes for unstructured grids on graphics processing units. *International Journal for Numerical Methods in Fluids*, 67(2):232–246.

[14] U. Avdan and G. Jovanovska. Algorithm for automated mapping of land surface temperature using LANDSAT 8 satellite data. 2016:1–8.

[15] U. Avdan and G. Jovanovska. Algorithm for automated mapping of land surface temperature using LANDSAT 8 satellite data. *Journal of Sensors*, 2016:1–8, 2016.

[16] M. Batty. Model cities. *Town Planning Review*, 78(2):125–151, mar 2007.

[17] M.J. Brown, R.E. Lawson, D.S. DeCroix, and R.L. Lee. Comparison of centerline velocity measurements obtained around 2d and 3d building arrays in a wind tunnel. page 8.

[18] L. Chen, J. Hang, M. Sandberg, L. Claesson, S. Di Sabatino, and H. Wigo. The impacts of building height variations and building packing densities on flow adjustment and city breathability in idealized urban models. 118:344–361.

[19] L. Chen, J. Hang, M. Sandberg, L. Claesson, S. Di Sabatino, and H. Wigo. The impacts of building height variations and building packing densities on flow adjustment and city breathability in idealized urban models. *Building and Environment*, 118:344–361, jun 2017.

[20] X.-L. Chen, H.-M. Zhao, P.-X. Li, and Z.-Y. Yin. Remote sensing image-based analysis of the relationship between urban heat island and land use/cover changes. *Remote Sensing of Environment*, 104(2):133–146, sep 2006.

[21] W.C. Cheng and F. PortÃľ-Agel. Adjustment of turbulent boundary-layer flow to idealized urban surfaces: A large-eddy simulation study. 155(2):249–270.

[22] D. H. J. Chung and M. Choo. Computational fluid dynamics for urban design: The prospects for greater integration. *International Journal of Architectural Computing*, 9(1):33–53, mar 2011.

[23] O. Coceal, T. G. Thomas, I. P. Castro, and S. E. Belcher. Mean flow and turbulence statistics over groups of urban-like cubical obstacles. 121(3):491–519.

[24] Eurostat (European Commission). Statistics on cities, towns and suburbs : 2016 edition, 2016. [Online; accessed 19-August-2018].

[25] [ANSYS] contributors. Filtered navier-stokes equations. `http://www.afs.enea.it/project/neptunius/docs/fluent/html/th/node94.htm`. [Online; accessed 19-August-2018].

[26] [ANSYS] contributors. Mesh quality. `https://www.sharcnet.ca/Software/Ansys/17.0/en-us/help/flu_ug/flu_ug_mesh_quality.html`. [Online; accessed 19-August-2018].

[27] [ANSYS] contributors. Rng k-ϵ model. `https://www.sharcnet.ca/Software/Ansys/16.2.3/en-us/help/flu_th/flu_th_sec_turb_rng.html`. [Online; accessed 19-August-2018].

[28] [CFD Online] contributors. K-epsilon models. `https://www.cfd-online.com/Wiki/K-epsilon_models`. [Online; accessed 19-August-2018].

[29] [NASA] contributors. The drag coefficient. `https://www.grc.nasa.gov/WWW/k-12/airplane/dragco.html`. [Online; accessed 19-August-2018].

[30] [NASA] contributors. Dynamic pressure. `https://www.grc.nasa.gov/WWW/k-12/airplane/dynpress.html`. [Online; accessed 19-August-2018].

[31] P. Davoudabadi. The most accurate and advanced turbulence capabilities. page 47.

[32] C. Dempsey. Calculating polygon area in arcmap. `https://www.gislounge.com/calculating-polygon-area-in-arcmap/`. [Online; accessed 19-August-2018].

[33] A. R. dos Santos, F. S. Oliveira, and A. Silva et al. Spatial and temporal distribution of urban heat islands. *Science of The Total Environment*, 605-606:946–956, dec 2017.

[34] ESA. World urbanization prospects: Highlights. `"https://esa.un.org/unpd/wup/publications/files/wup2014-highlights.pdf"`, 2014. [Online; accessed 19-August-2018].

[35] ESA. World urbanization prospects: The 2018 revision. `"https://esa.un.org/unpd/wup/Publications/Files/WUP2018-KeyFacts.pdf"`, 2018. [Online; accessed 19-August-2018].

[36] R.C. Estoque, Y. Murayama, and S.W. Myint. Effects of landscape composition and pattern on land surface temperature: An urban heat island study in the megacities of southeast asia. 577:349–359.

[37] R. Florida. The most famous models for how cities grow are wrong, 2013. [Online; accessed 19-August-2018].

[38] G. Forzieri, A. Cescatti, F. Batista, and L. Feyen. Increasing risk over time of weather-related hazards to the european population: a data-driven prognostic study. *The Lancet Planetary Health*, 1(5):e200–e208, aug 2017.

[39] S.S. Garud, I.A. Karimi, and M. Kraft. Design of computer experiments: A review. 106:71–95.

[40] M. Ghandehari, T. Emig, and M. Aghamohamadnia. Surface temperatures in new york city: Geospatial data enables the accurate prediction of radiative heat transfer. *Scientific Reports*, 8(1), feb 2018.

[41] E. GutiÃľrrez, A. Martilli, J. L. Santiago, and J. E. GonzÃąlez. A mechanical drag coefficient formulation and urban canopy parameter assimilation technique for complex urban environments. 157(2):333–341.

[42] K. R. Hope. Urbanization and urban growth in africa. *Journal of Asian and African Studies*, 33(4):345–358, jan 1998.

[43] E. Igun and M. Williams. Impact of urban land cover change on land surface temperature. *Global Journal of Environmental Science and Management*, 4(1), Jan 2018.

[44] J. C. J.-Muñoz, J. A. Sobrino, A. Gillespie, D. Sabol, and W. T. Gustafson. Improved land surface emissivities over agricultural areas using ASTER NDVI. *Remote Sensing of Environment*, 103(4):474–487, aug 2006.

[45] J. Samenow. Red-hot planet: All-time heat records have been set all over the world during the past week. `https://www.washingtonpost.com/news/capital-weather-gang/wp/2018/07/03/hot-planet-all-time-heat-records-have-been-set-all-over-the-world-in-last-week/?utm_term=.1260ab5a1470`, 2018. [Online; accessed 19-August-2018].

[46] B. Johnson, R. Tateishi, and T. Kobayashi. Remote sensing of fractional green vegetation cover using spatially-interpolated endmembers. 4(9):2619–2634.

[47] I.C. Kampolis, X.S. Trompoukis, V.G. Asouti, and K.C. Giannakoglou. Cfd-based analysis and two-level aerodynamic optimization on graphics processing units. *Computer Methods in Applied Mechanics and Engineering*, 199(9):712 – 722, 2010.

[48] M. Kanda, R. Moriwaki, and F. Kasamatsu. Large-eddy simulation of turbulent organized structures within and above explicitly resolved cube arrays. 112(2):343–368.

[49] N. Katsantonis and D. Bilefsky. Outskirts of athens hit by deadly flash floods. `https://www.nytimes.com/2017/11/15/world/europe/athens-deadly-flash-floods.html?module=ArrowsNav&contentCollection=Europe&action=keypress&region=FixedLeft&pgtype=article`, 2017. [Online; accessed 19-August-2018].

[50] K. Keremidis, M. J. A. Qomi, R. J.-M Pellenq, and F.-J. Ulm. A resilience assessment of structures using molecular dynamics. *Research Brief*, 6, 2018.

[51] J.J. Kim and D.Îĕ. Kim. Effects of a building's density on flow in urban areas. *Advances in Atmospheric Sciences*, 26(1):45–56, jan 2009.

[52] J.J. Kim and D.Y. Kim. Effects of a buildingâĂŹs density on flow in urban areas. 26(1):45–56.

[53] Gergely KristÃşf and PÃľter FÃijle. Optimization of urban building patterns for pollution removal efficiency by assuming periodic dispersion. 162:85–95.

[54] L. KukaÄŊka, Åă. Nosek, R. KellnerovÃą, K. JurÄŊÃąkovÃą, and Z. JaÅĹour. Wind tunnel measurement of turbulent and advective scalar fluxes: A case study on intersection ventilation. 2012:1–13.

[55] B. Li, J. Liu, and J. Gao. Surface wind pressure tests on buildings with various non-uniformity morphological parameters. 137:14–24.

[56] B. Li, J. Liu, and M. Li. Wind tunnel study on the morphological parameterization of building non-uniformity. 121:60–69.

[57] H. Li, Y. Zhou, X. Li, L. Meng, X. Wang, S. Wu, and S. Sodoudi. A new method to quantify surface urban heat island intensity. *Science of The Total Environment*, 624:262–272, may 2018.

[58] M. Li, J. Guo, M. Xiong, and C. Xiang. Heat island effect on outdoor meteorological parameters for building energy-saving design in a large city in northern china. *International Journal of Global Warming*, 14(2):224, 2018.

[59] Z. Li, B. Tang, H. Wu, H. Ren, G. Yan, Z. Wan, .F. Trigo, and J.A. Sobrino. Satellite-derived land surface temperature: Current status and perspectives. 131:14–37.

[60] F. S. Lien and E. Yee. Numerical modelling of the turbulent flow developing within and over a 3-d building array, part i: A high-resolution reynolds-averaged navierâĂŞstokes approach. 112(3):427–466.

[61] M. Lin, J. Hang, Y. Li, Z. Luo, and M. Sandberg. Quantitative ventilation assessments of idealized urban canopy layers with various urban layouts and the same building packing density. 79:152–167.

[62] M. Lin, J. Hang, Y. Li, Z. Luo, and M. Sandberg. Quantitative ventilation assessments of idealized urban canopy layers with various urban layouts and the same building packing density. *Building and Environment*, 79:152–167, sep 2014.

[63] C. Loyd. Landsat 8 bands. `https://landsat.gsfc.nasa.gov/landsat-8/landsat-8-bands/`. [Online; accessed 19-August-2018].

[64] A. Martilli and J.L. Santiago. CFD simulation of airflow over a regular array of cubes. part II: analysis of spatial average properties. 122(3):635–654.

[65] T. Misra. East asia's massive urban growth, in 5 infographics, 2015. [Online; accessed 19-August-2018].

[66] A.F. Mohammad, S.A. Zaki, M.S.M. Ali, H. Aya, A.A. Razak, M. Shirakashi, and N. Arai. Large eddy simulation of wind pressure distribution on heterogeneous buildings in idealised urban models. 78:3055–3060.

[67] NASA. How climate is changing. `https://climate.nasa.gov/effects/`, 2017. [Online; accessed 19-August-2018].

[68] MIT Notes. Basics of turbulent flow. `http://www.mit.edu/course/1/1.061/www/dream/SEVEN/SEVENTHEORY.PDF`. [Online; accessed 19-August-2018].

[69] OpenStreetMap contributors. Boundaries map 4.3 - english. `https://wambachers-osm.website/index.php/projekte/internationale-administrative-grenzen/boundaries-map-4-3-english`. [Online; accessed 19-August-2018].

[70] OpenStreetMap contributors. Osm boundaries map 4.4.6. `https://wambachers-osm.website/boundaries/`. [Online; accessed 19-August-2018].

[71] S. Peng, S. Piao, P. Ciais, P. Friedlingstein, C. Ottle, F. BrÃľon, H. Nan, L. Zhou, and R. Myneni. Surface urban heat island across 419 global big cities. 46(2):696–703.

[72] L. Peres, A. Lucena, O. Rotunno Filho, and J. FranÃğa. The urban heat island in rio de janeiro, brazil, in the last 30 years using remote sensing data. 64:104–116.

[73] L. F. Peres, A. J. Lucena, O. C. R. Filho, and J. R. França. The urban heat island in rio de janeiro, brazil, in the last 30 years using remote sensing data. *International Journal of Applied Earth Observation and Geoinformation*, 64:104–116, feb 2018.

[74] Q. and N. Li. Assessment of the impact of interdependencies on the resilience of networked critical infrastructure systems. *Natural Hazards*, 93(1):315–337, apr 2018.

[75] R. Ramponi, B. Blocken, L.B. de Coo, and W.D. Janssen. CFD simulation of outdoor ventilation of generic urban configurations with different urban densities and equal and unequal street widths. 92:152–166.

[76] M. Saeedi and B.C. Wang. Large-eddy simulation of turbulent flow and dispersion over a matrix of wall-mounted cubes. 27(11):115104.

[77] J. L. Santiago, O. Coceal, A. Martilli, and S. E. Belcher. Variation of the sectional drag coefficient of a group of buildings with packing density. 128(3):445–457.

[78] J.L. Santiago, A. Martilli, and F. MartÃŋn. CFD simulation of airflow over a regular array of cubes. part i: Three-dimensional simulation of the flow and validation with wind-tunnel measurements. 122(3):609–634.

[79] M. Schultz, J. Voss, M. Auer, S. Carter, and A. Zipf. Open land cover from OpenStreetMap and remote sensing. 63:206–213.

[80] L. Shen, Y. Han, C.S. Cai, and G. Dong. Large eddy simulation of the wind environment in urban residential areas based on an inflow turbulence generating method. page 21.

[81] Y. Shi, J. Qiu, R. Li, Q. Shen, and D. Huang. Identification of potential high-risk habitats within the transmission reach of oncomelania hupensis after floods based on SAR techniques in a plane region in china. 14(9):986.

[82] J. A. Sobrino, J. C. J. Muñoz, and L. Paolini. Land surface temperature retrieval from LANDSAT TM 5. *Remote Sensing of Environment*, 90(4):434–440, apr 2004.

[83] J. Sobstyl, R.-J. Pellenq, and F-J. Ulm. Prioritizing resilient retrofits. *Research Brief*, 2, 2018.

[84] J. M. Sobstyl, T. Emig, M. J. Abdolhosseini Qomi, F.-J. Ulm, and R. J.-M. Pellenq. Role of city texture in urban heat islands at nighttime. *Physical Review Letters*, 120(10), mar 2018.

[85] M. Stathopoulou and C. Cartalis. Daytime urban heat islands from landsat ETM+ and corine land cover data: An application to major cities in greece. *Solar Energy*, 81(3):358–368, mar 2007.

[86] F. Toja-Silva, C. P. Hoderlein, and J.Chen. On the urban geometry generalization for CFD simulation of gas dispersion from chimneys: Comparison with gaussian plume model. *Journal of Wind Engineering and Industrial Aerodynamics*, 177:1–18, jun 2018.

[87] X.S. Trompoukis, V.G. Asouti, I.C. Kampolis, and K.C. Giannakoglou. Chapter 17 - cuda implementation of vertex-centered, finite volume cfd methods on unstructured grids with flow control applications. In Wen mei W. Hwu, editor, *GPU Computing Gems Jade Edition*, Applications of GPU Computing Series, pages 207 – 223. Morgan Kaufmann, Boston, 2012.

[88] K. T. Tsiakas, Xenofon S. Trompoukis, Varvara G. Asouti, and Kyriakos C. Giannakoglou. *Design-Optimization of a Compressor Blading on a GPU Cluster*, pages 277–291. Springer International Publishing, Cham, 2015.

[89] Mirjana Velickovic, Yves Zech, and Sandra Soares-FrazÃčo. Steady-flow experiments in urban areas and anisotropic porosity model. 55(1):85–100.

[90] C. Wang, S.W. Myint, P. Fan, M. Stuhlmacher, and J. Yang. The impact of urban expansion on the regional environment in myanmar: a case study of two capital cities. 33(5):765–782.

[91] F. Wang, Z. Qin, C. Song, L. Tu, A. Karnieli, and S. Zhao. An improved mono-window algorithm for land surface temperature retrieval from landsat 8 thermal infrared sensor data. *Remote Sensing*, 7(4):4268–4289, apr 2015.

[92] Q. Weng, D. Lu, and J. Schubring. Estimation of land surface temperature–vegetation abundance relationship for urban heat island studies. *Remote Sensing of Environment*, 89(4):467–483, feb 2004.

[93] OpenStreetMap Wiki. Downloading data — openstreetmap wiki,. `http://wiki.openstreetmap.org/w/index.php?title=Downloading_data&oldid=1631037`, 2018. [Online; accessed 19-August-2018].

[94] OpenStreetMap Wiki. Key:building — openstreetmap wiki,. `"http://wiki.openstreetmap.org/w/index.php?title=Key:building&oldid=1577262"`, 2018. [Online; accessed 20-August-2018].

[95] Wikipedia contributors. Api — Wikipedia, the free encyclopedia. `https://en.wikipedia.org/w/index.php?title=Api&oldid=258346829`, 2008. [Online; accessed 19-August-2018].

[96] Wikipedia contributors. Arcgis — Wikipedia, the free encyclopedia. `https://en.wikipedia.org/w/index.php?title=ArcGIS&oldid=852372206`, 2018. [Online; accessed 19-August-2018].

[97] Wikipedia contributors. Fluid dynamics — Wikipedia, the free encyclopedia. `"https://en.wikipedia.org/w/index.php?title=Fluid_dynamics&oldid=854720427"`, 2018. [Online; accessed 19-August-2018].

[98] Wikipedia contributors. Monte carlo method — Wikipedia, the free encyclopedia. `"https://en.wikipedia.org/w/index.php?title=Monte_Carlo_method&oldid=854492318"`, 2018. [Online; accessed 19-August-2018].

[99] Wikipedia contributors. Normalized difference vegetation index — Wikipedia, the free encyclopedia. `"https://en.wikipedia.org/w/index.php?title=Normalized_difference_vegetation_index&oldid=852330725"`, 2018. [Online; accessed 19-August-2018].

[100] Wikipedia contributors. Satellite imagery — Wikipedia, the free encyclopedia. `"https://en.wikipedia.org/w/index.php?title=Satellite_imagery&oldid=849733099"`, 2018. [Online; accessed 19-August-2018].

[101] Wikipedia contributors. Shapefile — Wikipedia, the free encyclopedia. `https://en.wikipedia.org/w/index.php?title=Shapefile&oldid=846901488`, 2018. [Online; accessed 19-August-2018].

[102] Wikipedia contributors. Xml — Wikipedia, the free encyclopedia. `https://en.wikipedia.org/w/index.php?title=XML&oldid=853117384`, 2018. [Online; accessed 19-August-2018].

[103] Q. Yang, X. Huang, and J. Li. Assessing the relationship between surface urban heat islands and landscape patterns across climatic zones in china. 7(1).

[104] Q. Zhu, M. Hu, Y. Zhang, and Z. Du. Research and practice in three-dimensional city modeling. *Geo-spatial Information Science*, 12(1):18–24, jan 2009.

Διερεύνηση της Επίδρασης Αστικών Γεωμετριών σε Προβλήματα Αστικού Περιβάλλοντος μέσω Τεχνικών Υπολογιστικής Ρευστοδυναμικής

Τίνα Νεφέλη Βαρτζιώτη

Επιβλέποντες:

Κ.Χ. Γιαννάκογλου, Καθηγητής ΕΜΠ
F.J. Ulm, Καθηγητής MIT
R. Pellenq, Senior Research Scientist MIT

Εκτενής Περίληψη Διπλωματικής Εργασίας

Concrete Sustainability Hub
MASSACHUSETTS INSTITUTE of TECHNOLOGY
Μονάδα Παράλληλης Υπολογιστικής Ρευστοδυναμικής & Βελτιστοποίησης
ΕΘΝΙΚΟ ΜΕΤΣΟΒΙΟ ΠΟΛΥΤΕΧΝΕΙΟ
Οκτώβριος 2018

Κεφάλαιο 1

Εισαγωγή

1.1 Εισαγωγή

Σε αυτό το κεφάλαιο, γίνεται αναφορά στην αστική ανάπτυξη και το ρόλο αυτής σε περιβαλλοντικά ζητήματα. Επιπλέον, περιγράφονται οι διάφορες προσεγγίσεις για τη μοντελοποίηση αστικών δικτύων και τρόποι για την ποσοτικοποίησή τους. Η μοντελοποίηση και ποσοτικοποίηση είναι ιδιαίτερα σημαντικές προκειμένου να κατανοηθεί ο μελλοντικός αντίκτυπος στη βιωσιμότητα και την ανθεκτικότητα των πόλεων.

1.2 Αύξηση του Αστικού Πληθυσμού

Η ταχεία ανάπτυξη του αστικού πληθυσμού, η οποία αναπαρίσταται στο Σχήμα 1-1, δημιουργεί μια εντατική ανάγκη για την ανάπτυξη των αστικών υποδομών,[43]. Πολλές πόλεις έχουν βιώσει έντονες επεκτάσεις τόσο εδαφικές όσο και πληθυσμιακές.

1.3 Περιβαλλοντικά Ζητήματα

Οι θερμοκρασιακές συνθήκες στις αστικές περιοχές διαφέρουν σημαντικά από τις αγροτικές περιοχές. Η βλάστηση έχει αντικατασταθεί από άσφαλτο και μπετόν, που απορροφούν τη θερμότητα, η οποία απελευθερώνεται πάλι στην ατμόσφαιρα. Αυτή η αλλαγή είναι γνωστό ότι αυξάνει τη θερμοκρασία της επιφάνειας της γης, όπως φαίνεται στο Σχήμα 1-2,[43].

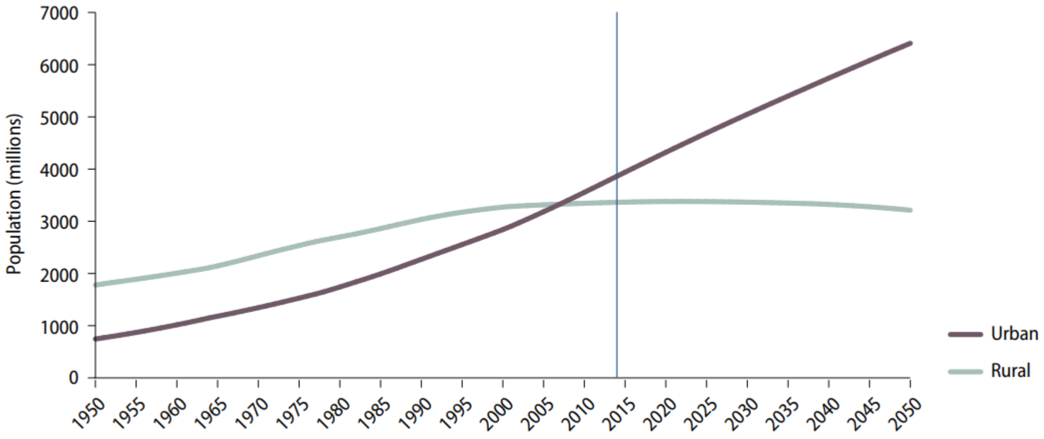

Σχήμα 1-1: Αστικός και υπαίθριος πληθυσμός του κόσμου 1950-2050, Ηνωμένα Έθνη

Προκειμένου να αντιμετωπιστεί η ανάγκη για ασφαλείς και φιλικές προς το περιβάλλον πόλεις, είναι απαραίτητη η εστίαση στα προβλήματα που εμφανίζονται σε αυτές, όπως είναι η αστική θερμονησίδα (Urban Heat Island UHI),οι τυφώνες, οι πλημμύρες και η ατμοσφαιρική ρύπανση.

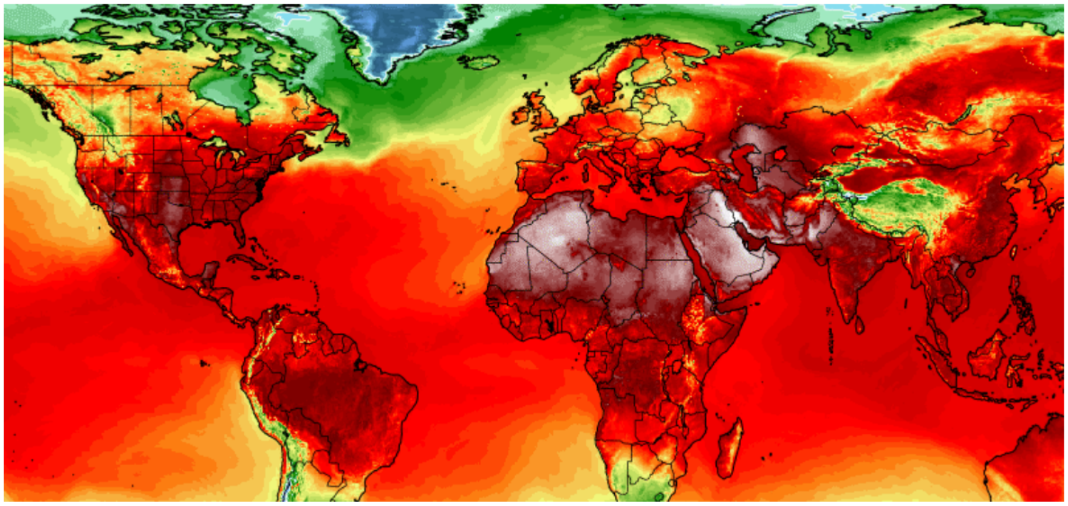

Simulation of maximum temperatures on July 3 from American (GFS) weather model at two meters above the ground. (University of Maine Climate Reanalyzer)

Σχήμα 1-2: Ρεκόρ καταγραφής τιμών θερμοκρασίας σε ολόκληρο τον κόσμο κατά την διάρκεια της πρώτης εβδομάδας του Ιουλίου 2018, Washington Post

1.4 Υπάρχοντα Μοντέλα Πόλεων

Τα μοντέλα αποτελούν μια απλοποιημένη απεικόνιση της πραγματικότητας. Σύμφωνα με τον Morrison [3] τα μοντέλα κατέχουν έναν αυτόνομο ρόλο στην επιστήμη και τον σχεδιασμό. Με άλλα λόγια, τα μοντέλα δεν μπορούν να λαμβάνονται ούτε ως θεωρία όυτε ως ισοδύναμα πραγματικά συστήματα. Συνεπώς, λειτουργούν ως εργαλεία τα οποία επιτρέπουν στους επιστήμονες και στους μηχανικούς να εξερευνήσουν τον κόσμο, να τον προβλέψουν και να σχεδιάσουν τις δράσεις τους πριν ενεργήσουν με αμετάκλητο τρόπο. Έχουν υπάρξει διάφοροι τρόποι μοντελοποίησης πόλεων είτε για τη πολεοδομία είτε για τη διεξαγωγή διαφορετικών στατικών και δυναμικών αναλύσεων. Τα υπάρχοντα μοντέλα πόλεων είναι:

- Επιχώρια μεταφορικά μοντέλα (land use transportation models) τα οποία αποτελούν τα πρώτα μαθηματικά μοντέλα αναπαράστασης μιας πόλης που προσομοίωσαν μετακινήσεις ανθρώπων, συσχετισμένες με εργασιακές δραστηριότητες μέσα στην πόλη.

- Μορφολογικά μόντελα (morphological models) τα οποία δανείζονται μοντέλα αναπαράστασης από τη στατιστική φυσική, δηλαδή απεικονίζουν τα κτίρια ως άτομα. Ένα τέτοιο μοντέλο αποτελεί και η συναρτηση ακτινικής κατανομής.

- Τρισδιάστατα μοντέλα πόλης (3-D city models) τα οποία μπορούν να αποθηκεύσουν οποιοδήποτε είδος χωρικών αστικών δεδομένων μαζί με τη γεωγραφική τους αναφορά πάνω στο χάρτη. Τέτοιες αναπαραστάσεις πόλεων είναι ακόμη πολύ περιορισμένες, με αποτέλεσμα αυτή η μέθοδος απεικόνισης να είναι σε πρώιμο σταδιο ακόμα.

Κεφάλαιο 2

Συλλογή ανοικτών δεδομένων

2.1 Εισαγωγή

Σε αυτό το κεφάλαιο παρουσιάζεται το πρώτο ζήτημα της διπλωματικής εργασίας. Αφορά την απόκτηση γεωμετρικών δεδομένων κτιρίων από το OpenstreetMap. Η ενασχόληση με ανοιχτά δεδομένα (open source data) ήταν ένα λογικό επακόλουθο της έλλειψης πληροφοριών κτιρίων πόλεων από τοπικές αρχές και πανεπιστήμια για πολλές ευρωπαϊκές πόλεις και κυρίως για την Αθήνα. Η παροχή και επεξεργασία αυτών των πληροφοριών παρέχει τη δυνατότητα ποσοτικοποίησης των πόλεων. Η μεθοδολογία της φιλτραρισμενης λήψης, του pre- and post- processing των δεδομένων αφορά την πληρότητα, την ποιότητα και την επεξεργασία των δεδομένων ύστερα από τη λήψη των ψηφιακών χαρτών. Στόχος αποτελεί ο υπολογισμός της συνάρτησης ακτινικής κατανομής (radial distribution function), g(r) για να περιγραφεί η δομή της πόλης (city texture). Τα δεδομένα χαρτών που απαιτούνται πρέπει να περιέχουν πληροφορίες που αφορούν τη διδιάστατη γεωμετρία των κτιρίων, την τοποθεσία τους πάνω στον χάρτη, καθώς και χαρακτηριστικά όπως η περίμετρος και η επιφάνειά τους. Τα δεδομένα των κτιρίων μετατρέπονται σε σημεία που διατηρούν τις πληροφορίες θέσης και επιφάνειας για τον υπολογισμό της συνάρτησης ακτινικής κατανομής, g(r). Η μοντελοποίηση των πόλεων με βάση τη συνάρτηση ακτινικής κατανομής παρουσιάζεται πιο αναλυτικά σε επόμενο κεφάλαιο. Για την επαλήθευση της εγκυρότητας των δεδομένων στους υπολογισμούς, αναπτύσσεται μια συγκριτική μελέτη μεταξύ δεδομένων πόλεων και των ανοικτών δεδομένων. Τα ανοικτά δεδομένα μπορούν εύκολα να αμφισβητηθούν για την πληρότητα και την ακρίβεια των πληροφοριών των κτιρίων που παρέχουν μιας και προέρχονται από χρήστες.

2.2 Μεθοδολογία

Σύμφωνα με το παρακάτω διάγραμμα ροής, Σχήμα 2-1, τα δεδομένα των χαρτών μετατρέπονται στην κατάλληλη μορφή για τους υπολογισμούς της μοντελοποίησης της πόλης. Η τελική μορφή των δεδομένων είναι ως σημεία όπως παρουσιάζονται στο Σχήμα 2-2.

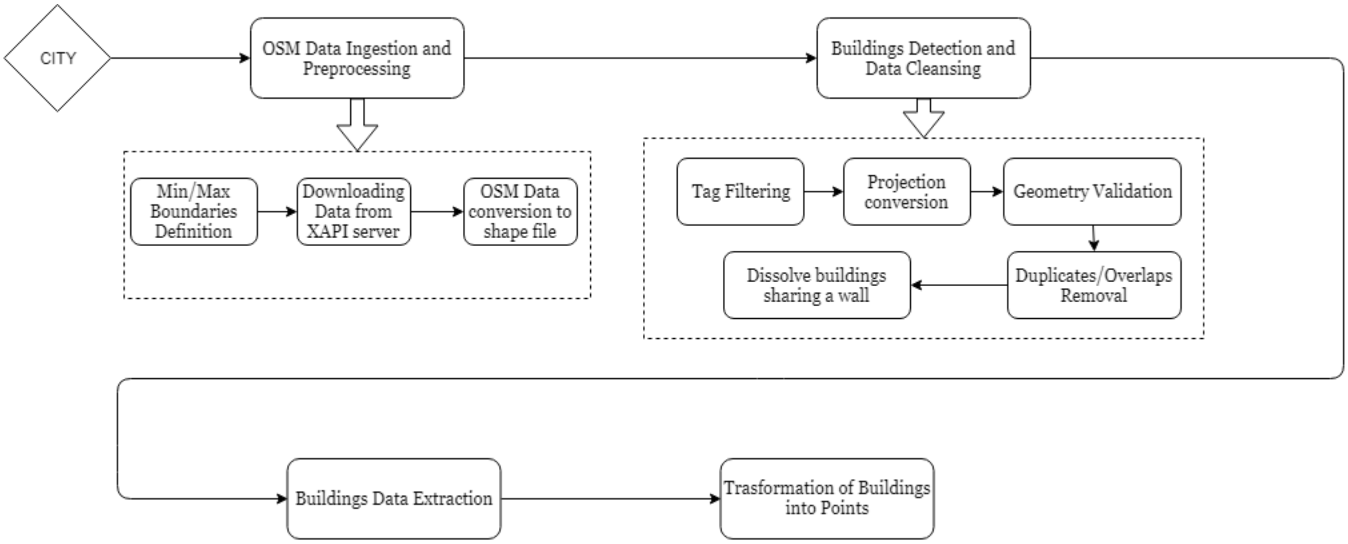

Σχήμα 2-1: Διάγραμμα ροής

2.3 Επαλήθευση των ανοικτών δεδομένων

Σε αυτήν την ενότητα θα παρουσιαστεί η ακρίβεια της χρήσης δεδομένων από το OpenstreetMap (OSM) για τον υπολογισμό της δομής πόλεων χρησιμοποιώντας τη συνάρτηση ακτινικής κατανομής, g(r). Συγκεκριμένα, για αυτή τη σύγκριση υπολογίστηκε η συνάρτηση ακτινικής κατανομής χρησιμοποιώντας τα δεδομένα από το σύστημα γεωγραφικών πληροφοριών (Geographic Information Systems, GIS) πόλεων και πανεπιστημίων και τα δεδομένα από

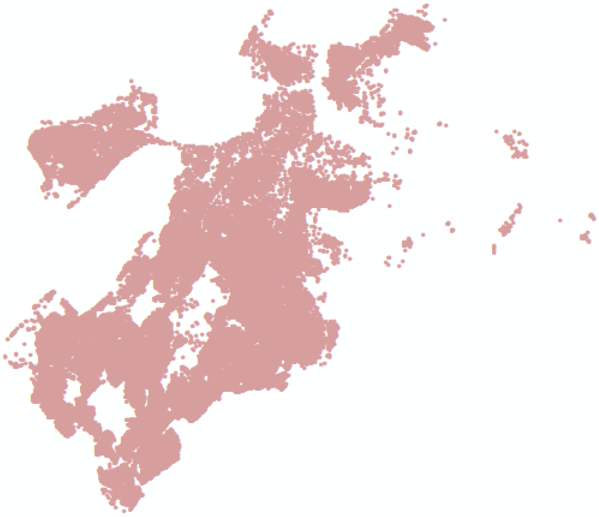

Σχήμα 2-2: Κτίρια που έχουν μετατραπεί σε σημεία

το OSM, όπως φαίνεται στο Σχήμα 2-3. Το g(r) υπολογίστηκε με τον ίδιο τρόπο όπως στην εργασία [85]. Αυτό σημαίνει ότι χρησιμοποιείται ένα buffer για συγκεκριμένες συντεταγμένες στην πόλη. Αργότερα χρησιμοποιείται μια διαφορετική προσέγγιση για το g(r), η οποία θα εξηγηθεί στο κεφάλαιο 3.

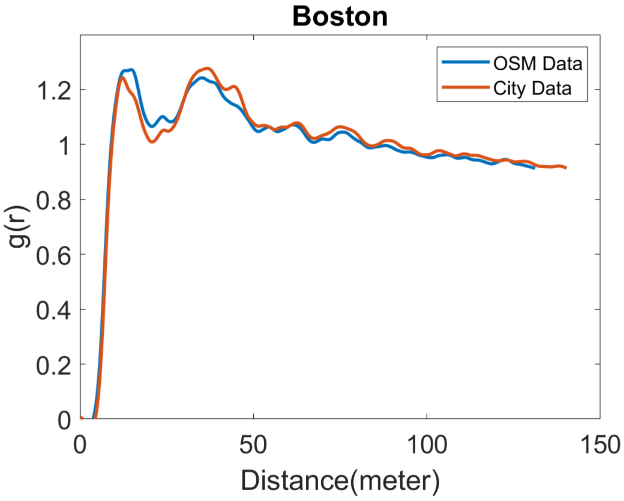

Σχήμα 2-3: Συνάρτηση ακτινικής κατανομής για την Βοστόνη χρησιμοποιώντας OSM και δεδομένα από το GIS τμήμα

Κεφάλαιο 3

Αστική Θερμονησίδα

3.1 Εισαγωγή

Αστική θερμονησίδα (Urban Heat Island, UHI) είναι ένα κλιματικό φαινόμενο τα αποτελέσματα του οποίου εμφανίζουν αυξημένη θερμοκρασία μέσα στις πόλεις όταν συγκρίνονται με τις γειτονικές μη αστικές περιοχές. Περισσότερο από 50% του πληθυσμού ζει σε πόλεις με αποτέλεσμα η αστικοποίηση να αποτελεί σημαντικό παράγοντα της υπερθέρμανσης του πλανήτη, [19]. Ακριβείς υπολογισμοί του UHI μπορούν να βοηθήσουν στην αξιολόγηση της πιθανότητας υψηλών θερμοκρασιών και να οδηγήσουν τις αρχές των πόλεων και κρατών σε σωστή ενεργειακή διαχείριση και σχεδιασμό. Το φαινόμενο της αστικής θερμικής νησίδας (Urban Heat Island, UHI) ορίζεται με δεδομένα θερμοκρασίας είτε από μετεωρολογικούς σταθμούς σε αστικές και αγροτικές περιοχές είτε με pixels μέσω θερμικών εικόνων. Συγκεκριμένα μπορεί να προσεγγιστεί συγκρίνοντας την θερμοκρασία αέρα σε αστικές περιοχές και στα περίχωρα βάσει δεδομένων από μετεωρολογικούς σταθμούς. Ένας άλλος τρόπος υπολογισμού αφορά το UHI υπολογισμένο για θερμοκρασία εδάφους (land surface temperature,LST), και στηρίζεται σε δεδομένα από δορυφόρους. Η χρήση των δορυφόρων είναι ο πιο κοινός τρόπος για τον υπολογισμό της θερμοκρασίας εδάφους και κατ' επέκταση και του UHI μέσω θερμοκρασίας εδάφους. Ο τρόπος υπολογισμού του φαινομένου UHI είναι ουσιαστικά η διαφορά μεταξύ των τιμών θερμοκρασιών των δύο περιοχών, αστικής και αγροτικής. Η θερμοκρασία στις αστικές περιοχές εμφανίζεται να έχει σημαντικά υψηλότερη τιμή σε σχέση με τα περίχωρα και παρατηρήθηκε από τους υπολογισμούς ότι το UHI αυξάνεται με την αύξηση της θερμοκρασίας. Αυτή η προσέγγιση του UHI δεν έχει παρατηρηθεί σε άλλες δημοσιεύσεις σχετικά με το φαινόμενο.

3.2 Δορυφορικά Δεδομένα

Ο δορυφόρος LandSat περνάει από την ίδια θέση στη γη κάθε 16 ημέρες. Η τροχιά του πηγαίνει από το βόρειο στο νότιο πόλο και καταγράφει ανά τακτά χρονικά διαστήματα μια νέα θέση. Αυτό συμβαίνει εδώ και 40 χρόνια, αλλά από το Δεκέμβριο του 2008 η πολιτική δεδομένων άλλαξε με αποτέλεσμα όλα τα δεδομένα LandSat να είναι διαθέσιμα σε οποιονδήποτε χωρίς περιορισμούς και κόστος. Υπήρξαν διάφοροι δορυφόροι LandSat, αλλά το Φεβρουάριο του 2013 το LandSat8 απογειώθηκε με εξοπλισμό, ο οποίος είχε πολύ καλύτερη ανάλυση σε σύγκριση με οποιαδήποτε άλλα όργανα δορυφορικής απεικόνισης. Η ανάλυση του προηγούμενο δορυφόρου, LandSat7, ήταν 500 μέτρα ενώ για το LandSat8 η ανάλυση είναι 100 μέτρα ,[1]. Αυτό το γεγονός δίνει την ευκαιρία λήψης ακριβέστερων αποτελεσμάτων για τον υπολογισμό της επιφανειακής θερμοκρασίας της γης. Υπάρχουν επίσης και άλλες πηγές δορυφορικών δεδομένων, όπως το MODIS που χρησιμοποιήθηκε σε πολλές έρευνες για την ποσοτικοποίηση του φαινομένου UHI, ωστόσο το LandSat8 έχει την υψηλότερη ανάλυση. Το LandSat8 μετρά 11 διαφορετικά εύρη συχνοτήτων κατά μήκος του ηλεκτρομαγνητικού φάσματος, κάθε εύρος-περιοχή ονομάζεται band. Έχει το κόκκινο, το πράσινο και το μπλε bands, τα 4, 3, 2 και ο συνδυασμός αυτών προσφέρει μια εικόνα αληθινών χρωμάτων, [64]. Τα δεδομένα συλλέγονται από δύο κύρια όργανα επί του δορυφόρου. Συγκεκριμένα, το LandSat8 φέρει τα εξής όργανα μέτρησης: το Operational Land Imager (OLI) και το Thermal Infrared Sensor (TIRS), [1]. Ειδικότερα το OLI συλλέγει εικόνες της επιφάνειας της γης σε εννέα διαφορετικά band ορατής και μη ορατής (υπέρυθρης) ακτινοβολίας. Τα band 4, 5 που χρησιμοποιούνται σε αυτή τη μελέτη έχουν ανάλυση 30 μέτρων. Αυτά χρησιμοποιούνται για τον υπολογισμό του κανονικοποιημένου δείκτη βλάστησης (Normalized Difference Vegetation Index, NDVI) που παρουσιάζεται παρακάτω στη μεθοδολογία. Το TIRS συγκεντρώνει εικόνες της επιφάνειας της γης σε δύο υπέρυθρα (θερμικά) bands, το band 10 και 11.

3.3 Διαχωρισμός Αστικών και Αγροτικών Περιοχών.

Πρώτο βήμα αποτελεί ο καθορισμός των ορίων της αγροτικής και της αστικής περιοχής. Μια πρώτη προσπάθεια ήταν να γίνει κλιμάκωση των όριων της πόλης. Αυτό φαίνεται να είναι μια ικανοποιητική προσέγγιση για πόλεις με κυκλικό σχήμα, όπως το Βερολίνο, το Παρίσι και το Λονδίνο, αλλά σε πόλεις όπως η Νέα Υόρκη και η Αθήνα δεν μπορεί να εφαρμοστεί. Η εξήγηση γι' αυτό βασίζεται στο γεγονός ότι τα όρια των συγκεκριμένων πόλεων εκτείνονται κυρίως προς μία κατεύθυνση και η αγροτική περιοχή δεν είναι ομοιογενής προς όλες τις κατευθύνσεις. Αυτό οδηγεί στη χρήση ενός buffer, του οποίου η ακτίνα υπολογίζεται αυξάνοντας τα όρια της πόλης σε 25 χιλιόμετρα. Το μέγεθος του buffer ή με άλλα λόγια τα όρια μεταξύ αγροτικής και αστικής περιοχής είναι μια προσέγγιση, στηριγμένη σε παρόμοιες έρευνες για την παρατήρηση των δορυφορικών δεδομένων, [21]. Αυτή η απόσταση ήταν η ελάχιστη δυνατή για την ύπαρξη επαρκών αγροτικών δεδομένων. Αυτή η μέθοδος εφαρμόστηκε με αυτόματο τρόπο, συνδυάζοντας τα όρια του OpenStreetMap και τις δορυφορικές εικόνες. Τα όρια της πόλης συγχωνεύονται σε ένα πολύγωνο, προβάλλονται από το πολικό σε καρτεσιανό σύστημα συντεταγμένων και μετατρέπονται σε μέτρα ενώ στην συνέχεια υπολογίζεται η περιοχή των ορίων και η επιφάνεια της πόλης. Υποθέτοντας ότι η περιοχή αντιπροσωπεύει έναν κύκλο υπολογίζεται η υποθετική ακτίνα. Υπολογίζεται το κέντρο μάζας των συνόρων της πόλης το οποίο ορίζεται ως το κέντρο του κύκλου. Το επόμενο βήμα είναι να δημιουργηθεί ένα buffer. Το κέντρο του buffer είναι το σημείο που δημιουργήθηκε σε προηγούμενα βήματα και η ακτίνα = υποθετική ακτίνα + 25 χλμ. Το τελευταίο βήμα είναι να δημιουργηθούν τα δύο διαφορετικά όρια για την αγροτική και την αστική περιοχή. Αυτό γίνεται με τη λήψη της συμμετρικής διαφοράς μεταξύ του buffer και των ορίων της πόλης.

3.4 Μεθοδολογία

Αυτή η μεθοδολογία έχει επίσης εφαρμοστεί με αυτοματοποιημένο τρόπο χρησιμοποιώντας Python και ArcGIS, συναρτήσεις . Τα απαιτούμενα input είναι τα αγροτικά και αστικά σύνορα από τα δεδομένα συνόρων του OpenstreetMap και τα ληφθέντα δορυφορικά δεδομένα. Η ροή εργασίας και η μεθοδολογία παρουσιάζεται στο παρακάτω Σχήμα 3-1. Για τον υπολογισμό των μέσων θερμοκρασίων για τις αγροτικές και τις αστικές περιοχές, γίνεται περικοπή των δορυφορικών εικόνων, όπως φαίνεται στο Σχήμα 3-2, χρησιμοποιώντας τα καθορισμένα όρια. Αυτό εφαρμόζεται σε όλα τα απαραίτητα bands για τους υπολογισμούς. Η χρήση των bands παρουσιάζεται σε περαιτέρω βήματα. Για να εξαχθούν οι τιμές θερμοκρασίας των pixel ακολουθείται η μέθοδος που παρέχεται από την Γεωλογική Υπηρεσία των ΗΠΑ (United States Geographical Survey, USGS).

- Βήμα 1 Ατμοσφαιρική Φασματική Ακτινοβολία - Top of Atmospheric Spectral Radiance.
  Τα μετρητικά όργανα OLI και TIRS του LandSat8 παρέχουν δεδομένα εικόνων σε μονάδες απόλυτης ακτινοβολίας. Αυτές οι τιμές μπορούν στη συνέχεια να μετατραπούν σε φασματική ακτινοβολία χρησιμοποιώντας τους συντελεστές κλίμακας ακτινοβολίας που παρέχονται στο αρχείο μεταδεδομένων, [5]. Το πρώτο βήμα του αλγορίθμου είναι η είσοδος της ζώνης (band) 10. Αφού εισαχθεί η ζώνη 10 χρησιμοποιούνται τύποι που λαμβάνονται από την ιστοσελίδα USGS για την ανάκτηση της top of atmospheric (TOA) φασματικής ακτινοβολίας (spectral radiance).

- Βήμα 2 Μετατροπή της ακτινοβολίας σε θερμοκρασία αισθητήρα.
  Αφού οι ψηφιακοί αριθμοί (DN) μετατραπούν σε ανάκλαση, τα δεδομένα ζώνης TIRS μετατρέπονται από τη φασματική ακτινοβολία (spectral radiance) σε θερμοκρασία φωτεινότητας (brightness temperature,BT) χρησιμοποιώντας τις θερμικές σταθερές που παρέχονται στο αρχείο μεταδεδομένων. Τα δεδομένα TIRS της θερμοκρασίας της φωτεινότητας (Atmosphere Brightness Temperature, TIRS) μπορούν επίσης να μετατραπούν από τη φασματική ακτινοβολία (spectral radiance), όπως περιγράφεται παραπάνω, στη θερμοκρασία φωτεινότητας (Atmosphere Brightness Temperature), η οποία είναι η πραγματική θερμοκρασία που βλέπει ο δορυφόρος.

- ΒΗΜΑ 3 Μέθοδος NDVI.
  Οι μελέτες, remote sensing phenology studies, χρησιμοποιούν δεδομένα που συλλέγονται από δορυφορικούς αισθητήρες που μετρούν μήκη κύματος φωτός που απορροφώνται και αντανακλώνται από πράσινα φυτά. Ορισμένες χρωστικές στα φύλλα των φυτών απορροφούν έντονα τα μήκη κύματος του ορατού (κόκκινου) φωτός. Τα

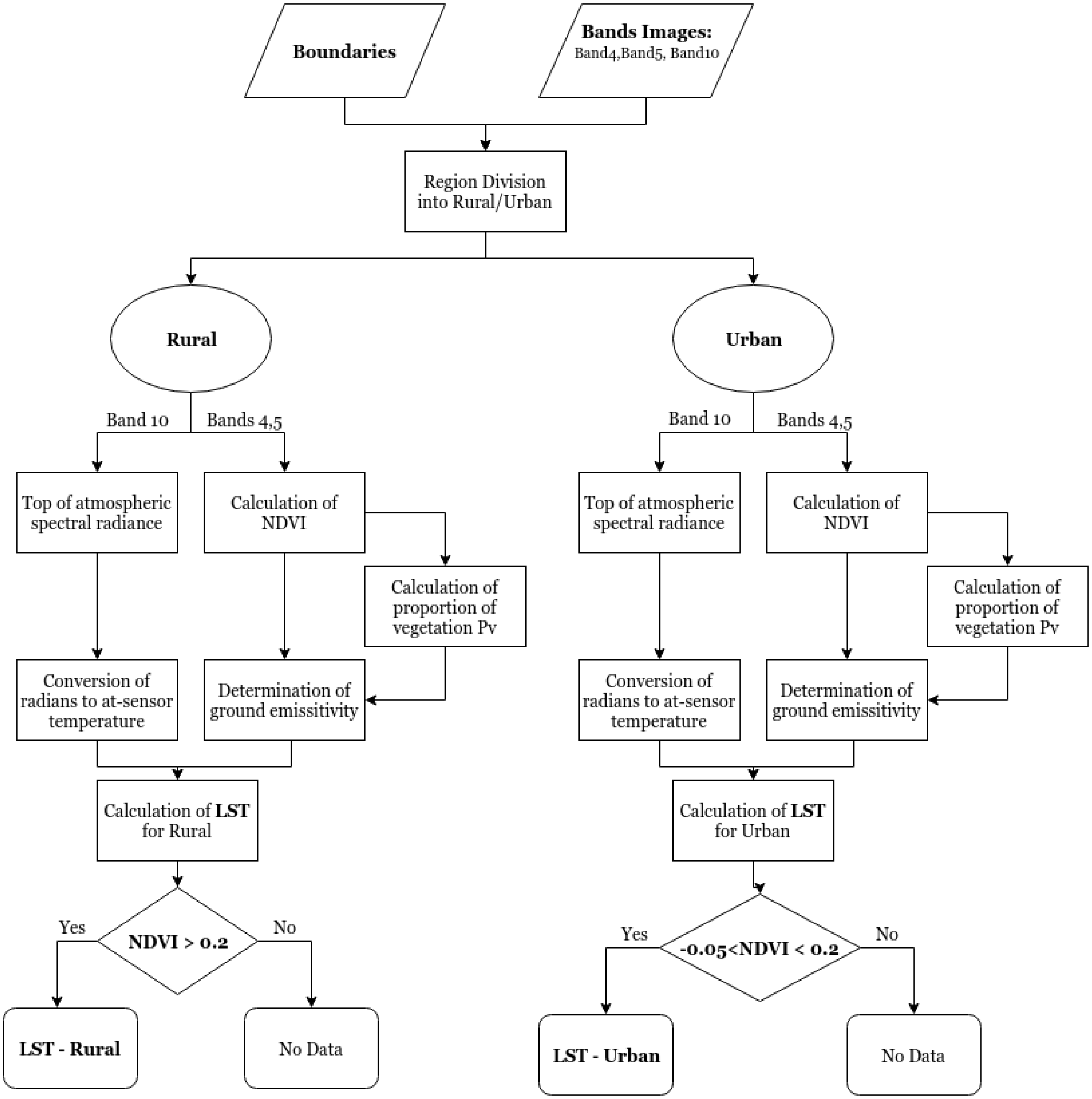

Σχήμα 3-1: Διάγραμμα ροής για τον υπολογισμό της θερμοκρασίας εδάφους

ίδια τα φύλλα αντανακλούν τα μήκη κύματος του εγγύς υπέρυθρου φωτός, το οποίο είναι αόρατο στο ανθρώπινο μάτι. Παρόλο που υπάρχουν διάφοροι δείκτες βλάστησης, ένας από τους πιο ευρέως χρησιμοποιούμενους είναι ο δείκτης βλάστησης κανονικοποιημένης διαφοράς (Normalized Difference Vegetation Index, NDVI). Οι τιμές NDVI κυμαίνονται από -1.0 έως +1.0. Περιοχές βραχώδεις, ερήμου ή χιονιού εμφα-

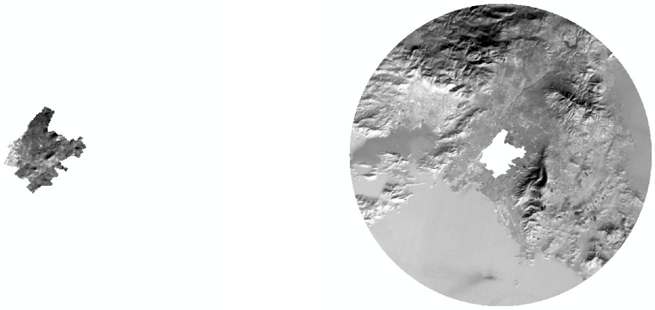

(α΄) Δορυφορική απεικόνιση της αστικής Αθήνας

(β΄) Δορυφορική απεικόνιση της υπαίθριας Αθήνας

Σχήμα 3-2: Δορυφορική απεικόνιση της Αθήνας.

νίζουν συνήθως πολύ χαμηλές τιμές NDVI (για παράδειγμα, 0.1 ή λιγότερο). Η αραιή βλάστηση, όπως θάμνοι και καλλιέργειες, έχουν ως αποτέλεσμα μέτριες τιμές NDVI (περίπου 0.2 έως 0.5). Οι υψηλές τιμές NDVI (περίπου 0.6 έως 0.9) αντιστοιχούν σε πυκνή βλάστηση όπως αυτή που απαντάται στα εύκρατα και τα τροπικά δάση ή στις καλλιέργειες στο μέγιστο στάδιο ανάπτυξής τους, [11]. LandSat ορατές (visible) και υπέρυθρες ζώνες (near-infrared bands) χρησιμοποιούνται για τον υπολογισμό του δείκτη NDVI. Ο υπολογισμός του NDVI είναι σημαντικός επειδή, στη συνέχεια, υπολογίζεται το ποσοστό της βλάστησης και συνδέεται σε μεγάλο βαθμό με την θερμοκρασία.

$$NDVI = \frac{NIR - R}{NIR + R} \tag{3.1}$$

όπου το NIR αντιπροσωπεύει τη ζώνη εγγύς υπερύθρου (ζώνη 5) και το R αντιπροσωπεύει την κόκκινη ζώνη (band 4), [12].

Μια πρόσθετη χρήση του NDVI έχει καθιερωθεί για τον διαχωρισμό των πράσινων-αγροτικών και των αστικών περιοχών. Για τον υπολογισμό της μέσης θερμοκρασίας των αστικών και αγροτικών περιοχών προσθέτουμε έναν επιπλέον περιορισμό στον αλγόριθμο. Για τις αγροτικές περιοχές μετατρέπουμε κτίρια ή δεδομένα μη-βλάστησης σε τιμές nodata και αντίστοιχα κάνουμε το ίδιο για αστικές περιοχές, εξαλείφουμε πάρκα και χώρους πρασίνου. Η σημασία αυτού του βήματος βασίζεται στις χαμηλότερες θερμοκρασίες των χώρων πρασίνου και στις υψηλότερες θερμοκρασίες των κτιρίων και του δρόμου. Για παράδειγμα, προσθέτοντας κεντρικό πάρκο στην αστική θερμοκρασία, μειώνεται η μέση θερμοκρασία της πόλης. Το UHI υπολογίζεται ως η διαφορά αυτών των μέσων τιμών.

3.5 Αποτελέσματα

Τα αποτελέσματα αυτής της διαδικασίας είναι πρώτα από όλα δορυφορικές εικόνες με τις τιμές θερμοκρασίας στα pixel τους. Δύο από τις 35 πόλεις παρουσιάζονται στα παρακάτω στοιχεία. Όπως φαίνεται στο Σχήμα 3-3 για την Αθήνα, ακόμα και με χρήση ακτίνας 25 χιλιομέτρων έξω από τα όρια της πόλης πολλές περιοχές εξακολουθούν να έχουν υψηλές τιμές θερμοκρασίας. Περιοχές όπως η Ελευσίνα με βιομηχανίες, όπως η ελληνική πετρελαϊκή εταιρεία, έχουν υψηλές τιμές θερμοκρασίας. Οι λευκές τιμές στις εικόνες είναι εικονοστοιχεία- pixel χωρίς δεδομένα. Παρατηρούμε ότι στην Αθήνα υπάρχουν πολλοί χώροι στο χάρτη χωρίς δεδομένα. Αυτό μπορεί να επαληθευτεί και με την παρατήρηση του NDVI της Αθήνας, στο Σχήμα 3-4, το οποίο δείχνει ποιες περιοχές καλύπτονται από κτίρια και ποιές είναι πράσινες.

Ένα ενδιαφέρον αποτέλεσμα αυτής της ανάλυσης είναι η συσχέτιση της θερμοκρασίας της υπαίθρου-πράσινων περιοχών και του UHI. Όπως φαίνεται στα παρακάτω γραφήματα υπάρχει μια γραμμική συσχέτιση μεταξύ της θερμοκρασίας της υπαίθρου και της πόλης. Αυτό σημαίνει ότι καθώς αυξάνεται η θερμοκρασία στην ύπαιθρο, η διαφορά θερμοκρασίας μεταξύ της αστικής και της αγροτικής θερμοκρασίας αυξάνεται. Αυτό μπορεί να μην έχει τεράστιες επιπτώσεις για τις χαμηλές θερμοκρασίες, αλλά για υψηλές θερμοκρασίες της τάξης 30°C στην αγροτική περιοχή καταλήγουν σε μια θερμοκρασία εντός της πόλης σε 35°C για πόλεις. Αυτό το αποτέλεσμα τονίζει το φαινόμενο UHI.

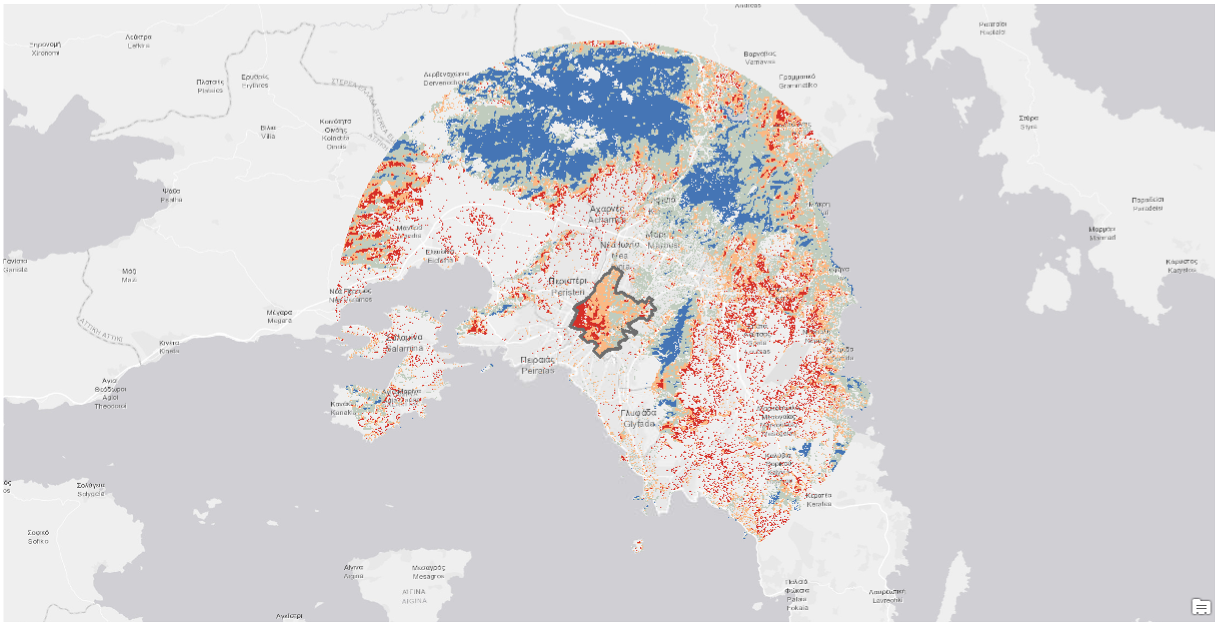

Σχήμα 3-3: Θερμοκρασία εδάφους στην Αθήνα

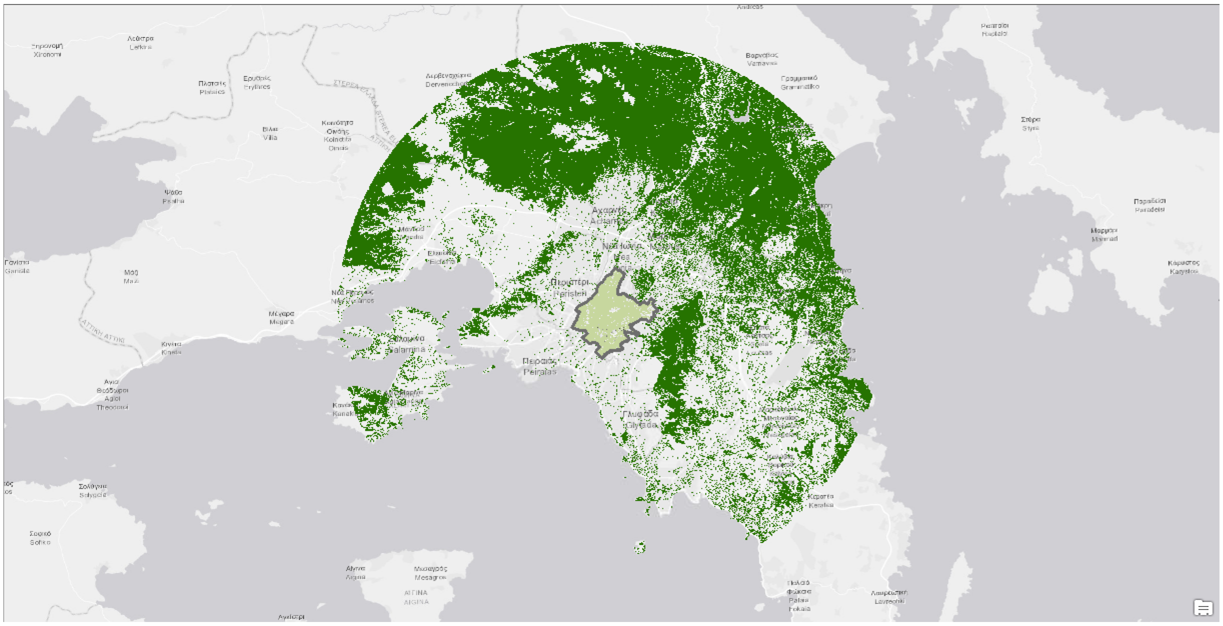

Σχήμα 3-4: Η μετρική NDVI για την πόλη της Αθήνας

Κεφάλαιο 4

Συνάρτηση ακτινικής κατανομής

Αυτό το κεφάλαιο ξεκινά με την εισαγωγή ενός παραλληλισμού μεταξύ της στατιστικής φυσικής και των αστικών μοντέλων. Αυτή η αναλογία επιτρέπει τη χρήση εργαλείων της στατιστικής φυσικής για την μοντελοποίηση των πόλεων. Αρχικά γίνεται μια γενική προσέγγιση για την ποσοτικοποίηση των πόλεων, η οποία πραγματοποιείται με τη χρήση της συνάρτησης ακτινικής κατανομής (radial distribution function), g(r). Αυτό το κεφάλαιο ολοκληρώνεται εξηγώντας τη χρήση του g(r), τη μοντελοποίηση των πόλεων μέσω αυτής και τη συσχέτισή του με το φαινόμενο UHI.

4.1 Ορισμός της συνάρτησης ακτινικής κατανομής, g (r) στις πόλεις

Η συνάρτηση ακτινικής κατανομής g(r) περιγράφει τον τρόπο με τον οποίο η τοπική πυκνότητα ποικίλλει από την μέση πυκνότητα. Παραδοσιακά, έχει χρησιμοποιηθεί για την διερεύνηση της δομής της ατομικής κλίμακας της συμπυκνωμένης ύλης. Στο πλαίσιο των κτιρίων, g(r) είναι η πιθανότητα να βρεθεί ένα κτίριο σε απόσταση r από το κτίριο αναφοράς. Η πυκνότητα στη στατιστική φυσική είναι η μέση πυκνότητα των σωματιδίων, τα οποία έχουν παρόμοιο μέγεθος. Αυτό δημιουργεί ορισμένους περιορισμούς όταν χρησιμοποιείται αυτή η μέθοδος για πόλεις, όπου τα κτίρια σε ολόκληρο το αστικό δίκτυο έχουν σημαντική διακύμανση μεγέθους. Ως αποτέλεσμα, λαμβάνεται ένα μέσο μέγεθος κτιρίου

L. Οι κορυφές στο g(r) εμφανίζονται όταν η τοπική πυκνότητα των κτιρίων αποκλίνει από τη μέση πυκνότητα της πόλης. Αυτές οι κορυφές μπορούν να μελετηθούν για να εξαχθούν πληροφορίες σχετικά με τα μεγέθη κτιριακών buffer χρησιμοποιώντας το ελάχιστο της συνάρτησης. Η απόσταση στην οποία το g (r) φθάνει στο πρώτο ελάχιστο ορίζεται ως το τοπικό μέγεθος buffer R. Ένα τέτοιο ορισμένο μέγεθος buffer είναι κρίσιμο για την ποσοτικοποίηση των παραμέτρων της πόλης, δηλαδή τον αριθμό των τοπικών γειτόνων, τη μέση απόσταση μεταξύ τους, τη τοπική πυκνότητα και τη χωρική παράμετρο (coordination parameter) που απεικονίζεται με την τοπική παράμετρο 2D Mermin Parameter. Συγκεκριμένα, χρησιμοποιώντας το g(r) για την ποσοτικοποίηση της δομής της πόλης, διαπιστώνεται ότι οι πόλεις έχουν διακριτές δομές που μοιάζουν με δομές κρυστάλλων, υγρών ή αερίων,[85].

4.2 Συσχέτιση δομής πόλεων και σωματιδιακής φυσικής:

Προκειμένου να εξαχθούν στατιστικά χαρακτηριστικά συσχετίζεται η δομή των πόλεων με τη δομή των σωματιδίων η οποία πραγματοποιείται με μια αναλογία μεταξύ κτιρίων και σωματιδίων. Η βασική πληροφορία που προέρχεται από το g(r) είναι η πιθανότητα εύρεσης γειτονικού σωματιδίου ή κτιρίου σε δεδομένη απόσταση από το σημείο αναφοράς. Μόλις η τοπική πυκνότητα αποκλίνει από τη μέση πυκνότητα του συστήματος, προκύπτουν οι κορυφές στην κατανομή. Σε στατιστικούς όρους σωματιδίων αυτό εξηγείται ως η πιθανότητα εύρεσης ατόμου σε απόσταση r από το άτομο αναφοράς. Αυτοί οι όροι που χρησιμοποιούνται στην κλίμακα της πόλης επιτρέπουν τον ορισμό της μέσης πυκνότητας κτιρίου. Χρησιμοποιώντας την αναλογία πόλης-σωματιδίων, δεδομένα που δίδονται από τη συνάρτηση ακτινικής κατανομής οδηγούν στην κατανόηση της δομή της πόλης. Οι απαραίτητες μετρήσεις για το μοντέλο της πόλης είναι η πυκνότητα των κτιρίων, το μέσο μέγεθος κτιρίου, ο αριθμός Cn και η τοπική πυκνότητα, τα οποία θα εξηγηθούν λεπτομερέστερα παρακάτω. Η μέση πυκνότητα κτιρίου ορίζεται ως η αναλογία του αριθμού των κτιρίων που διαιρείται με τη συνολική έκταση της πόλης, [85].

$$\rho = \frac{N}{A} \tag{4.1}$$

όπου N είναι το πλήθος των κτιρίων και A η έκτασης της πόλης. Η πυκνότητα αυτή είναι θεμελιώδης για τους υπολογιμούς του g(r).

$$g(r) = \frac{1}{N} \sum_{i=1}^{N} \frac{n_i(r + dr) - n_i(r)}{\bar{\rho}_{city} 2\pi r \times dr} \tag{4.2}$$

όπου $n_i(r)$ δείχνει τον αριθμό των κτιρίων εντός της ακτινικής απόστασης r από το εκάστοτε κτίριο i. Επιπλέον, το dr αποτελεί την ακτινική αύξηση, η οποία έχει επιλεγεί ως το 5% του μέσου μεγέθους του κτιρίου (L), δηλαδή $dr = 0.05L$ [4.6] $= exp(Nlog(A_i))$ [4.7] όπου N το πλήθος των κτιρίων και A_i η επιφάνεια του κτιρίου i.

$$L = \exp(\frac{1}{N} \sum_{i=1}^{N} \sqrt{log(A_i)}) \tag{4.3}$$

Για κτίρια (και πόλεις) το πρώτο ελάχιστο της g(r) είναι αντιπροσωπευτικό του χαρακτηριστικού μεγέθους R, της τοπικής συστάδας (cluster), όπου η πυκνότητα των κτιρίων μέσα στο cluster αποκλίνει αισθητά από το μέση τιμή του συστήματος [85]. Το Rmax μπορεί να υπολογιστεί μόνο για δείγμα πόλεων με κρυσταλλική ή υγρή δομή. Για πόλεις με αέρια δομή, εν γένει δεν είναι δυνατό να υπολογιστεί το ελάχιστο, καθώς η συνάρτηση δεν έχει κάποιο ελάχιστο.

Η πρώτη κορυφή του g(r) ποσοτικοποιεί την απόσταση στην οποία το g(r) φτάνει το μέγιστο. Στο πλαίσιο των πόλεων αυτή είναι η χαρακτηριστική απόσταση d μεταξύ του κτιρίου αναφοράς και του πρώτου κελύφους των τοπικών γειτόνων Cn. Λόγω του ότι για την ανάλυση του g(r) θεωρούνται τα κτίρια ως σωματίδια χωρίς μέγεθος, το d είναι η απόσταση μεταξύ των κεντρών μάζας των κτιρίων και όχι η ελάχιστη απόσταση μεταξύ των τοίχων των κτιρίων, [85]. Βρέθηκε ότι υπάρχει μια ισχυρή συσχέτιση μεταξύ R και d η οποία εκφράζεται από την μέση σχέση: d=0.72*R. Ο αριθμός Coordination Cn είναι ο αριθμός των κοντινότερων γειτόνων, που βρίσκονται γύρω από το κεντρικό άτομο αναφοράς, [85]. Στο πλαίσιο του g(r), το Cn ορίζεται ως η περιοχή κάτω από την πρώτη κορυφή της συνάρτησης. Κατά την εφαρμογή αυτού σε διδιάστατη δομή πόλης, ο αριθμός μπορεί να γενικευτεί ως:

$$C_n = 2pi\bar{\rho_{local}} \int_0^{rmax} rg(r)dr \tag{4.4}$$

όπου rmax η απόσταση κατά την οποία η g(r) φτάνει στο πρώτο ελάχιστο. Για το υπολογισμό του Cn πρέπει να υπολογίσουμε την τοπική πυκνότητα των κτιρίων (local density), local density $\bar{\rho_{local}}$:

Η οποία ορίζεται ως εξής:

$$\bar{\rho_{local}} = \frac{1}{n}\sum_{i=1}^{n}\frac{N_i}{A_r} \tag{4.5}$$

όπου N_i είναι ο αριθμός των κτιρίων σε κάθε τοπική επιφάνεια (local area) Ar η οποία είναι ορισμένη από έναν κύκλο με ακτίνα, rmax.

4.3 Συσχέτιση της δομής της πόλης και του φαινομένου UHI.

Χρησιμοποιώντας τη μέθοδο υπολογισμού θερμοκρασίας για το UHI, που παρουσιάστηκε στο προηγούμενο κεφάλαιο δίνεται η δυνατότητα να διερευνηθεί αν υπάρχει κάποια συσχέτιση μεταξύ της αστικής θερμικής νησιδας επιφανείας και της δομής της πόλης. Έχει διαπιστωθεί ότι υπάρχει υψηλή συσχέτιση μεταξύ του φαινομένου UHI με την θερμοκρασία αέρα κατά τη διαρκεια της νυχτας και τη δομή της πόλης. Σε αυτήν την μελέτη δορυφορικά δεδομένα για τον υπολογισμό της θερμοκρασίας εδάφους δίνουν συνεχείς μετρήσεις για ολόκληρη την πόλη και την αστική περιοχή. Ο μόνος περιορισμός αυτής της μεθόδου είναι ότι έχουμε μόνο θερμοκρασίες για μια συγκεκριμένη χρονική στιγμή. Το γεγονός της λήψης εικόνων σε διαφορετικές ώρες της ημέρας είναι προβληματικό, καθώς η γωνία του ήλιου διαφέρει και τα δεδομένα θερμοκρασίας δεν μπορούν εύκολα να συγκριθούν. Στο παρακάτω γράφημα, Σχήμα 4-1, παρατίθεται η συνάρτηση πυκνότητας πιθανότητας για τις τρεις κατηγορίες δομών, το αέριο, το υγρό και τον κρύσταλλο. Το UHI υπολογίζεται από τα δορυφορικά δεδομένα, τα οποία πραγματοποιούνται λαμβάνοντας τη διαφορά μεταξύ των μέσων αστικών και αγροτικών θερμοκρασιών. Όπως παρατηρείται στο γράφημα, η κατανομή για τα αέρια έχει μεγάλη απόκλιση, ενώ για τις κρυστάλλινες πόλεις το UHI έχει σημαντικά μικρότερο εύρος.

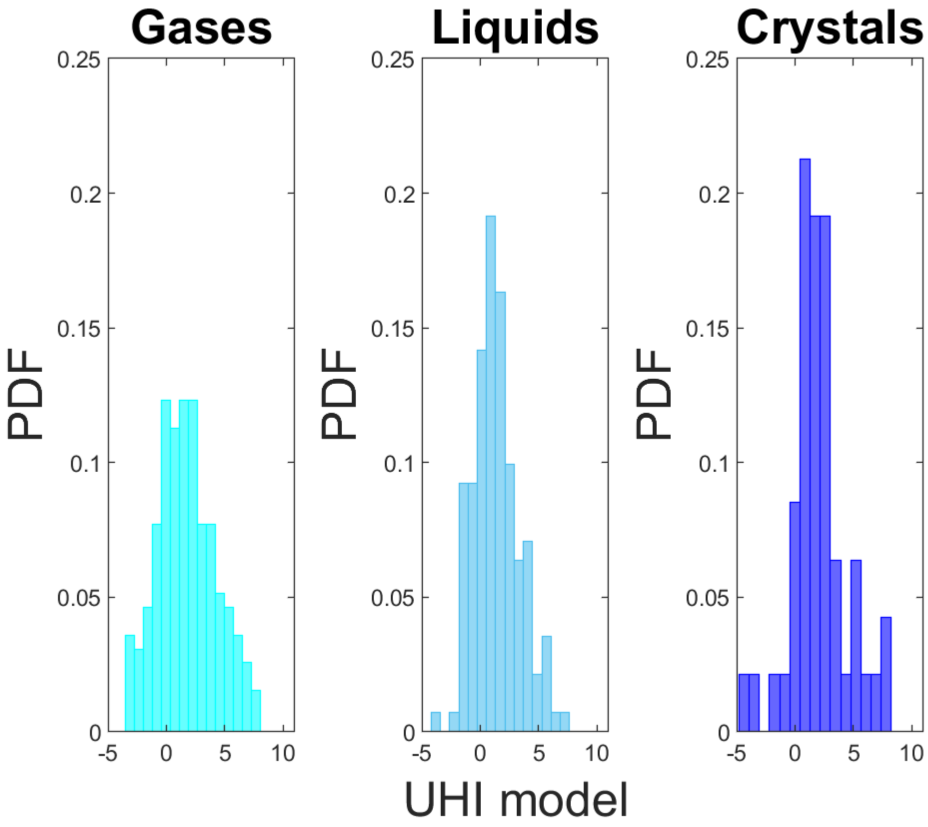

Σχήμα 4-1: Συνάρτηση πυκνότητας πιθανότητας UHI για 35 πόλεις ταξινομημένες με βάση τη δομή τους

f

Κεφάλαιο 5

Ρευστομηχανική μελέτη για συνθετικές πόλεις

5.1 Εισαγωγή

Σε αυτό το κεφάλαιο εξετάζεται ο τρίτος ερευνητικός στόχος, ο οποίος επιβάλλει τη χρήση της συνάρτησης ακτινικής κατανομής g(r) για τη μοντελοποίηση της πόλης. Σε ένα περαιτέρω βήμα, αυτά τα μοντέλα χρησιμοποιούνται για τη δημιουργία συνθετικών πόλεων και τη μετατροπή τους σε κτίρια για την εφαρμογή cfd προσομοιώσεων για την ποσοτικοποίηση φορτίων στα κτίρια.

5.2 Προσομοίωση πόλεων-συνθετικές πόλεις

Ο στόχος αυτής της προσέγγισης είναι η δημιουργία αντιπροσωπευτικών δειγμάτων των πόλεων για τον υπολογισμό των φορτίων ανέμου. Η θεμελιώδης μέθοδος για τη δημιουργία αυτών των συνθετικών πόλεων βασίζεται σε προσομοιώσεις Monte Carlo, οι οποίες είναι υπολογιστικοί αλγόριθμοι που βασίζονται σε επαναλαμβανόμενες τυχαίες δειγματοληψίες για την επίτευξη αριθμητικών αποτελεσμάτων. Στα προβλήματα που σχετίζονται με τη φυσική, οι μέθοδοι Monte Carlo είναι χρήσιμες για την προσομοίωση συστημάτων με πολλούς συζευγμένους βαθμούς ελευθερίας, όπως ρευστά, μη ταξινομημενα υλικά και κυτταρικές δομές. Κατ’ αρχήν, οι μέθοδοι Monte Carlo μπορούν να χρησιμοποιηθούν για την επίλυση οποιουδήποτε προβλήματος που έχει μια πιθανοτική ερμηνεία, [97]. Στην παρούσα προσέγγισή στόχος είναι η δημιουργία δειγμάτων τυχαίων πόλεων τα οποία θα πρέπει να ακολουθούν τις παραμέτρους περιγραφής της πόλης που εξηγούνται από την συνάρτηση ακτινικής κατανομής. Το σημαντικό γεγονός εδώ είναι ότι η προσέγγιση Monte Carlo επιτυγχάνει την αναδημιουργία στατιστικά χαρακτηριστικών πόλεων, όπως το Παρίσι με 103,367 κτίρια αλλά με την χρήση ενός σημαντικά μειωμένου πλήθους κτιρίων, περίπου 900. Αυτά τα μοντέλα πόλεων χρησιμοποιούνται ως μοντέλα για τον υπολογισμό φορτίων πάνω στα κτίρια μιας πόλης.

5.3 Μεθοδολογία

Η μέθοδος που ακολουθήθηκε για την δημιουργία των συνθετικών πόλεων παρουσιάζεται στο παρακάτω διάγραμμα ροής, Σχήμα 5-1. Συγκεκριμένα, ορίζοντας συγκεκριμένη πυκνότητα πόλης και αριθμό κτιρίων μπορεί να καθοριστεί η επιφάνεια της πόλης. Στην συνέχεια προστίθενται κτίρια που αποτελούν γειτονικά κτίρια για τον ακριβή υπολογισμό του g(r) πάντοτε έχοντας την πυκνότητα 0.25 ως κριτήριο. Το επόμενο βήμα αφορά την Monte Carlo προσομοίωση, επιλέγουμε τυχαία ένα κτίριο και του αλλάζουμε τυχαία μια θέση. Αν το g(r) προσεγγίζει καλύτερα το g(r) της πραγματικής πόλης, αφήνεται στην θέση που τοποθετήθηκε και αυτό συνεχίζεται για 250,000 επαναλήψεις, όπως παρουσιάζεται στο Σχήμα 5-2. Σε όλα τα παραπάνω βήματα τα κτίρια εξακολουθούν να είναι σημεία, όπως φαίνεται στο Σχήμα 5-3 για την πόλη της Αθήνας, ενώ η μετατροπή τους σε διδιάστατη και στην συνέχεια τρισδιάστατη μορφή γίνεται με βάση το χαρακτηριστικό μήκος κτιρίου.

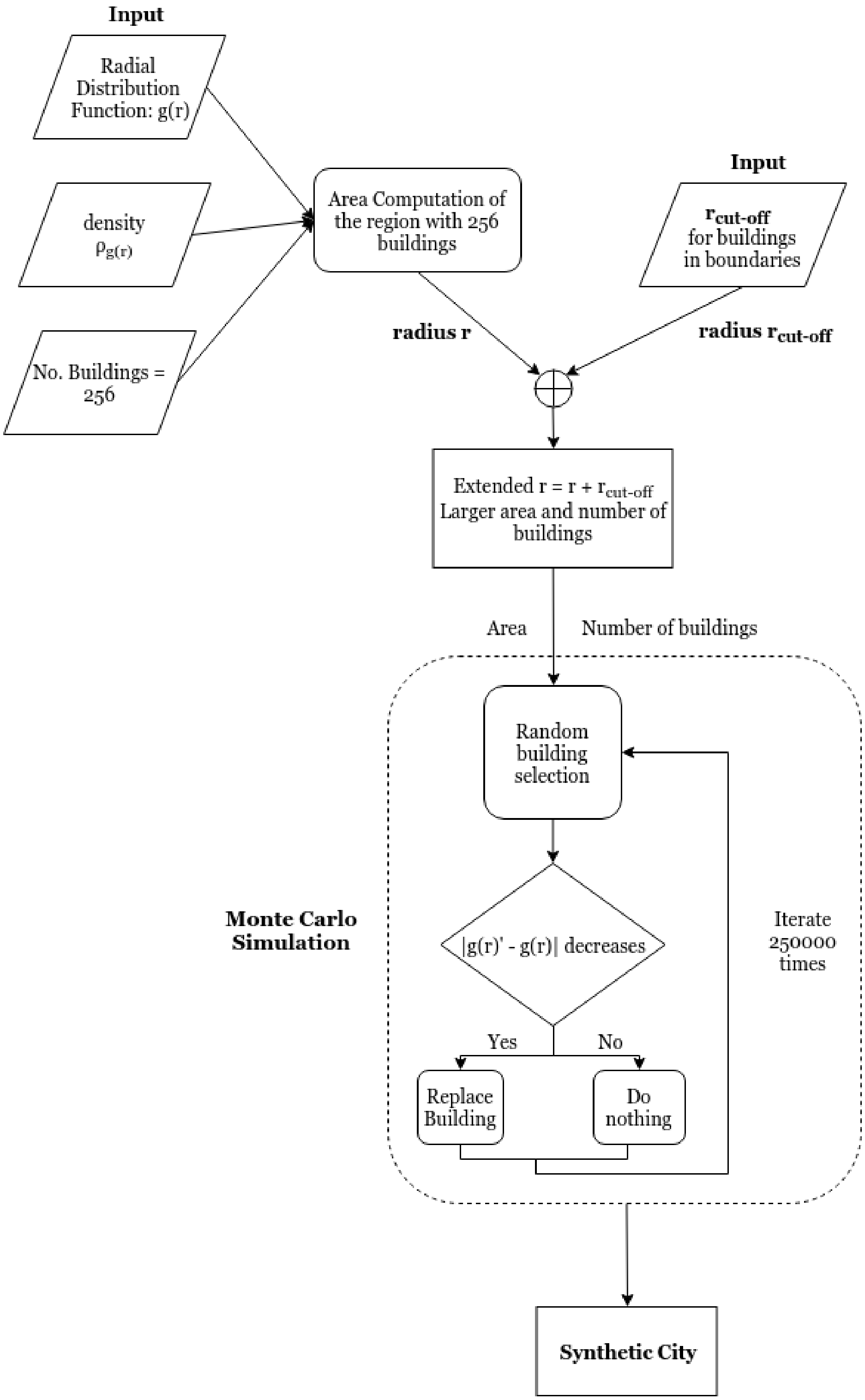

Σχήμα 5-1: Μοντελοποίηση της πόλης

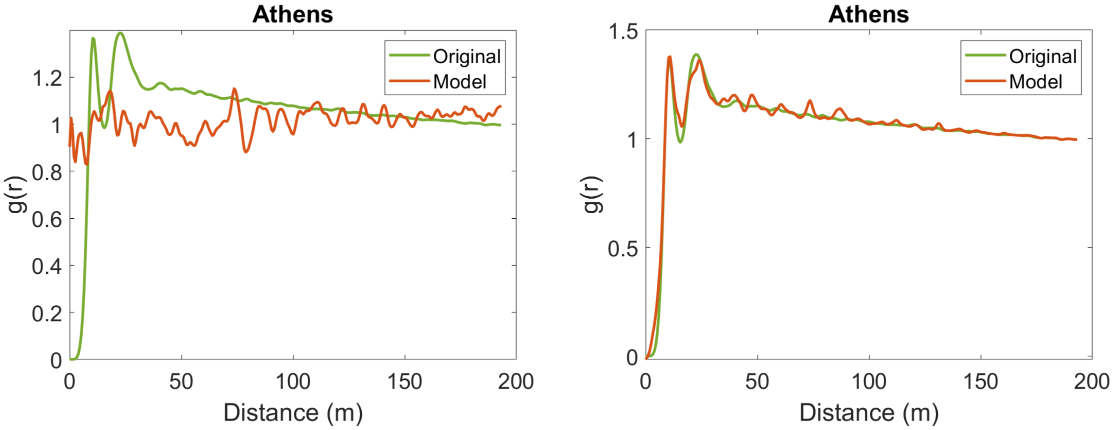

(α΄) Αρχικό βήμα της προσομοίωσης Monte Carlo(β΄) Τελικό βήμα της προσομοίωσης Monte Carlo

Σχήμα 5-2: Συνάρτηση ακτινικής διανομής για τη μοντελοποιήση και πρωτότυπη μορφή της πόλης

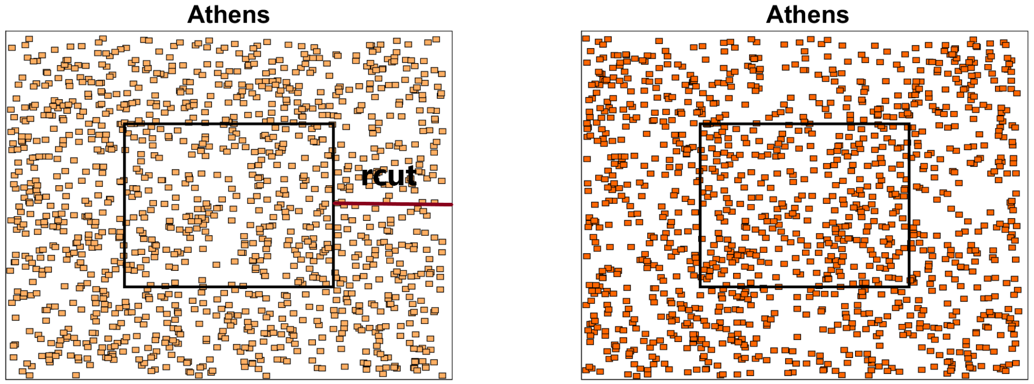

(α΄) Αρχική διαμόρφωση της Αθήνας

(β΄) Τελική διαμόρφωση της Αθήνας

Σχήμα 5-3: Συνθετική πόλη της Αθήνας

5.4 Υπολογισμοί Φορτίων Ανέμων στην πόλη

Η αεροδυναμική μελέτη στην πόλη χωρίζεται σε δύο τμήματα. Η αρχική μελέτη αφορά τον υπολογισμό ταχυτήτων στην έξοδο της πόλης για την οποία δεν απαιτείται ιδιαίτερη ακρίβεια κοντά στα κτίρια, όπου εφαρμόζεται ένα μοντέλο τυρβώδους ροής,$k-\epsilon$, ασυμπίεστου, συνεκτικού ρευστού.

Η δεύτερη μελέτη αφορά τον υπολογισμό των φορτίων πάνω στα κτίρια και απαιτεί μια πιο λεπτομερή ανάλυση. Σε αυτήν τη μελέτη γίνεται η χρήση του μοντέλου, Large Eddy Simulation (LES). Η μέθοδος LES έχει τη δυνατότητα για βελτιωμένη ακρίβεια όταν η ανάλυση των μεγαλύτερων στροβίλων είναι σημαντική. Τα μειονεκτήματα εδώ είναι κυρίως ότι είναι υπολογιστικά ακριβό, απαιτείται υψηλότερη ανάλυση πλέγματος και επίσης μια αστάθεια προσομοίωσης με μικρά βήματα χρόνου δημιουργεί υψηλό υπολογιστικό κόστος και μεγάλο όγκο δεδομένων. Όπως εξηγείται στη μεθοδολογία, πρόκειται για μια πολύ απλή γεωμετρία η οποία δίνει τη δυνατότητα εφαρμογής της προσομοίωση LES. Οι μελέτες για τα μοντέλα των πόλεων έγιναν με τη χρήση άδειας του Ansys από το εργαστήριο στο MIT. Μια συγκριτική μελέτη μεταξύ των αποτελεσμάτων του λογισμικού του εργαστηρίου και των αποτελεσμάτων από το Ansys παρουσιάζεται παρακάτω. Μια απλοποιημένη αρχικά περίπτωση με δύο κτίρια έχει εφαρμοστεί, αλλά θα μπορούσε να επεκταθεί και σε ολόκληρο το μοντέλο της πόλης με 500 κτίρια.

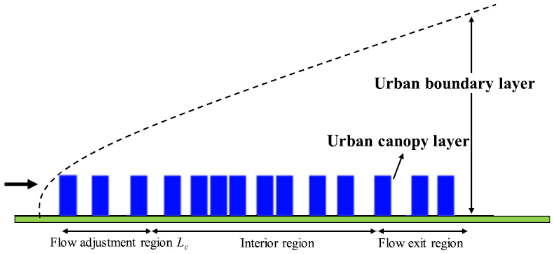

Σχήμα 5-4: Περιοχές της μοντελοποιημένης πόλης

5.5 Σύγκριση αποτελεσμάτων Ansys και CFD software PUMA

Έχει εφαρμοστεί ένα μοντέλο σύγκρισης δύο κτιρίων για την επέκταση της μεθοδολογίας χρησιμοποιώντας έναν ανοικτό κώδικα επίλυσης CFD. Στόχος αυτής της προσέγγισης είναι η επίτευξη εξαιρετικά ακριβών αποτελεσμάτων με τη χρήση μη εμπορικών επιλυτών. Τα αποτελέσματα των λύσεων Ansys και του κώδικα CFD από τη μονάδα Παράλληλης Υπολογιστικής Ρευστομηχανικής και Βελτιστοποίησης του ΕΜΠ, είναι παρόμοια, όπως φαίνεται στον παρακάτω πίνακα.

	PUMA	**ANSYS**
cd	0.1219	0.1348

Ορισμένες λεπτομέρειες για τους υπολογισμούς με το λογισμικό PUMA δίνονται παρα-

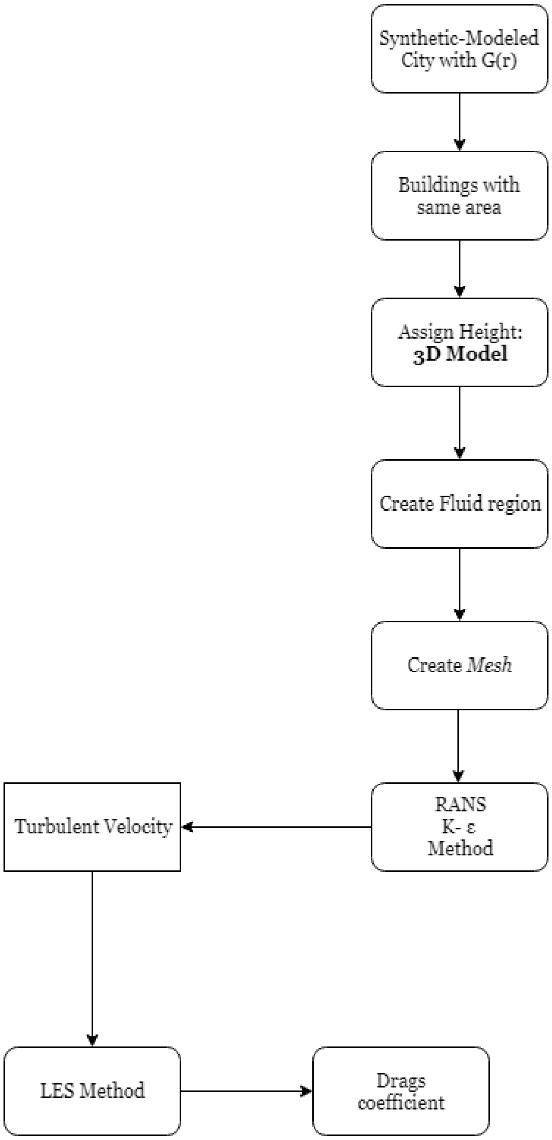

Σχήμα 5-5: Διάγραμμα ροής της μεθοδολογίας

κάτω: GPU κώδικας PUMA (Parallel Unstructured Multirow and Adjoint) του PCOpt/ΕΜΠ. Το πλέγμα αποτελείται από 78,587 κόμβους και 420,584 hetra. Ένα CFD (steady) σε μία NVIDIA Tesla P100 (αρχιτεκτονικής Pascal) με 16 GB GPU μνήμη, με υπολογιστικό χρόνο 7 λεπτά.Η προσομοίωση έγινε με το μοντέλο τύρβης Spalart-Allmaras με wall functions.

Οι τιμές που παρουσιάζονται στον πίνακα παρουσιάζουν μικρή διαφορά συγκρίνοντας το cd που υπολογίστηκε. Ο συντελεστής οπισθέλκουσας του δεύτερου κτιρίου έχει συγκριθεί, με βάση τη μεθοδολογία της προηγούμενης προσέγγισης, δεδομένου ότι τα φορτία στο πρώτο κτίριο, δεν είναι αντιπροσωπευτικά.

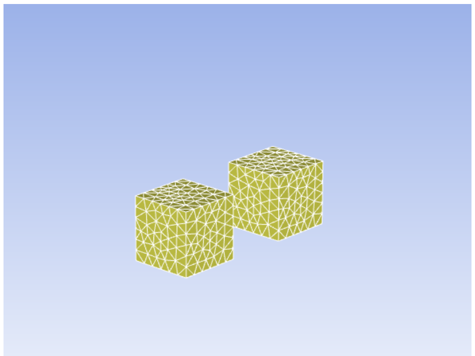

Σχήμα 5-6: Επιφανειακό πλέγμα γύρω από τα δύο κτίρια για τους CFD υπολιογισμούς.

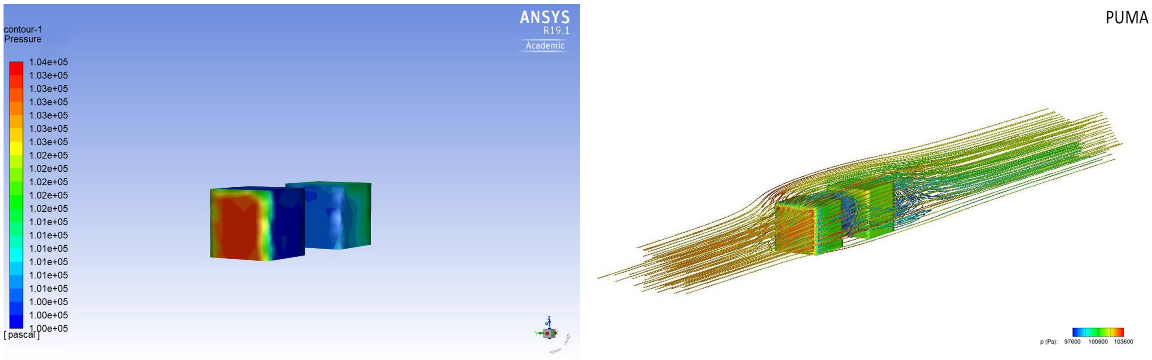

(α΄) Κατανομή πιέσεων, ANSYS

(β΄) Κατανομή πιέσεων , PUMA

Σχήμα 5-7: Σύγκριση αποτελεσμάτων με την χρήση του ANSYS και PUMA

Τα ακριβή συμπεράσματα με τις δύο μεθόδους, καθιστόύν και τις δύο ιδιαίτερα αξιόπιστες. Ένας σημαντικός περιορισμός στην δημιουργία πιο πυκνών πλεγμάτων στην μοντελοποίηση ολόκληρης της πόλης αποτελεί το υπολογιστικό κόστος. Οι υπολογισμοί με την χρήση του κώδικα PUMA έχουν εμφανώς μικρότερο χρόνο εκτέλεσης. Μια τέτοια διαπίστωση οδηγεί στο συμπέρασμα ότι για τον ίδιο υπολογιστικό χρόνο θα μπορούσαμε να λάβουμε πιο υψηλής ακρίβειας αποτελέσματα.

5.6 Αποτελέσματα

Η πρώτη έξοδος της προσομοίωσης CFD είναι η ταχύτητα των τεσσάρων διαφορετικών πόλεων. Η ταχύτητα στο έδαφος για το $z = 0$ είναι μηδέν, με σεβασμό στην οριακή συνθήκη μη ολίσθησης. Καθώς το ύψος αυξάνεται, η ταχύτητα αυξάνεται καθώς η επίδραση των εμποδίων μειώνεται. Τα παρακάτω γραφήματα, Σχήμα 5.7, δείχνουν την ταχύτητα στο ύψος $h/2 = 5m$ των κτιρίων και $h = 10m$ στην κορυφή των κτιρίων. Και στις δύο περιπτώσεις η ταχύτητα αυξάνεται περισσότερο στα στενά κενά μεταξύ των κτιρίων. Το φαινόμενο αυτό βασίζεται στη διατήρηση της μάζας και στην εξίσωση Bernoulli. Στη συγκεκριμένη προσέγγιση έχοντας πολλαπλά εμπόδια-κτίρια, η ροή γύρω από τα προηγούμενα κτίρια επηρεάζει την ταχύτητα και την πίεση, [12]. Η απλοποιημένη προσέγγιση μπορεί να χρησιμοποιηθεί μόνο για μια πολύ απλή κατανόηση του αποτελέσματος. Οι διαφορετικές δομές της πόλης καταλήγουν σε διαφορετικό μέγεθος ταχύτητας, το οποίο επηρεάζει αντίστοιχα τις δυνάμεις οπισθέλκουσας στα κτίρια.

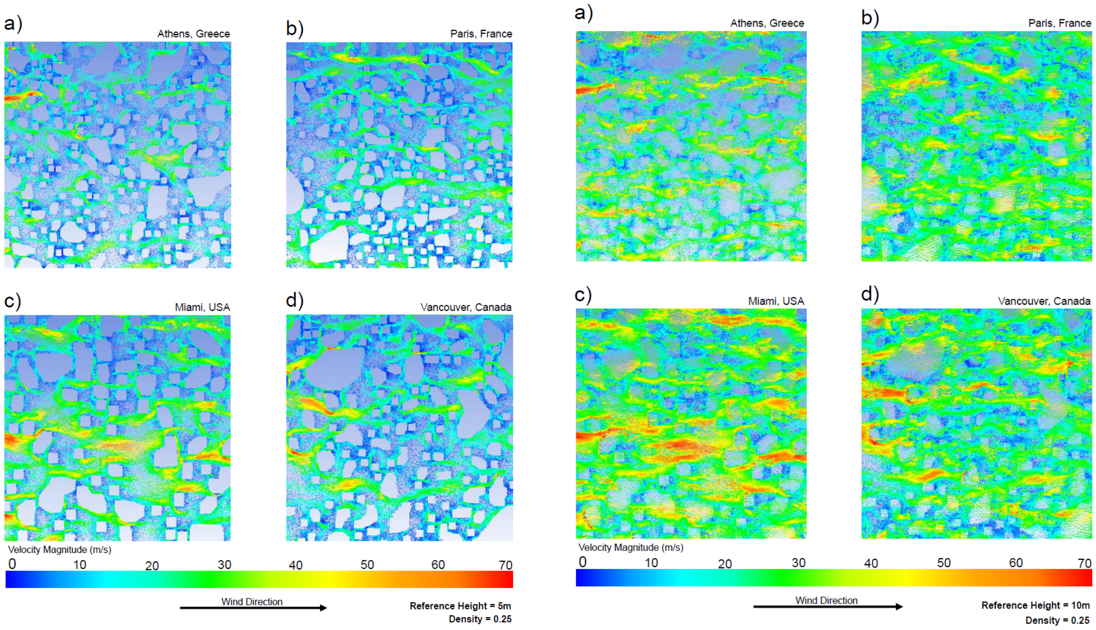

(α΄) Ταχύτητα για ύψος $z = h/2 = 5m$

(β΄) Ταχύτητα για ύψος $z = h = 10m$

Σχήμα 5-8: Μέτρο ταχύτητας για τις 4 υπολογισμενες πόλεις

Ο στόχος αυτής της μελέτης είναι να βρεθεί μια στατιστικά έγκυρη συσχέτιση που θα ποσοτικοποιεί τη συσχέτιση της μορφολογίας της πόλης και του συντελεστή αντίστασης. Ο συντελεστής αντίστασης εξαρτάται από το σχήμα και τις συνθήκες ροής και ορίζεται ως το κλάσμα της διαφοράς πίεσης στα τοίχωματα των κτιρίων προς την δυναμική πίεση. Το λογισμικό Ansys μας δίνει τη δυνατότητα του υπολογισμού αυτών των πιέσεων σε κάθε κτίριο. Ο μέσος όρος του συντελεστή αντίστασης για κάθε πόλη δίνει διαφορετικά αποτελέσματα. Όπως φαίνεται στα διαγράμματα οι κρυσταλλικές πόλεις όπως το Βανκουβερ και το Μαϊάμι έχουν υψηλότερο συντελεστή αντίστασης, ενώ τα αέρια (gases) μικρότερο.

Η διάταξη των κτιρίων και το είδος της ροής επηρρεάζει αυτήν την τιμή του συντελεστή αντίστασης.

$$\int_A dPdA = D \tag{5.1}$$

Η δυναμική πίεση (dynamic pressure q), χρησιμοποιείται για τον προσδιορισμό του συντελεστή αντίστασης.

$$Cd = \frac{2D}{A\rho V^2} \tag{5.2}$$

$$q = \frac{1}{2}\rho V^2 \tag{5.3}$$

$$Cd = \frac{Dq}{A} \tag{5.4}$$

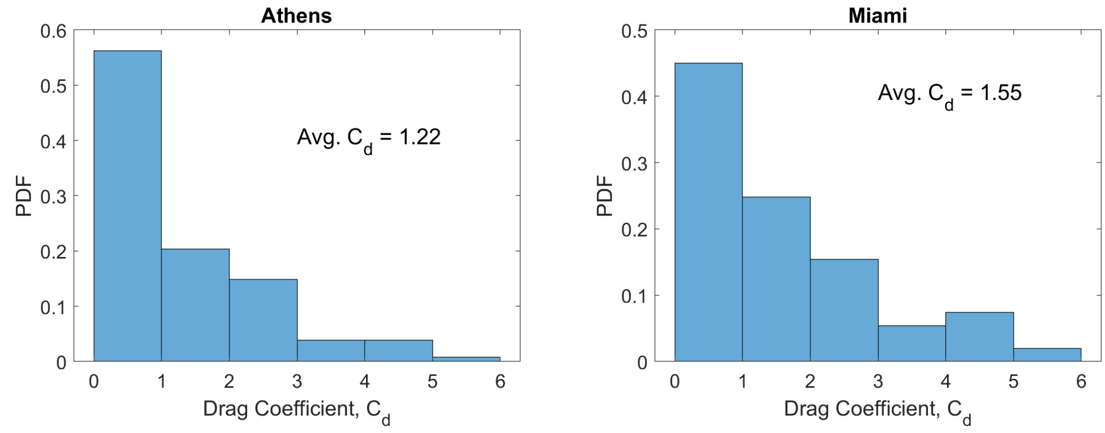

(α΄) Αθήνα-Δομή υγρού

(β΄) Παρίσι-Δομή αερίου

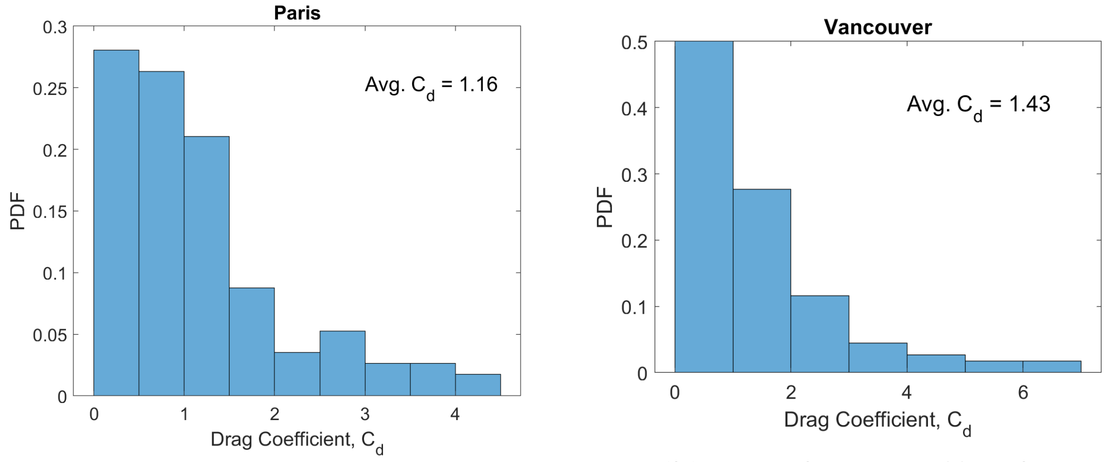

(γ΄) Μαϊάμι-Δομή υγρού

(δ΄) Βανκούβερ-Κρυσταλλική δομή

Σχήμα 5-9: Συνάρτηση πυκνότητας πιθανότητας του συντελεστή αντίστασης για τις 4 υπολογισμένες πόλεις